8-8-2023

AI-enabled modeling and monitoring of data-rich advanced manufacturing systems

Abdullah Al Mamun
Mississippi State University, green.mamun@gmail.com

AI-enabled modeling and monitoring of data-rich advanced manufacturing systems

By

Abdullah Al Mamun

Approved by:

Wenmeng Tian (Major Professor)
Linkan Bian (Co-Major Professor)
T.C. Falls
Haifeng Wang
Mohammad Marufuzzaman (Graduate Coordinator)
Jason Keith (Dean, Bagley College of Engineering)

A Dissertation
Submitted to the Faculty of
Mississippi State University
in Partial Fulfillment of the Requirements
for the Degree of Doctor of Philosophy
in Industrial & Systems Engineering
in the Department of Industrial & Systems Engineering

Mississippi State, Mississippi

August 2023

Name: Abdullah Al Mamun

Date of Degree: August 8, 2023

Institution: Mississippi State University

Major Field: Industrial & Systems Engineering

Major Professors: Wenmeng Tian, Linkan Bian

Title of Study: AI-enabled modeling and monitoring of data-rich advanced manufacturing Systems

Pages in Study: 109

Candidate for Degree of Doctor of Philosophy

ABSTRACT

The infrastructure of cyber-physical systems (CPS) is based on a meta-concept of cybermanufacturing systems (CMS) that synchronizes the Industrial Internet of Things (IIoTs), Cloud Computing, Industrial Control Systems (ICSs), and Big Data analytics in manufacturing operations. Artificial Intelligence (AI) can be incorporated to make intelligent decisions in the day-to-day operations of CMS. Cyberattack spaces in AI-based cybermanufacturing operations pose significant challenges, including unauthorized modification of systems, loss of historical data, destructive malware, software malfunctioning, etc. However, a cybersecurity framework can be implemented to prevent unauthorized access, theft, damage, or other harmful attacks on electronic equipment, networks, and sensitive data. The five main cybersecurity framework steps are divided into procedures and countermeasure efforts, including identifying, protecting, detecting, responding, and recovering. Given the major challenges in AI-enabled cybermanufacturing systems, three research objectives are proposed in this dissertation by incorporating cybersecurity frameworks. The first research aims to detect the *in-situ* additive manufacturing (AM) process authentication problem using high-volume video streaming data. A side-channel monitoring

approach based on an *in-situ* optical imaging system is established, and a tensor-based layer-wise texture descriptor is constructed to describe the observed printing path. Subsequently, multilinear principal component analysis (MPCA) is leveraged to reduce the dimension of the tensor-based texture descriptor, and low-dimensional features can be extracted for detecting attack-induced alterations. The second research work seeks to address the high-volume data stream problems in multi-channel sensor fusion for diverse bearing fault diagnosis. This second approach proposes a new multi-channel sensor fusion method by integrating acoustics and vibration signals with different sampling rates and limited training data. The frequency-domain tensor is decomposed by MPCA, resulting in low-dimensional process features for diverse bearing fault diagnosis by incorporating a Neural Network classifier. By linking the second proposed method, the third research endeavor is aligned to recovery systems of multi-channel sensing signals when a substantial amount of missing data exists due to sensor malfunction or transmission issues. This study has leveraged a fully Bayesian CANDECOMP/PARAFAC (FBCP) factorization method that enables to capture of multi-linear interaction (channels $\times$ signals) among latent factors of sensor signals and imputes missing entries based on observed signals.

DEDICATION

This dissertation work is dedicated to my parents, Mohammad Sekendar Ali Molla, and Saleha Begum, who have been endless sources of love and encouragement in my entire life.

ACKNOWLEDGEMENTS

I would like to thank the individuals who helped me during the preparation of this dissertation work. First and foremost, I am thankful to Dr. Wenmeng Tian and Dr. Linkan Bian, the chair and co-chair of my Ph.D., respectively. I also thank my Ph.D. committee, Mr. T.C. Falls and Dr. Haifeng Wang, whose guidance and trust led me through almost four years of research that created this dissertation.

TABLE OF CONTENTS

LIST OF TABLES

LIST OF FIGURES

CHAPTER I

INTRODUCTION

1.1 Motivation

Nowadays, manufacturing organizations are embracing manufacturing operations with information and communication technology systems to extend connectivity and remote access for better manufacturing operations and competencies. Advanced electronic technologies have been integrated with multifaceted systems that can be coupled with the cyber (digital) world and physical world, which are known as cyber-physical systems (CPS) [1]–[4]. The adoption of CSP is based on a meta-concept of cybermanufacturing systems (CMS) that synchronizes the Industrial Internet of Things (IIoTs), cloud computing, industrial control systems (ICSs), and big data analytics in manufacturing operations [2], [5]–[7]. In CMS settings, IIoTs devices can be used to collect real-time data from various stages of the manufacturing process, such as raw material inventory, production equipment, and product quality control. Additionally, ICS consists of a combination of hardware and software components that work together to manage and optimize manufacturing operations [8]–[10].

Leveraging the massive data available, Artificial Intelligence (AI) can be incorporated to make smart decisions in the day-to-day operations of cybermanufacturing systems. Figure 1.1 demonstrates the workflow in an AI-enabled factory that integrates both physical and cyber domains. In the physical domain, heterogenous signals are collected from the manufacturing machinery and merged through the data-fusion process, followed by decision-fusion for

manufacturing operations. Process monitoring & prognostics is followed by process control & optimization. Finally, the process control and optimization decisions will be sent to the manufacturing machinery, subsequently, making a closed-loop system in the cybermanufacturing systems [11]. Therefore, various manufacturing domain knowledge needs to be appropriately incorporated in the modelling, monitoring, and optimization in the data-rich manufacturing systems.

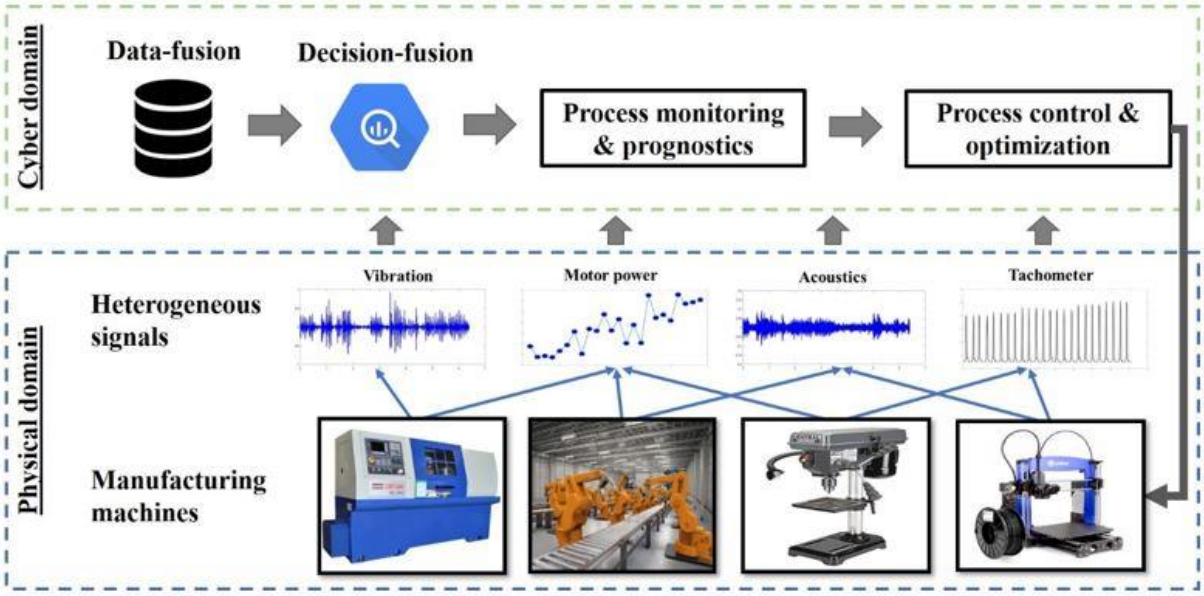

Figure 1.1 The overview of an AI-enabled cybermanufacturing systems.

1.2 Challenges

Even though AI has achieved significant success in modelling and monitoring, manufacturing operations pose inherent challenges, including: 1) potential cyber-physical attacks; 2) large volumes of data streams available; 3) ill-structured data, such as missing data. Collectively, these major challenges hinder modelling and monitoring-based decision-making activities in

cybermanufacturing systems. The above mentioned three challenges and their significances are briefly described in the following three sub-sections.

1.2.1 Potential cyberattacks

Cybermanufacturing systems have brought the global industrial operations to the easily accessible platforms while cyber-physical security has raised a serious concern for operational safety and product quality assurance [12]. In the cyber-physical systems, a malicious cyberattack may manipulate the machine operations and/or controls on various different levels, including altering machine setup parameters, changing product design, and injecting false sensing data [12], [13]. These will lead to compromised product, uncertified manufacturing procedure, and even machine or facility shutdowns. What is worse, conventional quality control (QC) systems are not effective in detecting those cyberattack induced changes in the manufacturing systems, because those attacked processes may still be "statistically in control" [12], [14]. To tackle these challenges, cybersecurity capabilities should be thoroughly investigated and practiced among small and medium manufacturing organizations, stakeholders, and third-parties [15]. Therefore, there is an urgent need to identify potential cybersecurity risks and manage identified risks in CSP [1], [2].

1.2.2 Large volumes of data streams available

In cybermanufacturing systems, the advanced sensing technologies provide massive essential data in real time collected from the manufacturing processes for quality control and machine diagnosis purposes. The data are recorded from different machines, workstations, and even production floors, generating a large volume of data streams in real time [16]. Therefore, how to integrate the large volume of heterogeneous manufacturing data in-process monitoring is an open question, given the increasingly large volume of data streams available [17], [18].

1.2.3 Ill-structured data and associated missing data

In CMS setting, the heterogeneous sensor can capture signals from manufacturing machinery. Signals may include noises, outliers, and missing data, leading to ill-structured data. Multi-channel sensor fusion can be challenging for real-time machinery fault identification and diagnosis when a substantial amount of missing data exists. For example, when significant missing data is present, the process condition and machine operating conditions may not be timely predicted. However, there are still substantial challenges in imputing missing data in high-dimensional sensing data [19]–[21].

1.3 Research objectives

Given the three major challenges in the AI-enabled cybermanufacturing systems modeling and monitoring, the three research objectives of this dissertation are described in the following sub-sections.

1.3.1 Process authentication of additive manufacturing for detecting cyberattack-induced alterations

The first research objective aims to detect the *in-situ* additive manufacturing (AM) process authentication problem by using high-volume yet very noisy video streaming data. Most cyberattacks towards AM processes can be manifested as printing path alterations, and an *in-situ* optical imaging system can focus on detecting alterations in the printing path. A side-channel monitoring approach based on an *in-situ* optical imaging system is established, and a tensor-based layer-wise texture descriptor is constructed to describe the observed printing path. Subsequently, tensor decomposition is leveraged to reduce the dimension of the tensor-based texture descriptor, and low-dimensional features can be extracted for detecting cyberattack-induced alterations.

1.3.2 Fault diagnosis of rotary machinery given high volume data streams

The second research work seeks to address the high-volume data stream problems in multi-channel sensor fusion for bearing fault diagnosis. Multi-channel sensor fusion can be more robust for diagnosing diverse bearing fault scenarios. However, diverse bearing fault scenarios can pose significant challenges for effective fault diagnosis when dealing with high-dimensional data. The second approach proposes a new multi-channel sensor fusion methodology, frequency-domain multilinear principal component analysis (FDMPCA), integrating acoustics and vibration signals with different sampling rates. Subsequently, the FD tensor is decomposed by multilinear principal component analysis (MPCA), resulting in low-dimensional process features for diverse bearing fault diagnosis by incorporating a Neural Network classifier, which significantly outperforms compared with a benchmark.

1.3.3 Missing signals imputation from multi-channel sensing signals by tensor factorization

The third research proposes a fully Bayesian CANDECOMP/PARAFAC (FBCP) factorization method for missing data recovery systems of mixed-bearing fault signals. Multi-channel sensor fusion can be challenging for real-time machinery fault identification and diagnosis when a substantial amount of missing data exists. Usually, some (or even all) sensors may not function correctly during real-time data acquisition due to sensor malfunction or transmission issues. Additionally, multi-channel sensor fusion yields a large volume of data. Imputation of missing entries can also be challenging with a large volume of data, which can predominantly affect the accuracy of machinery fault diagnosis. However, how to impute a substantial amount of missing data for machinery fault identification is an open research question. This proposed method can

effectively impute a substantial portion of continuous missing data from diverse bearing fault scenarios.

1.4 Dissertation outline

This dissertation has 7 chapters. Chapter 2 provides a comprehensive state-of-the-art review of papers for the proposed research. Chapter 3 describes a novel part authentication methodology based on image texture analysis of the layer-wise *in-situ* videos. This paper has been published in the Journal of Manufacturing Systems on 6th January 2022. Chapter 4 incorporates the condition-based maintenance of rolling element bearings. This chapter involves feature-level sensor fusion for *in-situ* anomaly detection of rolling element bearings and integrating time-frequency analysis and tensor decomposition under multiple mixed component faults on a Machinery Fault Simulator® [22]. This paper was published in the International Journal of Advanced Manufacturing Technology on 30th November 2022. Chapter 5 describes missing signal imputation for multi-channel sensing signals on rotary machinery by factorization method. In this chapter, a varying percentage of continuous missing signal scenarios is generated, and missing signal imputation in the time-domain tensor is adopted by a fully Bayesian CANDECOMP/PARAFAC (FBCP) factorization method. The summary of this dissertation work and future directions are leveraged in chapter 6. Chapter 7 lists all the cited papers relevant to this dissertation proposal. Table 1.1 describes this dissertation proposal's relevant topics, titles, and publication status.

Table 1.1 Relevant topics, titles, and publication status.

Topic #	Title	Publication status
1. Quality Control and reliability of Additive Manufacturing	Securing cyber-physical additive manufacturing systems by *in-situ* process authentication using streamline video analysis.	Published on January 6th, 2022, on the Journal of Manufacturing Systems [23].
2. Condition-based Maintenance of rolling element bearings	Multi-channel sensor fusion for *in-situ* bearing fault diagnosis by frequency-domain multilinear principal component analysis.	Published on November 30th, 2022, on the International Journal of Advanced Manufacturing Technology [24].
3. Missing signal imputation for multi-channel sensing signals by factorization method	Missing signal imputation for multi-channel sensing signals on rotary machinery by tensor factorization.	Accepted on March 8, 2023 by Manufacturing Letters [25].

CHAPTER II

LITERATURE REVIEW

Given the major challenges in AI-enabled cybermanufacturing systems, three research objectives are proposed in this dissertation work by incorporating cybersecurity frameworks. In this literature, sections 2.2 and 2.2 demonstrate the cybersecurity risks and how to manage associated cybersecurity risks in cybermanufacturing systems. Subsequently, section 2.3 is related to an overview of three proposed research methods by linking cybermanufacturing systems. Section 2.4 demonstrates state-of-the-art quality assurance methods for additive manufacturing related to the first proposed method. Section 2.5 seeks literature of the second and third proposed methods.

2.1 Understanding the cybersecurity risks in cybermanufacturing systems

Cybersecurity risks in cybermanufacturing systems are widespread and can be categorized into four major phases: threats, vulnerability, likelihood, and impact [5], [26]. Several cybersecurity threats to cybermanufacturing can be included as data breaches, malware attacks, insider threats, supply chain attacks, and physical attacks [27]–[29]. There are several cybersecurity vulnerabilities that cybermanufacturing systems may encounter, including lack of authentication and access control, weak encryption, inadequate software security, unsecured network connections, lack of physical security, and unsecured third-party security [29]–[31]. The likelihood of a cybersecurity breach in cybermanufacturing depends on factors, including the level of security measures in organizations, the complexity of cybermanufacturing process, and cybersecurity best

practices [32]. These security risks of cybermanufacturing have led to interrogation about unobserved attack spaces. The impact of cybersecurity incidents in cybermanufacturing is widespread. According to NIST report in 2017, approximately 61 % of small businesses in the U.S. experienced cyberattacks, and 34 % of all documented attacks targeted manufacturers. Significant cyberattacks on industrial control systems include German Still Mill in 2014, Kemuri Water Company in 2016, New York Dam in 2013, Target Stores in 2013, Ukraine Power Grid Attack in 2015 and 2016, etc [2], [33]–[35]. However, the widespread adoption of cybersecurity has been leveraged against the rise of cyberattacks space in cybermanufacturing. Increasing awareness of cybersecurity issues has brought significance to smart manufacturing, transportation, and large-scale infrastructures (power grid, water supply, healthcare, etc.) [36]–[38].

2.2 Managing cybersecurity risks in cybermanufacturing systems

Risk assessment of cybermanufacturing setting requires complement measures that fall under cybersecurity standards, governances, and practices. Cybersecurity framework can be implemented as procedures for managing cybersecurity risks of cybermanufacturing systems and associated manufacturing stakeholders and industry best practices [5], [8], [39], [40]. Additionally, cyberattack countermeasures in cybermanufacturing settings can be utilized to analyse the sensitivity of a cyberattack-induced environment [39], [41]. The five main cybersecurity framework areas are divided into particular procedures and countermeasure efforts (Table 2.1) [5], [8], [39], [40]. The first step of cybersecurity is to identify the risks comprising developing and managing cybersecurity risks to systems, people, assets, data, and capabilities. The second step is to protect against the impact of a likely cybersecurity incident. According to a Trust Alliance analysis in 2018, 95% of all cyberattacks could have been prevented using common sense employees, typically included in cybersecurity protection measures [42]. The third step is to follow

up on activities shielded by the detect function permit for real-time exposure to cybersecurity measures. The forth step is the response function that helps to lessen the effect of cyberattack incidents. The final phase of the cybersecurity framework is to recover plans that help an organization continue regular operations after a cyberattack incident. These steps are not a one-time process but a continuous practice that can be embraced in cybermanufacturing settings. Much research has focused on identifying countermeasures for cyberattacks in cybermanufacturing and analysing the sensitivity of cyberattack-induced environments as countermeasures [35].

Table 2.1 Cybersecurity steps and countermeasures in CMS.

Cybersecurity steps	**Cybersecurity procedures**	**Countermeasures of cyberattack in CMS**
1. Identify	• Control access to industrial control systems. • Create policies and procedures for cybersecurity.	• Observer control-based denial of service (DoS) [43]–[48]. • Cyberattack identification based on Machine Learning framework [49]–[51].
2. Protect	• Making a strong shield against possible cyberattacks. • Updating software systems.	• Dynamic data encryption for privacy preservation [52]–[54]. • Large-scale infrastructures (power grids) protection against cyberattacks [55]–[57].
3. Detect	• Detect unusual activities. • Maintain and monitor log activities.	• Secure control against intrusion detection [23], [35], [58], [59]. • Self-learning-based intrusion detection systems [60]–[62]. • Fault detection for multi-source integrated navigation using Deep Learning [63], [64]. • Spectrum sensing for malicious attack detection system [65]–[67].
4. Respond	• Immediate response to the cyberattack. • Directly notify stakeholders about the cyberattack.	• Automatic intrusion response systems for cyberattacks [35], [68]–[70]. • Cyberattack response in large-scale infrastructure (water treatment systems, power grids) [71], [72].
5. Recover	• Make an alternative backup of the database system. • Improve processes, procedures, and technologies	• Sensor effectiveness and system fidelity [34], [36], [73], [74]. • Cyberattack recovery schemes in smart grid restoration [75].

2.3 An overview of three proposed methods by linking CMS

Cybersecurity frameworks can be leveraged in a wide range of cybermanufacturing operations to make a robust shield against cyberattack space. Given the major challenges in AI-enabled cybermanufacturing systems, three research objectives are proposed in this dissertation work by incorporating cybersecurity frameworks (Table 2.1). The first research aims to detect the *in-situ* additive manufacturing (AM) process authentication problem using high-volume video streaming data (cybersecurity step 3). The second research work addresses the high-volume data stream problems in the multi-channel sensor fusion for diverse bearing fault diagnosis. By linking the second prosed method, the third research endeavour is aligned to recovery systems of multi-channel sensing signals when a substantial amount of missing data exists due to sensor malfunction or transmission issues (cybersecurity step 5). Overall, section 2.4 demonstrates state-of-the-art quality assurance methods for additive manufacturing related to the first proposed method. Section 2.5 illustrates the literature of the second and third proposed methods.

2.4 Quality assurance methods for AM authentication

The quality assurance methods for additive manufacturing processes can be briefly categorized as post-process quality inspection (section 2.4.1), *in-situ* monitoring (section 2.4.2), and anomaly detection based on AM process security (section 2.4.3).

2.4.1 Post-process quality inspection

Generally, AM post-process quality inspection methods fall into two major categories: destructive and non-destructive testing (NDT) techniques. In the destructive methods, AM-built parts are destroyed during either testing or sample preparation for material qualification. The most widely practiced destructive testing of AM fabricated parts includes tensile strengths (i.e., Young's

modulus, yield strength, ultimate tensile strength, and elongation), ductility test, and fatigue cycle performance [76]. In addition, material qualification/certification methods can be applied to evaluate the material properties (i.e., morphology, crystallography, and crack growth) of the AM parts [77], [78].

NDT techniques include visual inspection, eddy current and electromagnetic testing, liquid penetrant testing, ultrasonic testing, and X-ray radiography and computed tomography (CT)[79]–[83]. The advanced visual inspection techniques use optical metrological techniques in the geometry assessment of AM final parts [84], [85]. Moreover, the eddy current and electromagnetic techniques involved in detecting changes in dielectric and electronic properties of electrically conductive materials and therefore useful for detecting variations in capacitance due to the presence of crack, porosity, and associated defects in AM-built parts [83], [86]. Regarding material characterization and inspection, ultrasonic techniques are widely used for material testing and evaluation [82]. In addition, piezoelectric impedance-based measurements can be used as another NDE of AM part's dimensional alterations, positional changes, and internal porosity [87], [88]. With its higher resolution and accuracy compared to the fore mentioned NDT methods, X-ray Computed tomography (CT) is regarded as one of the most reliable part certification methods, especially used in internal structure certification (i.e., porosity, crack growth, etc.) [89], [90]. However, several practical challenges will limit the broader application of the X-ray CT techniques in AM part authentication. Firstly, the size of the X-ray CT machine chamber enforces a strict constraint in the dimension of the inspected parts. Therefore, it becomes infeasible to assess large-scale AM parts[87]. Secondly, X-ray CT scanning is a time-consuming procedure and the equipment is also rather costly, limiting its broad industrial applications [89]. Thirdly, as a post-manufacturing quality inspection method, the X-ray CT scans only detect the alteration after the

entire part is completely fabricated, which will significantly extend the lead time for AM part delivery once a part alteration is detected.

2.4.2 *In-situ* monitoring and anomaly detection

In-situ monitoring systems can be potentially used in AM part/process authentication by fusing heterogeneous sensing data. ASTM technical committee (F42) approved a complete list of AM process terminology regarding process monitoring and quality control of AM [91]. Based on multiple review studies, heterogenous sensing technologies have been extensively implemented in real-time process monitoring and control for metal-based AM processes, including acoustic emission, vibration, power consumption, temperature, and images [92]–[94]. The advanced sensing technologies generate high volume of data with various formats, including time series signals/curves, images, and point clouds. Univariate/multivariate time series are usually integrated for AM process monitoring and anomaly detection by leveraging various data fusion techniques, such as physics-based regression modelling and the Bayesian Dirichlet process (DP) mixture model.

Image streams include both optical and thermal image streams, which have been widely leveraged for *in-situ* defect detection. Due to the high volume and low signal-to-noise ratio in the image stream data, various dimension reduction methods are needed for data compression, including principal component analysis (PCA), multilinear PCA methods, Deep Neural Networks (DNNs) based feature extraction [95], and the image series modelling based feature extraction. In the laser-based AM process, *in-situ* process porosity can be detected through correlating the pyrometer images and porosity occurrence using a convolutional neural network (CNN) based data fusion technique [96]. In addition, a real-time layer-wise porosity prediction technique was also proposed by obtaining melt pool images, reducing the dimension of captured melt pool images

with tensor decomposition, and incorporating an SVM classifier for predicting the quality of melt pools [97]. In addition, in laser powder bed fusion (LPBF) AM, a computer vision algorithm is applied to detect anomalies during the powder spreading phase, and an unsupervised Machine Learning algorithm is used to classify those anomalies [98]. Moreover, a closed-loop proportional-integral-derivative (PID) feedback control scheme has been integrated for printing defect mitigation based on image data [99]. Furthermore, Cheng et al. [100]. investigated surface patterns by leveraging the image intensity information, where the surface defects are categorized into random defects and assignable defects due to specific process parameter shifts.

3D point clouds data characterizes the surface topology of AM parts for anomaly detection. For example, the deep forest Machine Learning methods have been used for *in-situ* layer-wise process shift detection [101]. A high-speed CMOS (complementary metal-oxide-semiconductor) camera has been used for real-time process monitoring for the layer-wise laser melting process [102]. Moreover, various optical sensors, including a structured-light scanner [101] and a 3D digital image correlation (DIC) camera, have been used to collect 3D point clouds of printed parts for anomaly detection [103]. In summary, state-of-the-art process monitoring and anomaly detection methods usually focus on detecting process changes/shifts due to unstable fabrication. However, malicious cyberattack-induced process alterations generally do not lead to inconsistent processes and thus cannot be easily detected by traditional process monitoring methods.

2.4.3 AM process security

Cyber-physical attacks in AM may occur in the designing, slicing, and manufacturing phases, and numerous studies have focused on the cyber-physical security of AM processes [104]. The literature on AM process security has been summarized through two aspects: 1) AM attack models; and 2) AM attack detection, which are introduced in subsections 2.4.3.1 and 2.4.3.2, respectively.

2.4.3.1 AM attack models

There are plenty of simulated AM attack models that have been investigated in the literature. Bridges et al. [105] summarizes the vulnerabilities in the entire AM process chain. Potential attacks to AM processes can target the digital files during all the phases in the AM processes. Firstly, quite a few studies attempted to alter the STL files in the design phase [13], [106], [107]. For example, additional features, such as internal voids, can be inserted into the STL file of the AM part, leading to compromised mechanical properties and catastrophic failures in the final product. Moreover, embedded defects can also be included by jetting a different material, leading to nonhomogeneous material properties in the final AM build [108]. Secondly, the slicing operations can be altered by AM attacks, generating an altered g-code file. The implemented alterations cover the whole set of slicing parameters, including printing direction, layer thickness, infill path and/or infill percentage [107], [109], [110]. In addition, AM attacks can also be directly applied to modify the g-code files. For example, Moore et al. [110] applied an attack on a firmware linked to the 3D printer to alter the g-codes by implementing the printing command in an altered order. Thirdly, AM attacks can also aim to alter AM process parameters, such as printing speed and fan cooling [111], extruding temperature, which can significantly affect the final part quality and reliability [102], [109].

2.4.3.2 Real-time AM attack detection

Side-channel analysis and monitoring have been widely used to detect AM part/process alteration by leveraging *in-situ* process measurements, such as acoustic emission, vibration, power consumption signals, and videos [107], [109], [112]–[114]. With the help of the above-mentioned techniques, a baseline of the signals is firstly established by AM parts which are verified to be normal, and then compared with a potentially altered part for alteration detection [115]. It is worth

noting that even though some sensors used for side-channel analysis are also widely used in process anomaly detection, the purposes of using those sensors are no longer assuring process quality but focusing on authenticating the process to its design intent. For example, Belikovetsky et al. [114]. conducted a side-channel authentication procedure to detect atomic modification (e.g., insertion, deletion, and modification of g-code commands) by analysing the digital audio signatures in real time. Liu et al. [106] leveraged the autoencoder method to compress the multi-stream acceleration signals to detect AM part/process alteration. Yu et al. [116] incorporated Machine Learning methods with the multi-modal side-channels for system state estimation for process authentication. Most of the side-channel monitoring studies are purely data-driven methods and thus heavily rely on a sufficiently large benchmark (or training) dataset which have already been verified to be unaltered. However, the uniqueness of AM processes in producing in high variety and low quantity makes it challenging to collect a sufficiently large benchmark dataset to train the data-driven models.

2.5 Condition monitoring of rotary machinery

In cyber-physical systems, a manufacturing plant can be operated and monitored simultaneously at the physical plants with the help of remotely controlled sensors that can collect real-time data for process monitoring and decision-making. In general, multi-sensor fusion incorporates multi-channel signals collected from the rotary machinery (RM) components for real-time condition monitoring and fault diagnosis. Different sensing technologies are being used in RM component's fault diagnosis purposes. While signal missing may prevail due to various reasons, including sensor sensitivity malfunction, sensor hardware malfunction, and transmission disruptions. In light of the above scenarios, section 2.5.1 demonstrates state-of-the-art of different sensing technologies for RM component's fault diagnosis. Subsequently, the state-of-the-art multi-

sensor fusion techniques can be divided into three levels, i.e., data-level, feature-level, and decision-level fusion [117], [118], which are briefly discussed in sub-section of 2.5.2. Section 2.5.3 seeks the literature of effective method for missing signal imputation for multi-channel sensing signals.

2.5.1 Sensing technologies in RM fault detection and diagnosis

Advanced sensing technologies provide new capacities for real-time fault detection and diagnosis of RM. Various sensors, including accelerometers, microphones, infrared imaging sensors, thermocouples, and power loggers, can be attached to the RM system to gather real-time process signals [119]–[122]. Among those sensing technologies, vibrations and acoustic emissions have been mostly used. Accelerometers are designed to measure vibration signals based on the severity of a shock event [123], [124]. The frequency range of accelerometer data is 8 Hz–15 kHz [120]. Generally, accelerometers are attached to the rolling component's surface for sensing real-time vibration signals that can be transferred via transmission cables and stored. Vibration signals are fundamentally comprised of frequency and amplitude that explain how frequently and how much severity of shock events are observed [125]. Multi-channel sensor fusion has been incorporated by using vibration signals for RM fault diagnosis [22], [126], [127]. Vibration signal-based spectrogram analysis is also useful for predicting tool wear in milling operation [128].

Microphone probes are placed adjacent to the RM for sensing real-time acoustics signals. Usually, a microphone probe can capture acoustics signals up to 20kHz [120]. Acoustics signature is measured based on bandwidth, power level (decibels), and voltage. Acoustics signal-based multi-channel sensor has also been used for machinery fault diagnosis [129], [130]. A thermocouple sensor is used for collecting temperature signals from machinery. Recently, temperature signal studies have gained popularity for health condition monitoring of RM [131]–

[133]. Usages of infrared imaging signal are also gained popularity for fault diagnosis of RM [119], [134], [135]. Several studies showed that a combination of vibration and acoustics signals is more effective than the individual signal analysis method. Moreover, vibro-acoustics based on multi-sensor fusion has also become popular for anomaly detection of RM [120], [122], [125], [136], [137].

2.5.2 Condition monitoring based on multi-channel sensor fusion

Multi sensor fusion incorporates multiple sensors of multi-channel signals for condition monitoring of RM. With regard to data managing level of abstraction, multi sensor fusion techniques can be divided into three levels of fusion, i.e., data-level fusion, feature-level fusion, and decision-level fusion [118], [119] and relevant state of the art has been discussed in the section 2.5.2.1, 2.5.2.2, 2.5.2.3, respectively.

2.5.2.1 Data-level sensor fusion

In the hierarchy of three levels of fusion (data-feature-decision), the lowest level of sensor fusion is the data-level that unifies signals from heterogeneous sensors [117], [138]. In data-level fusion methods, the most widely used techniques include digital signal processing, weighted average, coordinate transforms, and Kalman filtering, independent component analysis (ICA), multi-directional imaging with wavelet transform [139], [140], wavelets and hidden Markov models [141]. Meanwhile, SVM classifiers can also be used in data-level senor fusion for condition-based maintenance (CBM) of brushless DC motor (BLDC). For example, Prasad & Das [142] proposes multi-sensor data fusion for condition monitoring of BLDC motors by faulty signal classification based on the SVM method. Moreover, Liu & Wang [143] utilized a multi-sensor data-level fusion strategy based on the Cascade-Correlation (CC) neural network to diagnose

rotating imbalance.

However, there are some significant limitations associated with data-level fusion methods. In these methods, the communication load and processing complexity are usually very high [138]. Since the data level fusion exclusively relies on raw signal data that leads to a massive volume of data with increased dimensionality. Ultimately, an enormous volume of data transmission is required [140]. To address these limitations, an alternative approach is extracting key process features and then only transmitting those features for pattern recognition [138].

2.5.2.2 Feature-level sensor fusion

The feature-level fusion is an intermediate level of fusion that incorporates a combination of features extracted from heterogeneous sensors. Features are extracted by utilizing digital signal processing methods from heterogeneous sensors and then extracted features are fed into Machine Learning classifiers for pattern recognition/classification [137]. Implementing multi-sensor fusion can be challenging due to the complexity of data structure and their relationship, diversified sensor sampling frequency, and high dimensionality of the data [144]. In feature-level sensor fusion, several research gaps are prevailing in the anomaly detection and fault diagnosis of the rotary machinery. Multi-channel sensor fusion yields a high volume of data for condition monitoring, which is challenging for dimension reduction and feature extraction [145]. For high-dimensional data handling and feature extraction from a different source of signals, some widely used methods include Principal Component Analysis (PCA), High-order Statistics (HOS), and Independent Component Analysis (ICA) [146]–[149]. Usually, PCA is restricted to 1-D and 2-D data structures, while multilinear-PCA (MPCA) can handle 3-D or 4-D data structure, which is opted to multi-channel sensor fusion coupled with dimensionality reduction and feature extraction [148], [150]. Moreover, MPCA performs better than PCA for reducing data redundancy in high-dimensional

tensor space and extracting low-dimensional feature. Additionally, MPCA is essential for original signal features for all the tensor modes and in the meantime, it can retain as much as possible data variability in the original signals [150].

In contrast, Convolutional Neural Networks (CNNs) have recently become a popular algorithm for anomaly detection in RM. For example, X. Wang et al. [136] incorporated a 1D-convolutional Neural Network (CNN) based on vibration and acoustics sensor data for feature extraction and classification of bearing fault signals. Hao et al. [126] fused multi-sensors for bearing fault diagnosis implementing 1D-convolutional LSTM network. Chen et al. [22] implemented a duplet classifier using 1-D CNN for diagnosing bearing and rotor fault from a machinery fault simulator. Augmented data-based methods are utilized for RM fault diagnosis based on 1-D CNN architecture. However, this proposed method is also limited to the usage of vibration signals [151]. While multi-channel signals can also be stacked as 2-D structures and fed into 2-D CNNs [152]. Practically CNN network requires data robustness and time-intensive for training, validation, and testing purpose [22], [136], [153]. Additionally, In CNN architecture, parameter tuning is also quite time-consuming. Shao et al. [154] incorporated a deep autoencoder-based feature learning method for RM fault diagnosis. While this proposed method was limited to using only vibration signals.

2.5.2.3 Decision-level sensor fusion

Decision-level fusion involves making assumptions from a given homogeneous or heterogeneous sensor signal. It uses the information already extracted to a particular level of sensor data or feature-level processing to create a high-level decision [137], [155]. Bayesian estimation, Dempster-Shafer evidence theory, fuzzy logic, and classical inference are commonly used in decision-level fusion [140], [156], [157]. T. Wang et al. [157] incorporated decision-level sensor

fusion in order to monitor changes in rotary machinery conditions. They used multi-dimensional time-series analysis with autoregressive-integrated-moving-average (ARIMA) to detect rotary machine status. H. F. Wang & Wang [158] also used a decision-level sensor fusion methodology based on Dempster-Shafer algorithms for fault diagnosis of a diesel machine. Several studies suggested that feature-level fusion performs better than decision-level fusion, especially in classification methods [159]. In decision-level fusion, signal processing complexity is higher than in feature-level fusion. Moreover, data load capability in decision-level fusion can handle a small amount of information at a time [160]. Meanwhile, feature-level fusion performs better than decision-level fusion when heterogeneous sensor signals demonstrate highly diverse sampling frequency and non-stationary patterns.

2.5.3 Missing signal imputation for multi-channel sensing signals

A systematic state-of-the-art has been conducted based on mechanisms of missing data and different imputation methods. Section 2.5.3.1 primarily demonstrated the mechanisms of missing data and types of missing data patterns. In section 2.5.3.2, missing data imputation mechanisms are briefly discussed.

2.5.3.1 Missing data patterns and their generating mechanisms

Missing data problems are widespread in various applications, including industrial, social, biomedical, and weather science [161]–[163]. Missing data pattern describes the structure between missing entries and observed datasets. Missing data mechanisms refer to probable relations between the given variables and missing data [161]. Usually identifying the cause of missing data is usually somewhat difficult, but some inferences can help detect the missing data pattern [164]. Missing data occurrence can be responsible for various reasons, including sensor failure, sensor

aging, hardware malfunction, and transmission interference [165]–[168]. Missing data mechanism can be explained by three mutually exclusive categories: a. missing at random (MAR); b. missing completely at random (MCAR); c. missing not at random (MNAR)[161], [164], [169]. MAR relates the systematic link between one or more calculate variables and the probability of missing data [161], [170]. MAR occurrence is not random and explains the systematic missing. Additionally, MAR also explains the tendency for missing data that are correlated with associated variables [170]. MAR may occur due to transmission interruption that may end up with continuous missing signals [165]. For example, in a global navigation satellite system, time series data can be missing as MAR due to receiver crashes and power failure [171]–[173]. Offshore wind farms face difficulties of supervisory control and data acquisition systems when signals are missing due to harsh weather condition that led to sensor failure [174], [175]. MAR occurrence can also be found in wireless sensor networks due to sensor's node communication lost [176]. MCAR occurrence is completely haphazard, and the observed data can be assumed a random subsample of the complete data. The probability of MCAR data is unrelated of a given variable and also unrelated to other variables [170]. In contrast with MAR, MCAR data follow more restrictive conditions because of missing data is completely unrelated to the data [161], [170]. For instance, Micro-electromechanical systems (MEMS) senor malfunctioning can also be explained by MCAR behaviour based on its functional level that relates to several factors such as thermomechanical failure, electrical failure, and environmental failure [177]. Sound signal loss is also associated with MCAR due to malfunctioning microphone's electro-acoustic sensitivity [178], [179]. MNAR exists when the probability of missing data on a given variable is related to the value of itself. While other variables can also be controlled. MNAR is likely to be related to unobserved data. Similar to the MAR mechanism, there is no straightforward way to confirm that records are MNAR

without observing the entries of the missing variables [161].

2.5.3.2 Missing data imputation methods

Missing value recovery can be completed by different imputation techniques, including mean substitution that is replace by column mean or median [180]. K- nearest neighbour (KNN) is a widely used popular technique for missing data imputation [181], [182]. For example, KNN-based missing data imputation is implemented in wireless sensor networks missing sensor data [176]. Studies found that KNN performs better using continuous and discrete data [183]. However, the KNN-based imputation approach is time intensive since it searches for similar data patterns from its neighbours [184]. Different regression models, including multiple linear regression, logistics regression, and multinomial logistics regression, are used for missing data imputation. Regression models establish a relation between missing and existing features, where existing features are defined as predictors. However, this regression shows poor performance when it cannot correlate missing and existing features [184], [185]. Fuzzy c-means clustering techniques applied for missing data imputation that seeks the related features of a missing feature, and multiple linear regression and support vector regression are utilized for the particular features from fuzzy cluster [162]. While this proposed method failed to select automatic parameter selection in the regression model. In the state-of-the-art, deep learning models are widely used in the missing data imputation approach. Artificial neural network (ANN) is also a popular method for missing data imputation [163], [175]. Overfitting occurrences can be found in ANN when it shows good performance in the training dataset but fails to perform better in the testing dataset [175]. In the biomedical field, the missing data imputation approach is also popular by using recurrent neural network (RNN) [186], [187]. RNN showed better performance on missing pattern prediction. In [186] method, the proposed model was restricted to explain the correlation between missing pattern and prediction

task. Compressed Sensing -based on missing data imputation is utilized to condition monitoring of wind turbines [188]. However, Compressed Sensing-based on missing data imputation computational time is substantially high [189], [190].

Tensor completion methods are also widely used for high-dimensional missing data imputation. Tensor completion tasks can be categorized into several approaches, including decomposition/factorization-based, trace-norm based, and some other probabilistic methods. Tensor factorization coupled with tensor completion task is aligned to underlying factors based on partially observed data, and incorporating a multi-linear generative model assumption with fixed rank enables the prediction of missing entries [20], [191], [192]. Most widely used tensor decomposition approach includes CANDECOMP/PARAFAC (CP) and Tucker decomposition [193]–[197]. Tensor factorization with missing data has been conducted with several approaches including weighted least square problem termed as CP weighted optimization (CPWOPT) [198], CP with nonlinear squares (CPNLS) [203], geometric nonlinear conjugate gradient (geomCG) [199]. Still, the tensor factorization shows the tendency of overfitting because of incorrect tensor rank approximation and estimations of underlying factors that lead to poor predictive performance. In contrast, significant research work has also been conducted missing data imputation based on low-rank tensor completion (LRTC) [20]. Musialski et al. [19] incorporated Gaussian residual-based expectation maximization (EM) approach in Tucker decomposition with smoothing scheme coupled with fast low rank tensor completion (FaLRTC) and high accuracy low rank tensor completion (HaLRTC). Certain probabilistic CP decomposition techniques with Bayesian inference are also suggested for resolving missing entries estimation problem. This method is based on log-likelihood function that deletes the missing values from likelihood functions to deal with missing values and perform imputation [200]. However, tensor rank minimization based on

nuclear norm relies on parameter tuning approach, which performs over or under-estimating the true tensor rank. Tensor rank determination considers NP-complete because there is no simple algorithm for computer rank even with a given specific tensor [201]. Seeking the state-of-the-art solution, we have adopted a fully Bayesian CANDECOMP/PARAFAC (FBCP) factorization with low-rank determination method for missing data imputation from a machinery faults simulator (MFS) with diverse bearing faults signals.

CHAPTER III

SECURING CYBER-PHYSICAL ADDITIVE MANUFACTUING SYSTEMS BY *IN-SITU* PROCESS AUTHENTICATION USING STRAMLINE VIDEO ANALYSIS

3.1 Motivation and challenges

The increased interconnectedness in CPS has greatly enhanced the automation and productivity for modern manufacturing systems [3], in which cyber-physical security is of utmost importance for both quality and safety assurance. Malicious attacks can significantly affect a manufacturing system, altering machine parameters and product design, ultimately resulting in compromised products [107]. For example, the cyber-physical attack in the German steel mill in 2014 resulted in loss of control for the regulation of crucial parameters, leading to a massive blast of a furnace and even deaths of two workers [33]. Such catastrophic incidences of cyber-physical attacks show an urgent need in protecting manufacturing systems, identifying cyber threats, and detecting cyberattacks as soon as they occur. In the area of additive manufacturing (AM), the CPS provides unique opportunities for cost-effective production planning and control and enables new methods of collaboration where [202]–[204] all the AM machines can be operated and controlled remotely without human operator intervention [13]. The digital threads not only facilitate effective digital file sharing for design iteration, but also create significant risks of malicious cyberattacks, which are considered as a growing concern in AM systems. Maliciously alterations in the design files and process parameters could significantly affect final part's geometry, structural stability, mechanical performance, and functionality. What's worse, the layer-by-layer fashion of the AM

processes dramatically expands the victim space for potential alteration, leading to significantly changed structural compromises which are very challenging to detect [106], [205]. For example, internal structure changes, such as infill percentage, infill pattern, and unintended void addition, cannot be easily detected in the traditional Geometric Dimensioning and Tolerancing (GD&T) framework except for using either X-ray inspection, which are very time-consuming [89].

The AM process in a typical CPS is comprised of design (i.e., CAD design and STL file generation), slicing (i.e., G-codes generation), manufacturing (i.e., AM fabrication), and inspection [13], [112], [206]. Figure 3.1 illustrates the major steps of AM processes in a typical CPS, with red arrows illustrating the data/information transfer and green arrows showing the material flow. In general, cyberattacks may target on all the phases which involve data or information transfer, and typical attacks include inserting additional undesirable features in the original CAD design [207], altering processing parameters in generating the g-code [115], and injecting fake process data to mislead quality control decision making [206]. It is worth noting that most of the abovementioned process alterations can be manifested by the change in the printing path of the AM processes.

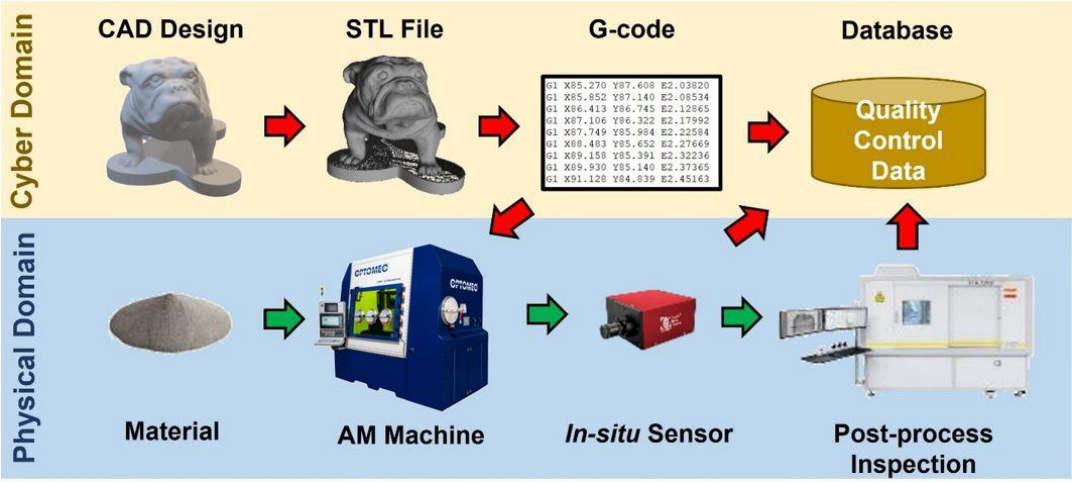

Figure 3.1 Material and information flow in CPS of AM.

Various types of sensors, including thermal couples, infrared (IR) imaging, accelerometers, microphones, power meters, can be potentially used to detect printing path alteration in AM processes [10], [15], [16]. However, the anomaly detection results are generally difficult to interpret. In addition, *in-situ* AM process authentication can be facilitated through optical imaging during the AM build. For example, in Figure 3.2, the images in the top row provide the slicing results of a square-shaped cross-sectional layer using different infill orientation angles, and the images in the bottom row illustrate their corresponding distribution of the texture orientation angles. It is observed that the layer-wise texture geometric feature distribution is largely determined by the printing path of the layer, and thus can be used as an informative and interpretable feature to detect printing path alteration.

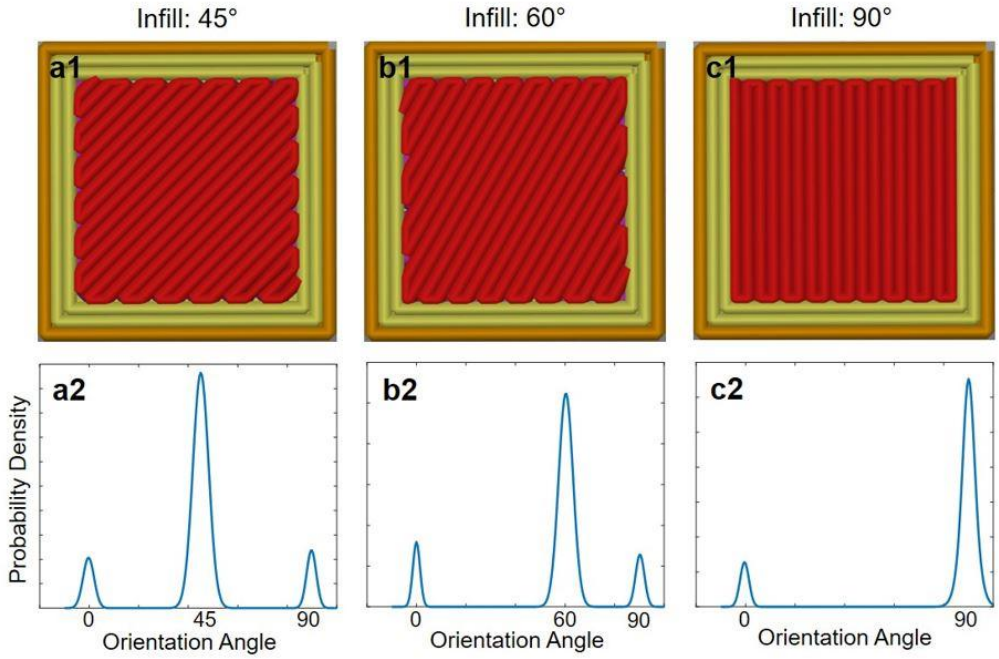

Figure 3.2 Different geometric feature distribution due to printing path alterations.

The texture of each layer can be observed by an optical camera which captures streamline video during the printing process. The advantages of the optical cameras include their cost-effectiveness and enhanced interpretability compared to other sensing technologies (such as acoustic emission and acceleration) [18], [208]. However, capturing a layer-wise image after fabricating each layer like the ones in the first row of Figure 3.2 may introduce significant interruptions in the fabrication, resulting in extended printing time. Therefore, an optical microscope attached to the extruder of the 3D printer can be used as an alternative solution to continuously capture streamline videos without any process interruptions [99]. Nevertheless, there are challenges in using the streamline videos captured by those optical cameras. First, the streamline video data are highly noisy due to the inevitable vibration of the microscope attached to the extruder during the printing process. Secondly, the field of view of the camera is changing since the camera is attached to the extruder, resulting in unstable contrast in the images over time and space due to dynamic light conditions. Third, the streamline videos are usually in high dimension and large volume. In summary, the *in-situ* process streamline video data are high-volume but low-quality. Therefore, how to extract low-dimensional informative layer-wise features from the streamline video with low signal-to-noise ratio (SNR) is an open challenge for effective AM process authentication.

3.2 Technical contribution of this work

In this paper, a new AM process authentication method is proposed to extract critical features from the high-volume, low-quality streamline videos collected from the camera attached to the printing head. The overall framework of the proposed methodology has three major phases: 1) Image-level texture feature extraction, which applies adaptive image filtering to retain the segmented regions (SRs) that demonstrate high contrast and are relevant to the printing path; 2)

Layer-wise feature extraction based on the geometric feature distribution of SRs, which constructs the layer-wise texture descriptor tensor (LTDT) to characterize the layer-wise texture distribution; and 3) Dimension reduction for the LTDTs based on multilinear principal component analysis (MPCA), which extracts low-dimensional features from the LTDTs to develop a Hotelling T^2 control chart for alteration detection. The effectiveness of the proposed method is evaluated by comparing with the benchmark method, which leverages the gray-level cooccurrence matrix (GLCM) to extract multivariate textural features [99] and the autoencoder technique to compress the high dimensional features.

The rest of the paper is organized as follows. Section 3.3 introduces the proposed methodology in detail. A case study based on the fused filament fabrication (FFF) process is demonstrated and the effectiveness of the proposed method is validated in Section 3.4. The conclusion and future work are summarized in Section 3.5.

3.3 Proposed methodology

In this section, subsection 3.3.1 firstly introduces the layer-wise texture descriptor tensor (LTDT), and subsection 3.3.2 describes the procedure of constructing the LTDT using the *in-situ* layer-wise video. Subsequently, subsection 3.3.3 introduces the dimension reduction for the LTDTs using multilinear principal component analysis (MPCA) and real-time monitoring based on the Hotelling T^2 control charting technique. The overall proposed methodology is illustrated in Figure 3.3.

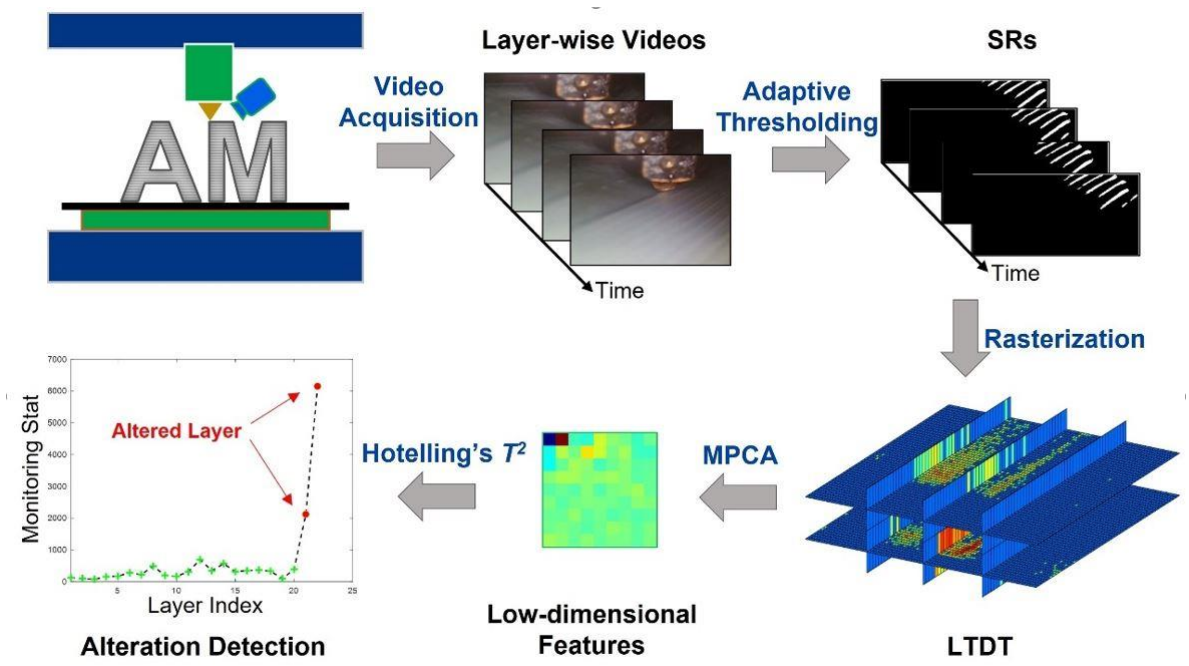

Figure 3.3 An overview of AM process authentication based on in-situ video analysis.

3.3.1 Layer-wise texture descriptor tensor

In CPS, most attacks aim to change the AM parts' internal structures, including infill pattern, infill percentage, and other structural features, since they are difficult to detect by traditional process monitoring methods. All the features of the internal structures are determined by the AM printing path, which can be captured by the textures observed from the *in-situ* videos. The layer-wise texture distribution contains critical information for the AM printing paths, and thus can be extracted to authenticate AM processes. Therefore, a novel layer-wise texture descriptor tensor is proposed in this section to characterize the distribution of the geometric features of the segmented texture.

Definition 1: Layer-wise texture descriptor tensor (LTDT). An R-th order LTDT of the l-th layer, denoted as $\mathcal{Z}_l \in \mathbb{N}_0^{D_1 \times \ldots \times D_R}$, is constructed with each mode representing the r-th geometric feature of the segmented textures obtained from the layer-wise imaging ($r = 1, 2, \ldots, R$), where

$\mathbb{N}_0$ denotes the set of non-negative integers. The LTDT contains the multivariate geometric feature distribution of the textures in the layer-wise image(s). It is worth noting that the LTDTs extracted from the same printing path design are assumed to be independently and identically distributed (i.i.d.) for the following reasons. First, the distribution of the LTDTs can be uniquely determined by the layer-wise printing path as illustrated in the Figure 3.2, and therefore, given the same printing path, the LTDTs should come from the same distribution. Second, the correlation between the consecutive layers can be regarded negligible if the microscopic camera is focused on the proximity of the printing nozzle. In this case, the observed printed texture in the area of interest will be mainly affected by the printing path of current layer, instead of its previous layer.

Proposed procedure for LTDT construction.

Without losing generality, this paper introduces the proposed approach for constructing LTDT when $R = 3$. However, the proposed method can be naturally extended to cases with $R > 3$. Image-level texture extraction and characterization. Each image frame in the video captured is firstly cropped to obtain the region of interest (ROI), which only retains the printed layer surface in the ROIs. Subsequently, adaptive image thresholding methods are used to adaptively segment the texture in the ROIs based on the local intensity in the neighbourhood of each pixel [208]. The locally adaptive algorithm automatically adjusts for varying background intensity levels due to spatially and temporally varying lighting conditions. As a result, it automatically discards the low contrast areas in the ROIs, which significantly reduces the data volume. The image pixels are segmented into two groups of regions: one group (labelled as “zero”) represents the background, and the other (labelled as “one”) represents segmented texture, which characterize the printing paths.

Definition 2: Segmented Region (SR). A segmented region is defined as a continuous region in the images that is labelled as "one" resulted from the adaptive image thresholding. The k-th SR captured from the l-th layer is denoted as SR_k^l, where $k = 1,2,\dots,K_l$ and K_l denotes the number of SRs in the l-th layer. For SR_k^l $(k = 1,2,\dots,K_l)$, four geometric features are calculated by approximating its shape using the ellipse that has the same second moment, as listed below.

1) **The Orientation** of SR_k^l is defined as the angle between the major axis of the SR's approximating ellipse and the horizontal axis, as illustrated in Figure 3.4. It approximates the printing path direction. The orientation of SR_k^l is denoted as o_k^l, where $-90° < o_k^l \leq 90°$ $(k = 1,2,\dots,K_l)$, where K_l denotes the number of SRs in the l-th layer.

2) **The Major Axis Length** of SR_k^l is defined as the length of the major axis of the approximating ellipse of the SR. It approximates the observed length of the printing path. The major axis length of SR_k^l is denoted as m_k^l $(k = 1,2,\dots,K_l)$. The unit of m_k^l can be the number of pixels in the captured image.

3) **The Minor Axis Length** of SR_k^l describes the length of the minor axis of estimating the ellipse of SR_k^l. It approximates the width of the printing path, and n_k^l $(k = 1,2,\dots,K_l)$ is used to denote the minor axis length of SR_k^l. The unit of n_k^l can be the number of pixels in the captured image.

4) **The Eccentricity** of SR_k^l describes the shape of SR_k^l. It is defined as the ratio of the distance between the foci and major axis length of the ellipse with the same second moment as SR_k^l, and denoted as ec_k^l $(k = 1,2,\dots,K_l)$ with $0 < ec_k^l < 1$. The smaller the ec_k^l value gets, the closer SR_k^l is to a circle. It is worth noting that the texture resulted from the printing path should demonstrate a large eccentricity value.

The reason for selecting those features is that their distribution over the entire layer provides critical information for the printing path of various AM processes. An illustration example of the geometric features of an SR is shown in Figure 3.4, where one SR is included as the white continuous region (labelled as “one”) on the black background (labelled as “zero”), the approximating ellipse is denoted as the golden ellipse, and the other relevant features, i.e., orientation, major and minor axis length of the SR, are also illustrated.

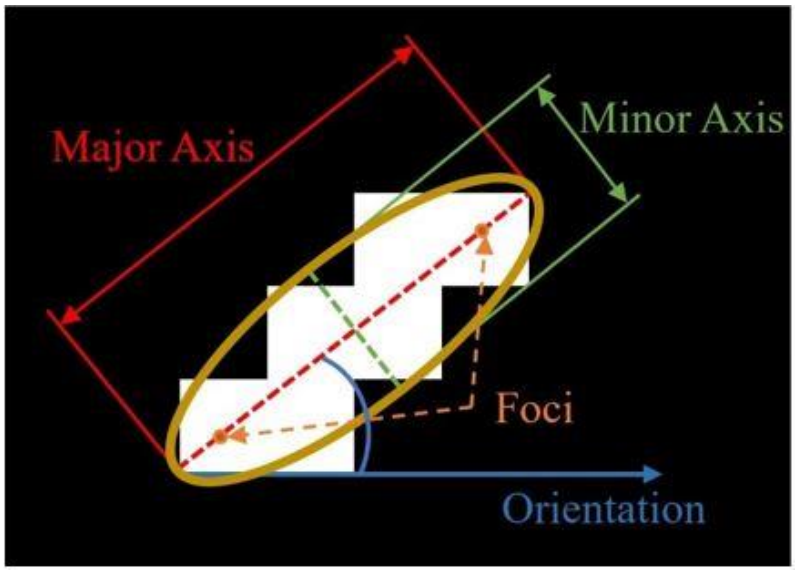

Figure 3.4 Illustrated of the extracted geometric features where the white region represents an SR segmented from the ROI.

In the proposed framework, the eccentricity is used to remove the irrelevant SRs which have a small eccentricity value, which are probably irrelevant to the printing path. This is based on the premise that the printing paths related SRs are generally long segments with a large length to diameter (L/D) ratio. The threshold for this region filtering can be determined based on the nominal printing path. For example, for parts with infill patterns resulting in long printing paths like the

rectilinear pattern, the filtering threshold should be set higher. In general, a larger threshold value for eccentricity will result in fewer filtered SRs.

3.3.2 Layer-wise geometric feature distribution characterization

To construct the LTDT, the distribution of SRs' geometric features is characterized using a rasterization algorithm. A set of regions are retained in the l-th layer after filtering, denoted as $\{(o_k^l, m_k^l, n_k^l) | ec_k^l \geq T_{ec}\}$, where o_k^l, m_k^l, n_k^l, and ec_k^l represents the orientation, major and minor axis length, and eccentricity of SR_k^l, respectively, and T_{ec} represents the threshold value of the eccentricity in the region filtering. Given a predefined bin size, i.e., (s_O, s_M, s_N), and ranges of these three features, i.e., (l_O, u_O), (l_M, u_M) and (l_N, u_N), the observed number of SRs in each bin can be calculated, where l_O, l_M, and l_N represent the lower bounds of the ranges and u_O, u_M, and u_N represent the upper bounds of the ranges, respectively. Without losing generality, The rasterization algorithm to generate the LTDTs is illustrated in Figure 3.5. As a result, the LTDT is represented as a 3rd-order tensor $\mathcal{Z}_l \in \mathbb{N}_0^{D_O \times D_M \times D_N}$, where $D_O = \left\lceil \frac{u_O - l_O}{s_O} \right\rceil$, $D_M = \left\lceil \frac{u_M - l_M}{s_M} \right\rceil$ and $D_N = \left\lceil \frac{u_N - l_N}{s_N} \right\rceil$. In addition, each element in $\mathcal{Z}_l$ can be calculated in Eq. (3.1)

$$\sum_{k=1}^{K_l} \left[\begin{pmatrix} l_O + (o-1)s_O \\ l_M + (m-1)s_M \\ l_N + (n-1)s_N \end{pmatrix} \leq \begin{pmatrix} o_k^l \\ m_k^l \\ n_k^l \end{pmatrix} < \begin{pmatrix} l_O + os_O \\ l_M + ms_M \\ l_N + ns_N \end{pmatrix} \right] \tag{3.1}$$

where $[\cdot]$ refers to the Iverson bracket, i.e.,

$$[Q] = \begin{cases} 1, \text{if } Q \text{ is true} \\ 0, \text{if } Q \text{ is false} \end{cases}$$

where $1 \leq o \leq D_O$, $1 \leq m \leq D_M$ and $1 \leq n \leq D_N$, and K_l represents the total number of SRs in the l-th layer. Due to the sparsity and high dimensionality of $\mathcal{Z}_l$, it is necessary to further extract

the key information from $\mathcal{Z}_l$ for monitoring. Given its effectiveness in reducing the dimensionality of high-dimensional tensors, MPCA is used in dimension reduction of the LTDTs for process alteration detection.

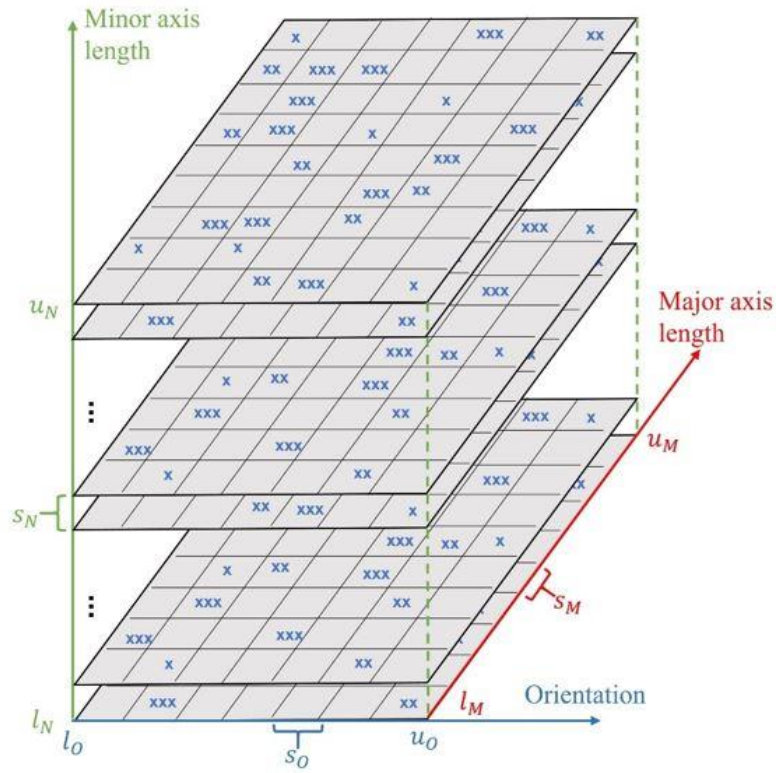

Figure 3.5 Rasterization to generate the LTDTs.

3.3.3 Dimension reduction from geometric feature distribution

The LTDT, denoted as $\mathcal{Z}_l \in \mathbb{N}_0^{D_O \times D_M \times D_N}$, is a 3rd-order tensor with the following properties: 1) all the elements in the tensor are non-negative integers and the distribution of those elements is right skewed; 2) the LTDTs are of high dimension and the elements in the tensor are highly correlated; 3) The LTDTs are sparse tensors, which means there are a lot of zeros in the tensor. Therefore, dimension reduction methods are needed to compress the LTDTs and extract critical

features for effective process authentication. To avoid numerical issues in tensor decomposition, a log-link function is used to transfer the original elements in the LTDTs to reduce its skewness. In addition, to retain the same lower bound (i.e., zero) and sparsity of the tensor after transformation, each element in $\mathcal{Z}_l$ is shifted by 1, as illustrated in Eq. (3.2). Based on the standard multilinear algebra, the tensor $\mathcal{X}_l$ can be expressed as in Eq. (3.3).

$$\mathcal{X}_l = \log\left(\mathcal{Z}_l + 1\right) \tag{3.2}$$

$$\mathcal{X}_l = \mathcal{G}_l \times_1 \mathbf{U}_O \times_2 \mathbf{U}_M \times_3 \mathbf{U}_N \tag{3.3}$$

where $\mathcal{G}_l = \mathcal{X}_l \times_1 \mathbf{U}_O{}^T \times_2 \mathbf{U}_M{}^T \times_3 \mathbf{U}_N{}^T$, and $\mathbf{U}_O$, $\mathbf{U}_M$ and $\mathbf{U}_N$ are orthogonal projection matrices corresponding to the mode of the orientation, major and minor axis length, respectively. $\mathcal{G}_l$ represents the core tensor with reduced dimension $d_O \times d_M \times d_N$, where $0 < d_O < D_O$, $0 < d_M < D_M$ and $0 < d_N < D_N$, and $\mathcal{G}_l$ can be used as the extracted features. Since the LTDTs are usually high-dimensional and sparse, tensor decomposition can be used to extract low dimensional features for alteration detection. Multilinear principal component analysis (MPCA) determines a multilinear projection that captures most variations in the original LTDTs. The objective of MPCA is to find the projection matrices, i.e., $\mathbf{U}_O$, $\mathbf{U}_M$ and $\mathbf{U}_N$, which maximize the total tensor scatter in $\mathcal{G}_l$, denoted by $\psi_{\mathcal{G}}$, as illustrated in Eq. (3.4).

$$\{\mathbf{U}_O, \mathbf{U}_M, \mathbf{U}_N\} = \arg\max_{\mathbf{U}_O, \mathbf{U}_M, \mathbf{U}_N} \psi_{\mathcal{G}} \tag{3.4}$$

To solve the optimization problem in Eq. (4), the problem is decomposed into a series of projection subproblems, where the projection matrices are iteratively updated. Figure 3.6 illustrates the pseudocode for implementing the MPCA algorithm, which is adapted from [197].

Input: A set of nominal layers' geometric features distribution $\{\mathcal{Z}_l \in \mathbb{R}^{D_O \times D_M \times D_N}, l = 1,2,\dots,L_{tr}\}$

Output: Low dimensional features $\mathcal{G}_l$ and projection matrices $\widetilde{\mathbf{U}}_O \in \mathbb{R}^{D_O \times d_O}$, $\widetilde{\mathbf{U}}_M \in \mathbb{R}^{D_M \times d_M}$ and $\widetilde{\mathbf{U}}_N \in \mathbb{R}^{D_N \times d_N}$

Algorithm:

Step 1 (Element-wise Transferring and Centering):

1.1 Transfer the original tensor as $\{\mathcal{X}_l = \log(\mathcal{Z}_l + 1)\}$

1.2 Center the benchmark samples as $\{\widetilde{\mathcal{X}}_l = \mathcal{X}_l - \overline{\mathcal{X}}, l = 1,2,\dots,L_{tr}\}$, where $\overline{\mathcal{X}} = \frac{1}{L_{tr}}\sum_{l=1}^{L_{tr}} \mathcal{X}_l$.

Step 2 (Initialization):

2.1 Calculate the eigen-decomposition of $\mathbf{\Phi}^{(j)*} = \sum_{l=1}^{L_{tr}} \widetilde{\boldsymbol{X}}_{l(j)} \widetilde{\boldsymbol{X}}_{l(j)}^T$ $(j = 1,2,3)$ and set $\widetilde{\mathbf{U}}_O$, $\widetilde{\mathbf{U}}_M$ and $\widetilde{\mathbf{U}}_N$ to consist of the eigenvectors corresponding to the most significant d_O, d_M and d_N eigenvalues, respectively. Here $\widetilde{\boldsymbol{X}}_{l(j)}$ represents the unfolded matrix of $\widetilde{\mathcal{X}}_l$ along the j-th mode.

2.2 Calculate $\{\tilde{\mathcal{G}}_l = \widetilde{\mathcal{X}}_l \times_1 \widetilde{\mathbf{U}}_O{}^T \times_2 \widetilde{\mathbf{U}}_M{}^T \times_3 \widetilde{\mathbf{U}}_N{}^T, l = 1,2,3\dots,L_{tr}\}$,

2.3 Calculate $\psi_{\mathcal{G}_0} = \sum_{l=1}^{L_{tr}} \|\tilde{\mathcal{G}}_l\|_F^2$

Step 3 (Optimization):

For $p = 1{:}P$

Update $\widetilde{\mathbf{U}}_O$: Set the matrix $\widetilde{\mathbf{U}}_O$ to consist of the d_O eigenvectors of the matrix $\mathbf{\Phi}^{(1)} = \sum_{l=1}^{L_{tr}} \widetilde{\boldsymbol{X}}_{l(1)} \cdot \widetilde{\mathbf{U}}_O \cdot \widetilde{\mathbf{U}}_O{}^T \cdot \widetilde{\boldsymbol{X}}_{l(1)}^T$, corresponding to the largest d_O eigenvalues.

Update $\widetilde{\mathbf{U}}_M$: Set the matrix $\widetilde{\mathbf{U}}_M$ to consist of the d_M eigenvectors of the matrix $\mathbf{\Phi}^{(2)} = \sum_{l=1}^{L_{tr}} \widetilde{\boldsymbol{X}}_{l(2)} \cdot \widetilde{\mathbf{U}}_M \cdot \widetilde{\mathbf{U}}_M{}^T \cdot \widetilde{\boldsymbol{X}}_{l(2)}^T$, corresponding to the largest d_M eigenvalues.

Update $\widetilde{\mathbf{U}}_N$: Set the matrix $\widetilde{\mathbf{U}}_N$ to consist of the d_N eigenvectors of the matrix $\mathbf{\Phi}^{(3)} = \sum_{l=1}^{L_{tr}} \widetilde{\boldsymbol{X}}_{l(3)} \cdot \widetilde{\mathbf{U}}_N \cdot \widetilde{\mathbf{U}}_N{}^T \cdot \widetilde{\boldsymbol{X}}_{l(3)}^T$, corresponding to the largest d_N eigenvalues.

Calculate $\{\tilde{\mathcal{G}}_l, l = 1,2,3\dots,L_{tr}\}$ and $\psi_{\mathcal{G}_p}$.

If $\psi_{\mathcal{G}_p} - \psi_{\mathcal{G}_{p-1}} < \varepsilon$, break and output projection matrices, $\widetilde{\mathbf{U}}_O$, $\widetilde{\mathbf{U}}_M$ and $\widetilde{\mathbf{U}}_N$.

Step 4 (Projection): For any newly collected layer, the low-dimensional features are calculated as $\{\mathcal{G}_l = (\mathcal{X}_l - \overline{\mathcal{X}}) \times_1 \widetilde{\mathbf{U}}_O{}^T \times_2 \widetilde{\mathbf{U}}_M{}^T \times_3 \widetilde{\mathbf{U}}_N{}^T, l = 1,2,3\dots,L_{tr}\}$.

Figure 3.6 The MPCA algorithm for projection matrix estimation.

Given training data set with several verified healthy layers, the projection matrices can be estimated based on the algorithm in Figure 3.6, and low-dimensional features can be extracted to

describe the major variability in the LTDTs. Subsequently, the Hotelling T^2 control charting scheme can be applied to the extracted multivariate features [209]. Based on the features extracted from the training set, the covariance matrix (denoted as $S_{\mathcal{G}}$) can be estimated. When a new part is fabricated and the streamline video data collected, the Hotelling T^2 monitoring statistics of the l-th layer is calculated in Eq. (3.5).

$$T_l^2 = \mathrm{vec}(\mathcal{G}_l)^T \left(S_{\mathcal{G}}\right)^{-1} \mathrm{vec}(\mathcal{G}_l) \tag{3.5}$$

where $\mathrm{vec}(\cdot)$ denotes the function to vectorize the resulting low dimensional tensor, and $\mathcal{G}_l$ denotes the low-dimensional features extracted based on the projection matrices obtained from the training data. The upper control limit (UCL) of the control chart can be determined as the empirical $100 \times (1-\alpha)\%$ quantile of the monitoring statistics based on the Phase I data, where α is the pre-determined Type I error rate. Process authentication alarm rule is that whenever the monitoring statistic T_l^2 exceeds the pre-determined UCL, the printing path of the l-th layer of the tested build is altered, and the printing process should be terminated for further investigation.

3.4 Case study

This section investigates the performance of the proposed methodology based on a fused filament fabrication (FFF) process which is equipped with a microscope camera to capture streamline videos. The experimental setup and data collection are described in Section 3.4.1, and the results are summarized and discussed in Section 3.4.2.

3.4.1 Experimental setup and data collection

An FFF-based 3D printer (Prusa i3 MK3S) was used for data collection. A Teslong Portable MS 100 USB microscope was attached to the extruder head and focused on the nozzle tip while

continuously capturing streamline videos from the fabricated surface. The camera's frame rate is 25 Hz, and the resulting resolution of each frame is 480×640. Figure 3.7 (a) and (b) illustrate the experimental setup with the real-time video shown on the screen of the laptop. In addition, Figure 3.7 (c) shows five example frames captured from the fabrication of one layer with solid infill of the rectilinear pattern; and Figure 3.7 (d) shows example image frames captured from the fabrication of one layer with a square shaped hollow feature included. It can be observed that the image contrast varies significantly within the same image and among multiple images.

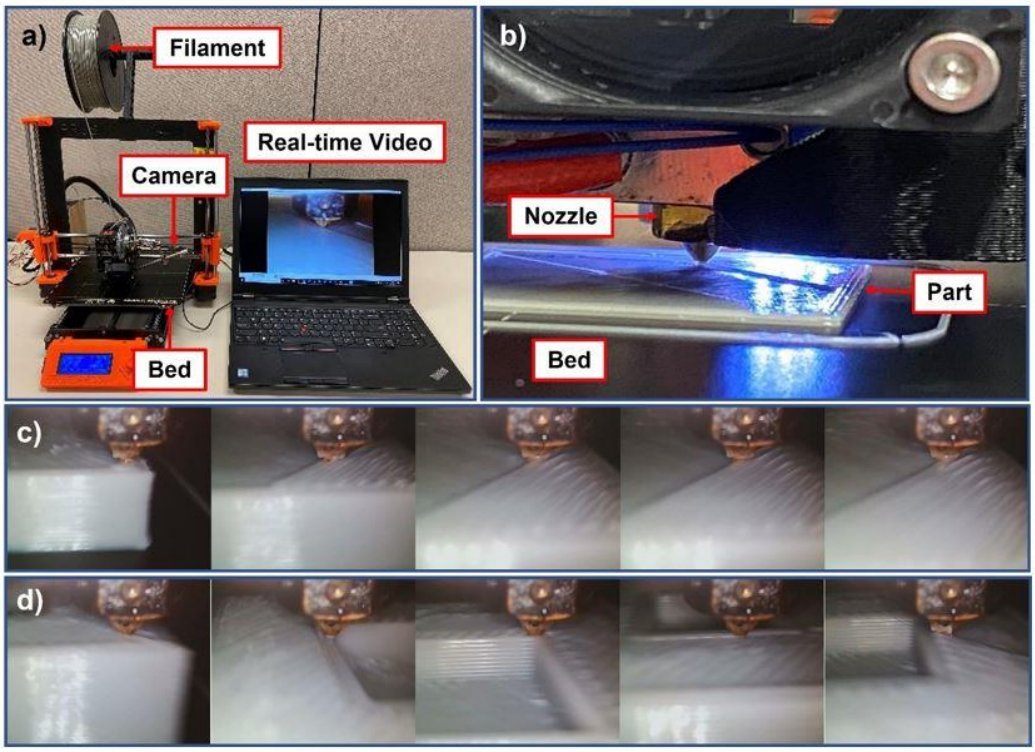

Figure 3.7 Demonstration of the experimental setup (a and b) and sample images (c and d).

This case study intends to simulate two scenarios of the cyberattacks, i.e., varying the infill orientation (Group B) and altering the STL files (Group C). As illustrated in Figure 3.9, both cyberattack scenarios considered result in changes the printing path, and thus alter the entire AM

chain starting from the slicing phase. Three different groups of parts were fabricated, in which Group A is the nominal part, and Group B and C are altered parts with printing path rotated and undesired feature added, respectively. Table 3.1 summarizes the part dimension and infill orientation of the three groups. The feedstock material used was the filament of polylactic acid (PLA) with a cross-sectional diameter of 1.75 mm. The printing parameters used for all the parts are summarized in Table 3.2, which remain the same and therefore excluded from the analysis in this study. Four parts in total were fabricated, among which two parts belong to Group A, and the other two are from Group B and C, respectively. Figure 3.8 illustrates the cross sections of the three printed parts which belong to Group A, B, and C, respectively.

Figure 3.8 Illustration of three groups of parts.

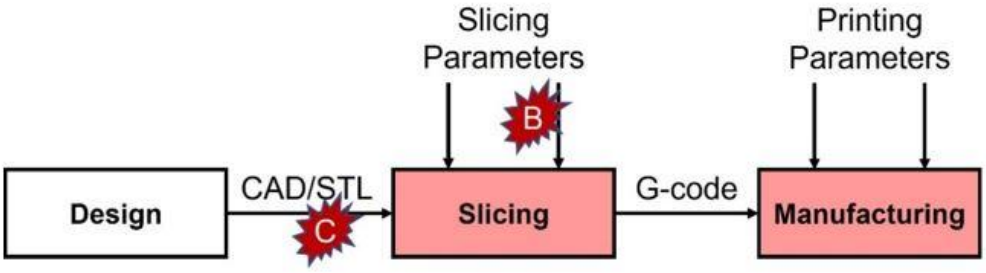

Figure 3.9 Cyberattack scenarios simulated in the case study.

Table 3.1 Model dimensions and infill parameters.

Part Group	A (Nominal)	B (Altered)	C (Altered)
Dimensions (L × W × H) (mm)		30 × 30 × 10	
Undesired feature (L× W × H) (mm)	NA	NA	10 × 10 × 5
Infill orientation (degree)	45	90	45
Build time (second)	3,761	3,812	3,550

Table 3.2 Printing parameters shared by all the three groups.

Parameter	Value	Parameter	Value
Infill (%)	100	Printing speed (mm/s)	20
Extrusion width (mm)	0.5	Nozzle temperature (°C)	200
First layer thickness (mm)	0.4	Bed temperature (°C)	65
Layer thickness (mm)	0.3	Number of layers	33

3.4.2 Results and discussion

This section demonstrates results and discussion of this case study. Selection of benchmark method and parameter estimation for both proposed and benchmark methods discuss in section 3.4.2.1 and 3.4.2.2, respectively.

3.4.2.1 Benchmark method selection

The image-based monitoring and control method for the FFF process proposed in Liu et al. [101] was adopted as the benchmark method for alteration detection, because it is the most recent study on anomaly detection by leveraging texture analysis of real-time optical images. In the benchmark method, a variety of textural statistics were extracted based on the gray-level co-occurrence matrix (GLCM), and the multivariate statistics are compressed using the autoencoder technique [210], which has been demonstrated as an effective data compression method in [106]. This method is mainly focused on the defect detection and its effectiveness has been validated in [99] in through the comparison between the conventional Machine Learning approaches. It is

worth noting that the benchmark method is proposed for image-wise anomaly detection. Therefore, to achieve layer-wise alteration detection, the arithmetic mean of the image-wise monitoring statistics across each entire layer was used as the layer-wise monitoring statistic. Another potential benchmark method is proposed by Bui and Apley [211], which proposed a stochastic textured surface modelling approach for high-dimensional images. However, the method is not applicable to the problem in this paper, because their modelling approach requires to establish a benchmark textured surface for monitoring and anomaly detection. In the streamline video captured from the 3D printing process, it will be quite cumbersome to find the unique benchmark textured surface for all the images due to dynamic nature of the ROIs captured. Therefore, this method is not adopted as a second benchmark method to compare with the proposed approach.

3.4.2.2 Parameter estimation for both methods

For both methods, image pre-processing was implemented. For the proposed method, the ROI was cropped by removing the region above the nozzle tip, resulting in the ROIs of size 315×637. For the benchmark method, the ROI cropping suggested in [99], resulting in the ROIs of size 80×80. All the 33 layers of each part except for the first layer were used since the textural information in the first layer is not comparable with any of the subsequent layers. For both methods, all the layers of the first part in Group A were used as the training data set for necessary parameter estimation. This includes projection matrices estimation in MPCA and covariance matrix estimation for the T^2 monitoring statistics for the proposed method, and the training of autoencoder for the benchmark method. Furthermore, randomly selected 75% layers of the second part in Group A were used as Phase I data for control limit determination. The remaining 25% layers of the second part of Group A and all the layers of Group B and C were used as the Phase II data to evaluate the performance. The random split between Phase I and Phase II data was

repeated for 100 times, and the average performance was summarized. It is also worth noting that, for the proposed method, the parameter estimation and UCL determination for the odd and even number of layers need to be separated, because the texture distributions of the odd and even number of layers in Group A are different. In Phase II, whenever the monitoring statistic exceeds the pre-determined UCL, the control chart will signal and that corresponding layer is detected as an altered layer; otherwise, the layer is regarded as unaltered. A test run example is illustrated in Figure 3.10.

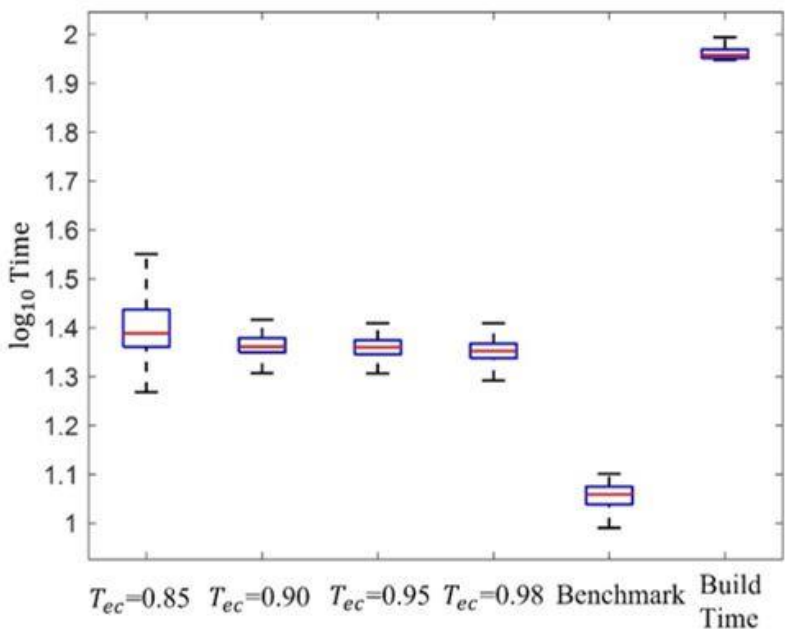

Figure 3.10 Average layer-wise computation time comparison.

3.4.3 Results comparison and discussion

The performance metrics used to evaluate the proposed and benchmark methods include recall, precision, F-score, and overall accuracy, which are defined in the Eq. (3.6), Eq. (3.7), Eq. (3.8) and Eq. (3.9), respectively in the below based on the elements in the confusion matrix.

$$\text{Recall} = \frac{\text{TP}}{\text{TP} + \text{FN}} \tag{3.6}$$

$$\text{Precision} = \frac{\text{TP}}{\text{TP} + \text{FP}} \tag{3.7}$$

$$\text{Fscore} = 2 \times \frac{\text{Precision} \times \text{Recall}}{\text{Precision} + \text{Recall}} \tag{3.8}$$

$$\text{Accuracy} = \frac{\text{TP} + \text{TN}}{\text{TP} + \text{TN} + \text{FP} + \text{FN}} \tag{3.9}$$

where true positive (TP) denotes the number of altered layers which are predicted accurately as altered, whereas true negative (TN) represents the unaltered layers which are accurately predicted as unaltered. In addition, false-negative (FN) denotes inaccurate prediction of altered layers as unaltered, while false positive (FP) represents inaccurate prediction of the layers which are unaltered but predicted as altered. $\text{F} - \text{score}$ is the harmonic mean of precision and recall, and the overall accuracy is the percentage of accurately classified layers within all the Phase II layers evaluate. To assess the feasibility for real-time analysis, the computational efficiency of the proposed and benchmark methods is also evaluated and compared.

There are two tuning parameters used in the proposed method: 1) the threshold value of eccentricity used in the SR filtering, denoted as T_{ec}; and 2) the number of MPCs retained in the monitoring statistics, denoted as d_{pc}. To test the robustness of the proposed method, both tuning parameters are varied, and the performance of the proposed method is summarized in Table 3.3. It can be observed that the proposed method outperforms the benchmark method within the wide range of the tuning parameters for all the performance metrics evaluated. Even though the proposed method demonstrates good performance in all the combinations of tuning parameters

tested, some trends are still visible in Table 3.3. Based on the F-score values, the best performing rows within each given T_{ec} value have been bolded in Table 3.3. It can be observed that when the T_{ec} value is small to medium (i.e., 0.85, and 0.9), the proposed method performs best using relatively large d_{pc} values (i.e., 10). When the T_{ec} value is medium to large (i.e., 0.95 and 0.98), the proposed method performs best using relatively small d_{pc} values (i.e., 5). The reason behind this observation is that smaller (larger) T_{ec} values, in general, lead to more SRs retained and less sparse LTDTs. Therefore, more (fewer) MPCs are potentially needed to capture the major variations in the extracted LTDTs for effective alteration detection.

The major reason for the inferior performance of the benchmark method is that their method works under the underlying premise that the GLCM based features can fully characterize the textured surfaces captured. However, in the real-world AM fabrication, the lighting condition and image contrast are varying significantly over time due to the high printing speed, making the GLCM features limited in characterizing these complex stochastic textured surfaces. To evaluate the computational efficiency of the proposed method, the average computation time is summarized in Figure 3.10. Since the different d_{pc} values ranging from 2 to 12 do not significantly affect the computation time, the computation time is only compared based on different T_{ec} values (Intel® Core™ Processor i7-7700 CPU @ 3.60GHz). It can be observed that even though the proposed method is less efficient compared with the benchmark method, both are significantly shorter than the layer-wise build time. Within different tuning parameters used in the proposed method, it is also observed that when the T_{ec} value is small, the variation of computation time is higher than when the T_{ec} value is medium or large. Furthermore, the average computation time decreases slightly as the T_{ec} increases, because the number of retained SRs will decrease given a higher threshold value of T_{ec}. In addition, it is also worth noting that given the same camera, the layer-

wise computation time of the proposed method is determined by the size of the video, which is proportional to the layer-wise build time. For the proposed method, the computation time stays between 25.0% and 28.3% of the layer-wise build time, depending on the tuning parameter used.

Table 3.3 Results summary of the proposed and benchmark method.

T_{ec}	d_{pc}	Accuracy	Precision	Recall	F-score
0.85	2	95.8%	95.5%	98.4%	96.9%
	5	86.1%	87.9%	91.8%	89.8%
	8	95.0%	93.1%	100.0%	96.4%
	10	**97.8%**	**96.8%**	**100.0%**	**98.4%**
	12	84.3%	91.3%	84.6%	87.8%
0.9	2	92.6%	93.0%	96.3%	94.6%
	5	89.4%	87.7%	97.9%	92.5%
	8	94.3%	92.2%	100.0%	95.9%
	10	**96.4%**	**94.9%**	**100.0%**	**97.4%**
	12	93.5%	91.2%	100.0%	95.4%
0.95	2	90.8%	87.8%	100.0%	93.5%
	5	**95.0%**	**96.0%**	**96.8%**	**96.3%**
	8	86.5%	95.4%	83.9%	89.3%
	10	82.7%	90.0%	83.4%	86.5%
	12	84.4%	90.3%	86.0%	88.0%
0.98	2	84.2%	96.2%	79.8%	87.1%
	5	**93.0%**	**90.6%**	**100.0%**	**95.0%**
	8	90.7%	93.7%	92.4%	93.0%
	10	88.1%	91.8%	90.4%	91.0%
	12	84.3%	91.2%	84.7%	87.8%
Benchmark		72.5%	84.0%	62.0%	71.0%

3.5 Conclusion and future work

Cybermanufacturing systems accelerate the communication, prototyping, and sharing of digital files to optimize productivity in AM process. The layer-by-layer fashion of AM fabrication significantly makes a large variety of process/part alterations possible and therefore extensively enlarge the vulnerability space. Most cyberattacks focus on altering the printing path, so that the internal structure of the product can be changed. This will lead to deteriorated mechanical

properties and compromised product functionality for mission-critical structures. What's worse, it may even cause catastrophic accidents for the operators for functional AM components. This paper proposes a new real-time process authentication method based on layer-wise streamline video data. By integrating adaptive image thresholding, the multivariate distribution of texture geometric features is extracted. In addition, a novel layer-wise AM process descriptor, i.e., the layer-wise texture descriptor tensor (LTDT), is constructed for process authentication. Multilinear principal component analysis (MPCA) is used to extract low-dimensional features from those high-dimensional and sparse LTDTs. To evaluate the effectiveness of the proposed methodology, a case study based on an FFF process is used. The proposed method outperforms the benchmark method in terms of alteration detection accuracy, while the computational efficiency remains satisfactory for real-time alteration detection.

This study can be potentially extended in the following three directions. First, the sensitivity of the alteration detection will be further quantified for major part alteration categories, such as undesired feature added and rotated printing orientation. Second, under the proposed framework, AM parts with diversified geometric features, including different shapes, infill patterns, and infill percentages, will be considered, and their performance will be evaluated. Third, a Machine Learning scheme can use to categorize different types of printing path alterations for fault diagnosis and impact assessment of the cyberattacks.

CHAPTER IV

MULTI-CHANNEL SENSOR FUSION FOR REAL-TIME BEARING FAULT DIAGNOSIS BY FREQUENCY-DOMAIN MULTILINEAR PRINCIPAL COMPONENT ANALYSIS

4.1 Motivation and challenges

The health conditions of rotary machinery have a significant impact on the functionality of various rotary machinery (RM), including motors, gearboxes, bearings, and connecting shafts [212], [213]. Faults in RM can lead to disruption of daily manufacturing operations, significant economic loss, and even catastrophic accidents. Therefore, timely fault detection and diagnosis are crucial for RM. In recent years, condition monitoring of RM has drawn huge attention [214], which can help to assure productivity, reliability, and safety while reducing maintenance costs [213]. The increased computation efficiency has made it possible to perform real-time condition monitoring based on multi-channel signals. Multi-sensor fusion is referred to as the synchronization of data to predict the real-time system condition from heterogeneous sensors [139], including accelerometers, microphones, and power loggers, which can be attached to the RM systems to simultaneously gather process data in real-time [122], [123], [215]. Multi-channel sensor fusion usually first extracts key process features from the raw signals. Subsequently, supervised, or unsupervised Machine Learning algorithms can be applied to the extracted features for fault detection and diagnosis [216]–[218]. Moreover, vibro-acoustics based on multi-sensor fusion has also become popular for the anomaly detection of RM [123], [137], [138], [215].

Real-time fault detection of RM rolling is a very complex problem. The complexity of the problem is two-folded. First, an RM is usually made up of multiple components, and any individual component's failure will have a significant impact on the RM and thus affect the entire system. Second, each component can potentially demonstrate multiple different faults. As illustrated in Figure 4.1, an RM can be comprised of multiple bearings with various possible faults. All the faults and their combinations result in a high dimensional RM fault space, which calls for accordingly large training data sets to train a reliable Machine Learning model. Hence, multi-channel sensor fusion for RM fault diagnosis requires a high volume of data for condition monitoring tasks, and thus training a reliable Machine Learning model can be costly. A significant number of studies have been involved in handling a large volume of the dataset with limited variety of faults for anomaly detection and diagnosis in RM. However, most of the fault detection and diagnosis methods requires very large training datasets which might not be practical for real-world RM applications [137], [138], [157], [218]–[220]. To bridge the gap, this study has been involved in utilizing a mixture of bearing faults scenarios along with the multi-sensor fusion of vibration and acoustic signals and using a significantly less amount of training and test dataset. Multilinear principal component analysis (MPCA) method is proposed for low-dimensional feature exaction for anomaly detection whereas combination of good bearing and four different faulty bearings scenarios are structured Figure 4.1. Ultimately, the robustness of this work can be evaluated with existing research works.

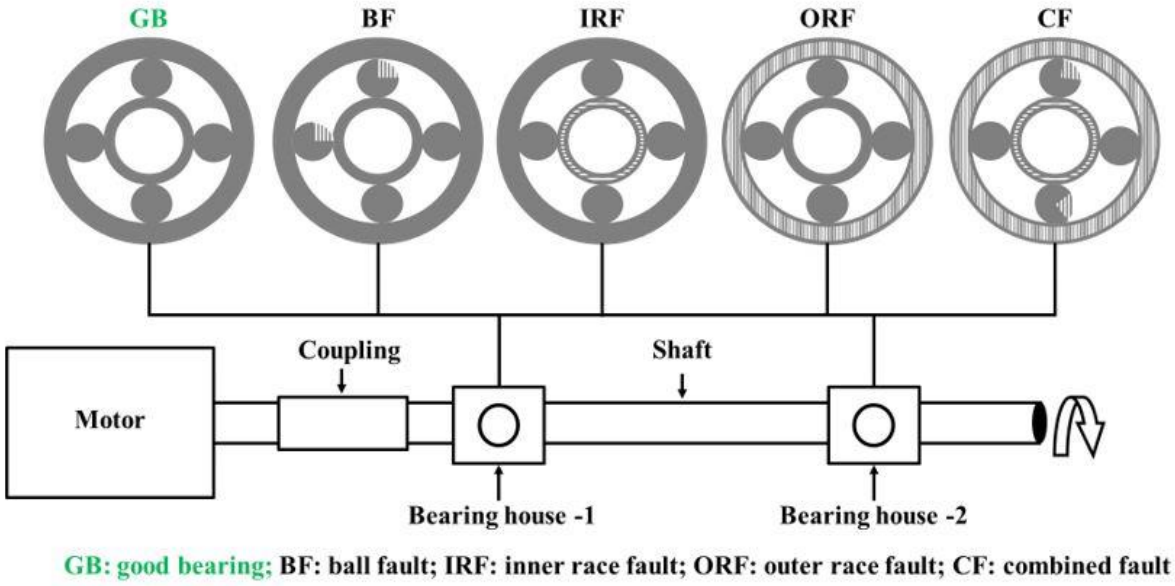

Figure 4.1 Different fault scenarios of a rotary machinery.

4.2 Technical contribution of this work

In this paper, a new multi-channel sensor fusion methodology, named frequency-domain multilinear principal component analysis (FDMPCA), is proposed to integrate multiple channels of vibration and acoustics signals. The technical contribution of this study can be summarized below. The proposed frequency-domain multilinear principal component analysis (FDMPCA) method has the following technical contributions. Firstly, the integration of frequency analysis and MPCA significantly improves the computational efficiency. This is due to the low-dimensional feature extraction from high-dimensional frequency-domain tensor (e.g., reduced by 99.62% in the case study). In addition, the proposed method also outperformed the benchmark method (1-D CNN method) for the accuracy of real-time fault diagnosis. The rest of this paper is organized as follows. Proposed method has been discussed in section 4.3. Section 4.4 demonstrates a case study based on the Machine Fault Simulator®, along with the experimental setup, data collection. Section 4.5

explains the results comparison and discussion. Conclusion and future works are discussed in section 4.6.

4.3 Proposed methodology

In this study, a novel method is proposed for sensor data fusion by a new FDMPCA-based tensor decomposition for low dimensional feature extraction for real-time bearing fault diagnosis. In this section, frequency analysis based on Fast Fourier Transform (FFT) is firstly introduced, and subsequently, the frequency domain tensor structure is constructed. The resulting tensor structure is decomposed using the FDMPCA to extract critical features for fault diagnosis. Finally, the supervised learning method is leveraged for bearing fault diagnosis. The overview of the proposed methodology along with the data visualization at multiple key steps are shown in Figure 4.2.

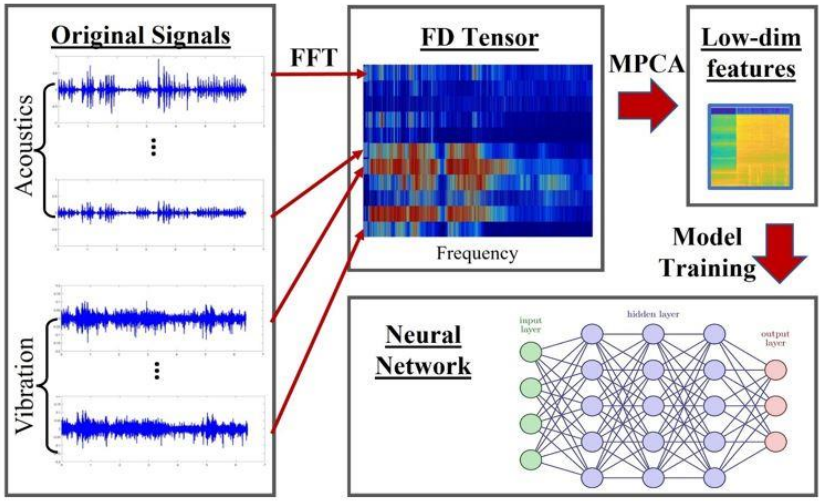

Figure 4.2 Proposed methodology of real-time bearing fault diagnosis of rotary machinery based on sensor data fusion of vibration and acoustics signals.

4.3.1 Time-frequency analysis based on FFT

After collecting the sensor-based signal data the FFT algorithm is applied for converting acoustics and vibration signal from time domain to frequency domain. As a fast-computational approach, the FFT is used for signal data compression [221]. Basically, using FFT based computation, the frequency responses of both vibration and acoustic signals can be generated. Acoustics and vibration time domain signal can be presented as $a_l^1(t), a_l^2(t), a_l^3(t), \dots, a_l^r(t)$ and $v_l^1(t), v_l^2(t), v_l^3(t), \dots, v_l^s(t)$, where r and s represents the number of acoustics and vibration channels and l is the observation index. The generalized FFT equation [221] for converting a time domain vibration or acoustic signal with n points to frequency domain can be expressed in Eq. (4.1).

$$f[k] = \frac{1}{M}\sum_{n=0}^{M-1} x[n]\, e^{\frac{-i2\pi kn}{M}} \tag{4.1}$$

where, $x[n]$ is a digital time domain signal with n time index, which can be any acoustics and vibration signals, i.e., $a_l^1(t), a_l^2(t), a_l^3(t), \dots, a_l^r(t)$ and $v_l^1(t), v_l^2(t), v_l^3(t), \dots, v_l^s(t)$. $f[k]$ is a frequency domain signal with k frequency index, i is an imaginary number and M is the digitally stored number of data points in signal x. Using the Eq. (1), the frequency domain of acoustics and vibration signal can be generated as $fa_l^1(\upsilon), fa_l^2(\upsilon), fa_l^3(\upsilon), \dots, fa_l^r(\upsilon)$ and $fv_l^1(\upsilon), fv_l^2(\upsilon), fv_l^3(\upsilon), \dots, fv_l^s(\upsilon)$, respectively. It is worth noting that in cases the frequency responses of different signals are of different lengths, linear interpolation can be applied to obtain all the frequency responses with unified length.

4.3.2 Frequency-domain tensor construction

The acoustics and vibration signals in the frequency domains of unified length of $fa_l^1(v), fa_l^2(v), fa_l^3(v), \dots, fa_l^r(v)$ and $fv_l^1(v), fv_l^2(v), fv_l^3(v), \dots, fv_l^s(v)$, are combined to construct FD tensor with the dimension of $D_1 \times (r+s)$. The resulting FD tensor, denoted as curved letter $\mathcal{Z}_l$, is represented as below in the Eq. (4.2).

$$\mathcal{Z}_l \in \mathbb{R}^{D_1 \times (r+s)} \tag{4.2}$$

where, D_1 and $(r+s)$ represents the unified frequency domains of different channels and the total number of channels in the multi-sensor fusion, respectively. Figure 4.3 represents FD tensor with corresponding frequency domains of different channels and number of observations.

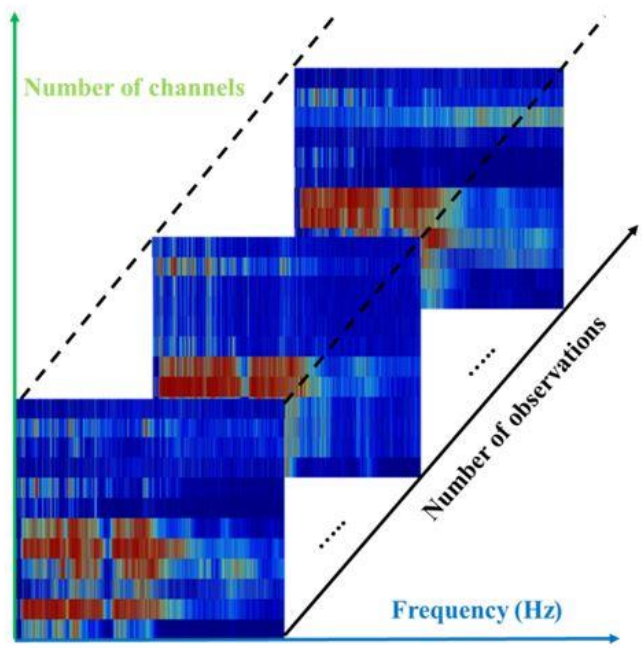

Figure 4.3 FD tensor that comprise of frequency domains, number of channels and observations.

4.3.3 Feature extracting using MPCA

Based on multilinear algebra, the tensor $\mathcal{Z}_l$ can be expressed in Eq. (4.3),

$$\mathcal{Z}_l = \mathcal{G}_l \times_1 \mathbf{U}^{(1)} \times_2 \mathbf{U}^{(2)} \tag{4.3}$$

where $\mathcal{G}_l = \mathcal{Z}_l \times_1 \mathbf{U}^{(1)^T} \times_2 \mathbf{U}^{(2)^T}$, and $\mathbf{U}^{(1)}$ and $\mathbf{U}^{(2)}$ represents the orthogonal projection matrices corresponding to the first and second mode of the FD tensor, as illustrated in Eq. (4.4). $\mathcal{G}_l$ represents the core tensor with reduced dimension $d_1 \times d_1$ ($0 < d_1 < D_1$ and $0 < d_2 < (r + s)$.

$$\mathcal{G}_l = \mathcal{Z}_l \times_1 \mathbf{U}^{(1)^T} \times_2 \mathbf{U}^{(2)^T} \tag{4.4}$$

The objective of MPCA is to find those projection matrices, i.e., $\mathbf{U}^{(1)}$ and $\mathbf{U}^{(2)}$, which maximizes the total tensor scatter in $\mathcal{G}_l$, denoted by $\psi_{\mathcal{G}}$, as illustrated in Eq. (4.5). Figure 4.4 demonstrates the tensor decomposition of the FD tensor based on MPCA analysis. Figure 4.5 illustrates the pseudocode for implementing the MPCA algorithm, which is adapted from [197].

$$\{\mathbf{U}^{(1)}, \mathbf{U}^{(2)}\} = \underset{\mathbf{U}^{(1)},\mathbf{U}^{(2)}}{\operatorname{argmax}} \psi_{\mathcal{G}} \tag{4.5}$$

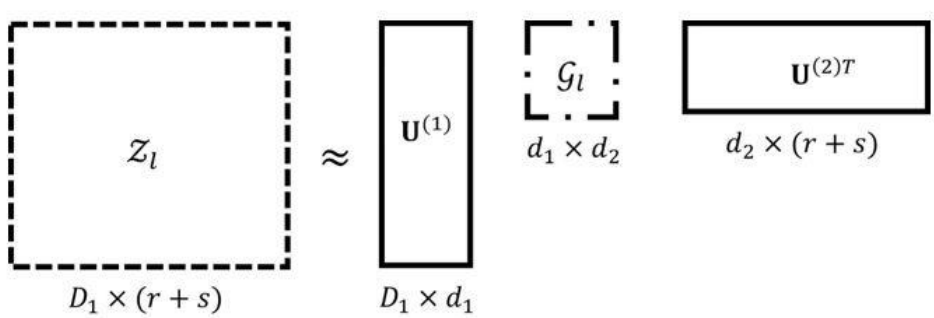

Figure 4.4 FD tensor decomposition based-on MPCA analysis.

Input: A set of vibration and acoustics feature distribution $\{\mathcal{Z}_l \in \mathbb{R}^{D_1 \times (r+s)}, l = 1,2,\dots,L_{tr}\}$, where L_{tr} is training observation number

Output: Low dimensional features $\mathcal{G}_l$

Algorithm:

Step 1 (Element-wise Transferring and Centering):

1.1 Centre training samples as $\{\tilde{\mathcal{Z}}_l = \mathcal{Z}_l - \bar{\mathcal{Z}}, l = 1,2,\dots,L_{tr}\}$, where $\bar{\mathcal{Z}} = \frac{1}{L_{tr}}\sum_{l=1}^{L_{tr}} \mathcal{Z}_l$.

Step 2 (Initialization):

2.1 Calculate the eigen-decomposition of $\mathbf{\Phi}^{(j)*} = \sum_{l=1}^{L_{tr}} \tilde{\mathbf{X}}_{l(j)} \tilde{\mathbf{X}}_{l(j)}^T$ $(j = 1,2)$ and set $\tilde{\mathbf{U}}^{(1)}$ and $\tilde{\mathbf{U}}^{(2)}$ to consist of the eigenvectors corresponding to the most significant d_1, d_2 eigenvalues, respectively. Here $\tilde{\mathbf{X}}_{l(j)}$ represents the unfolded matrix of $\tilde{\mathcal{Z}}_l$ along the j-th mode.

2.2 Calculate $\{\tilde{\mathcal{G}}_l = \tilde{\mathcal{Z}}_l \times_1 \tilde{\mathbf{U}}^{(1)^T} \times_2 \tilde{\mathbf{U}}^{(2)^T}, l = 1,2,\dots,L_{tr}\}$

2.3 Calculate $\psi_{\mathcal{G}_0} = \sum_{l=1}^{L_{tr}} \|\tilde{\mathcal{G}}_l\|_F^2$

Step 3 (Optimization):

For $p = 1{:}\,Q$

Update $\tilde{\mathbf{U}}^{(1)}$: Set the matrix $\tilde{\mathbf{U}}^{(1)}$ to consist of the d_1 eigenvectors of the matrix $\mathbf{\Phi}^{(1)} = \sum_{l=1}^{L_{tr}} \tilde{\mathbf{X}}_{l(1)} \cdot \tilde{\mathbf{U}}^{(1)} \cdot \tilde{\mathbf{U}}^{(1)^T} \cdot \tilde{\mathbf{X}}_{l(1)}^T$, corresponding to the largest d_1 eigenvalues.

Update $\tilde{\mathbf{U}}^{(2)}$: Set the matrix $\tilde{\mathbf{U}}^{(2)}$ to consist of the d_2 eigenvectors of the matrix $\mathbf{\Phi}^{(2)} = \sum_{l=1}^{L_{tr}} \tilde{\mathbf{X}}_{l(2)} \cdot \tilde{\mathbf{U}}^{(2)} \cdot \tilde{\mathbf{U}}^{(2)^T} \cdot \tilde{\mathbf{X}}_{l(2)}^T$, corresponding to the largest d_2 eigenvalues.

Calculate $\{\tilde{\mathcal{G}}_l, l = 1,2,\dots,L_{tr}\}$ and $\psi_{\mathcal{G}_p}$.

If $\psi_{\mathcal{G}_p} - \psi_{\mathcal{G}_{p-1}} < \varepsilon$, break and output projection matrices, $\tilde{\mathbf{U}}^{(1)}$and $\tilde{\mathbf{U}}^{(2)}$

Step 4 (Projection): For training and test data, the low-dimensional features are calculated as

$\{\mathcal{G}_l = (\mathcal{Z}_l - \bar{\mathcal{Z}}) \times_1 \tilde{\mathbf{U}}^{(1)^T} \times_2 \tilde{\mathbf{U}}^{(2)^T}, l = 1,2,\dots,L_{tr}\}$.

Figure 4.5 MPCA projection matrix estimation.

4.3.4 Real time fault detection based on supervised learning

Supervised learning algorithms can be adopted to establish a distinction among different operating conditions of rotary machines based on the extracted features by leveraging a training data set. The Neural Network (NN) models can learn robustly non-linear and complex relationships. A schematic diagram of the Neural Network is illustrated in Figure 4.6, which comprises input, hidden, and output layers. It's worth noting that all different Machine Learning methods can be used for fault detection. The NN classifier can be trained using a training data set with labelling information to obtain the best distinction among different classes, and the

complexity of the model can be determined through cross validation. In neural networks, the hyper-parameter selection, such as the number of hidden layers and learning rate, are significantly important as they directly regulate the trained model's behavior and significantly impact the model's performance [219], [222]. Bayesian optimization can be also used for hyperparameter tuning for the NN models [222].

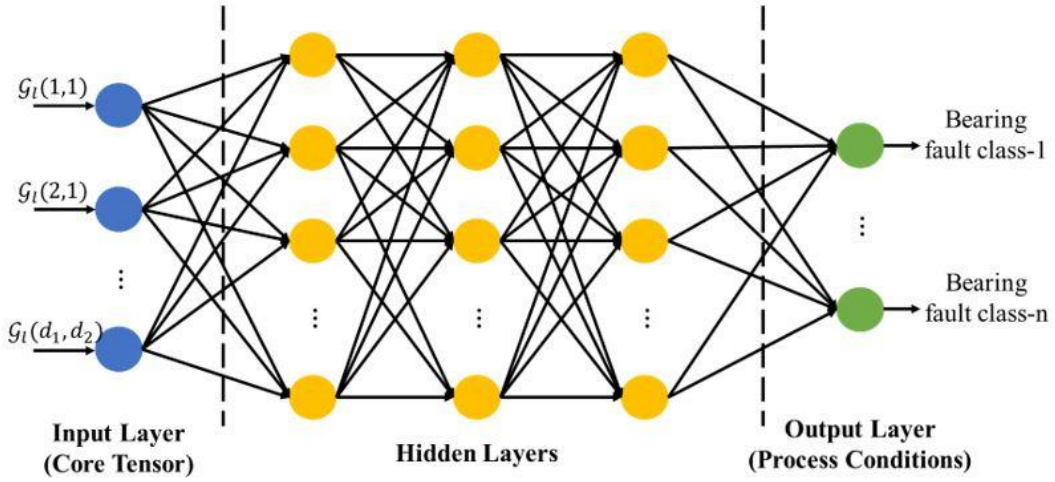

Figure 4.6 Schematic diagram of Neural Network.

4.4 Case study

This section evaluates the performance of proposed methodology using a machine fault simulator (MFS) ®, Manufactured by Spectra Quest Inc. The system is equipped with vibration and acoustics sensors for real-time fault detection and diagnosis.

4.4.1 Experimental setup and data collection

In this research work, vibration and acoustics signals are collected via accelerometers and microphones, respectively. Industrial ICP® 608A11 model single axis accelerometers are used for vibration data acquisition purposes with sensitivity performance 100 mV/g and frequency ranges

of 0.20 to 15 kHz. Adafruit® silicon MEMS microphones SPW 2430 with frequency response of 100 Hz to 10 kHz are used for acoustic signal recording. Figure 4.7 demonstrates sensor allocation on the MFS. A total of six accelerometers are placed on two bearing housings, with three attached to each bearing house, respectively. These six signals were connected to a data acquisition system for data collection, and the sampling rate was 10,240 Hz. Furthermore, six microphones were attached to the inside wall of MFS chamber and connected to another DAQ to capture real-time acoustic emission signals at a sampling frequency of 8,000 Hz. Figure 4.8 demonstrates the real-world MFS setup for data collection. The operating motor speed was 30 Hz. Table 4.1 demonstrates the experimental design for five different operating conditions and their corresponding sample sizes.

Table 4.1 Design of experiments for acoustics and vibration signals collection.

Bearing House -1	**Bearing House -2**	**Class Label**	**Number of observations**
Good	Good	1	90
Good	Ball fault	2	27
Ball fault	Good	2	27
Good	Inner race fault	3	27
Inner race fault	Good	3	27
Good	Outer race fault	4	27
Outer race fault	Good	4	27
Good	Combined fault	5	27
Combined fault	Good	5	27
	Total		**306**

The multi-channel sensor signals were collected after the motor reached the steady state operation conditions, and each run took 2.13 seconds of sensing data.

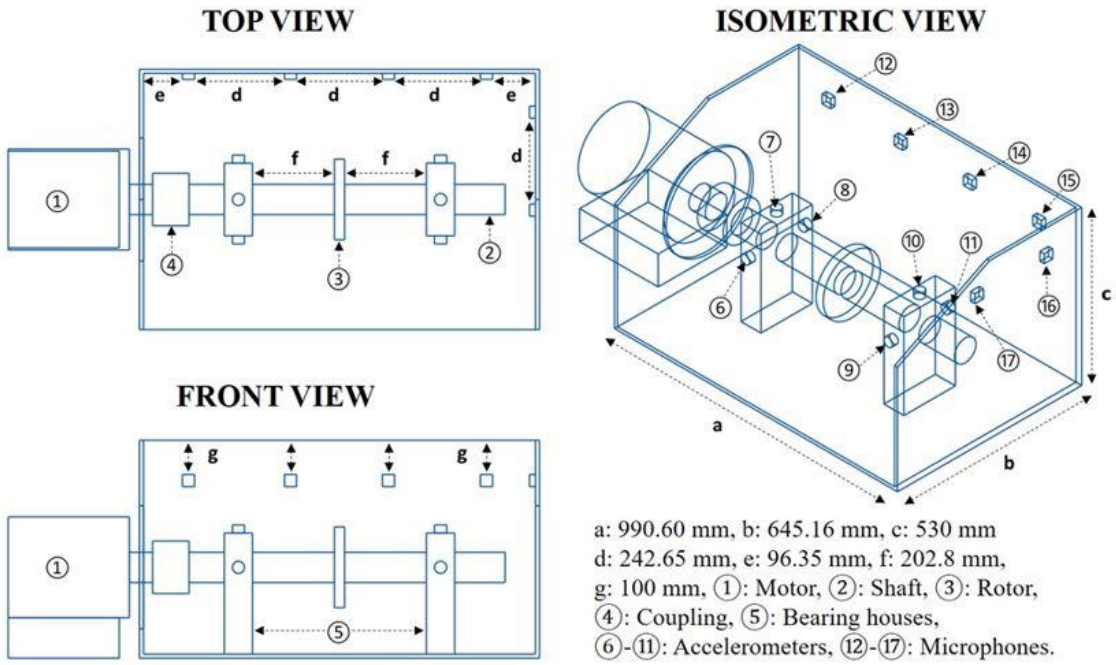

Figure 4.7 Multi-channel sensor allocation in the Machine Fault Simulator.

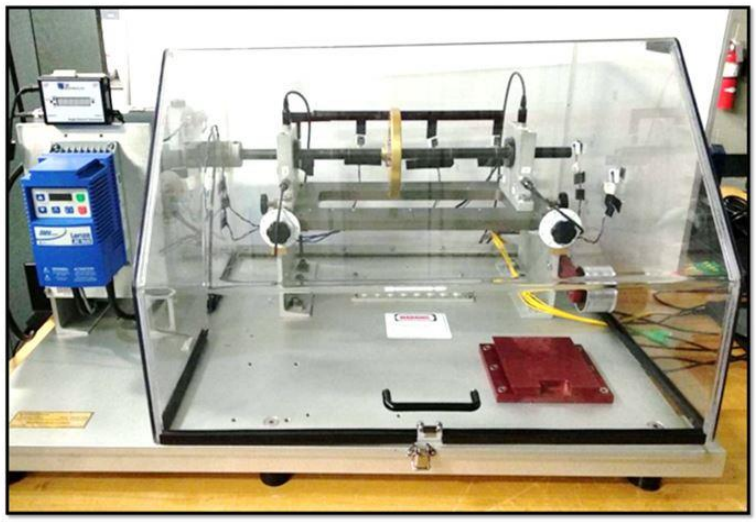

Figure 4.8 MFS setup for data collection with acoustics and acceleration sensors.

4.4.2 Benchmark method

Basically, the application of CNN can yield competitive performance evaluation in fault diagnosis of RM [219]. In this study, Chen et al.'s [22]1D-CNN method was selected as the benchmark method to compare with the proposed method. Chen et al.'s [22] paper demonstrated the advantages using 1D-CNN in RM fault diagnosis, including (a) a larger number of mixed faults can be classified, (b) the method shows the ability to recognize and classify unknown fault classes as well as robustness to noise perturbation. In the benchmark method, the 1D-CNN technique was adopted for mixed faults diagnosis of RM. Even though only vibration signals were used in Chen et al.'s [22] paper, all the sensing signals, including six channels of acoustics and six channels of vibration signals, were utilized to develop a 1D-CNN model for a fair comparison. Moreover, for hyperparameter tuning the automatic search method of Bayesian optimization can find global optima of 1-D CNN based on a given dataset. During Bayesian optimization of hyper-parameters for 1-D CNN, the range of learning rate and L-2 regularization were set as $[0.0001, 0.1]$ and $[10^{-10}, 10^{-2}]$, respectively. 5-fold cross-validation was used for hyper-parameter tuning, and the number of maximum objective evaluations was set as 10. The Bayesian optimization took in a total of 39 hours and 31 minutes using the Intel (R) Core (TM) i7-7700 CPU @ 3.60 GHz with NVIDIA GeForce GT 730. Table 4.2 shows the input factors of 1D-CNN for Bayesian optimization.

Table 4.2 1-D CNN architecture for training networks.

Input factors in 1-D CNN	Parameters
Filter size	3 x 1
Number of filters	32 for 1st convolutional layer 64 for 2nd convolutional layer
Optimizer	Adaptive Momentum Estimation (ADAM)
Batch size	20
Number of epochs	15
Validation frequency	5
Drop rate factor	0.50
Learn rate drop period	15

4.4.3 Evaluation criteria and procedure

For a fair comparison between the proposed and benchmark method, the evaluation procedure is described as below. In the proposed FDMPCA method, out of the 306 observations, 12% of bearing class label- 1, which is equivalent to 36 observations are used as FDMPCA projection matrix. Subsequently, all the remaining data were mapped to the low-dimensional space, among which 68% of all the samples were used in training the neural networks models and the rest 20% were used as testing data. Regarding the benchmark method, 80% of the samples were used in 1-D CNN for training and validation purposes, and the remaining 20% were used for testing. Figure 4.9 represents the overall view of observations data splitting for the proposed and benchmark method. It is worth mentioning that the random seeds used for data splitting in the proposed and benchmark methods were kept the same to make each iteration directly comparable. Ten iterations were implemented by repeating the testing procedure above.

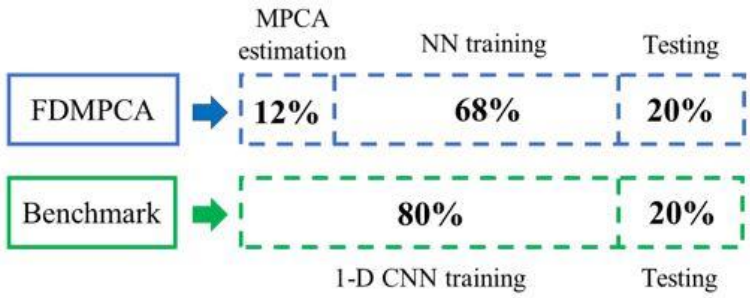

Figure 4.9 Observation data splitting for the proposed FDMPCA and benchmark method.

The performance matrices include precision, recall, and overall accuracy are used for performance evaluation of both proposed and benchmark methods. The following Eq. (4.6), (4.7) and (4.8) represent precision, recall, and accuracy, respectively. In those equations, True positive (TP) denotes bearing fault classes that are predicted accurately corresponding to actual classes. True negative (TN) demonstrates bearing fault classes which are predicted inaccurately corresponding to respective classes. Additionally, false positive (FN) represents inaccurate prediction of bearing fault classes and false positive (FP) denotes inaccurate prediction of bearing fault classes, which are accurate class but predicted to inaccurate classes.

$$\text{Precision} = \frac{\text{TP}}{\text{TP} + \text{FP}} \tag{4.6}$$

$$\text{Recall} = \frac{\text{TP}}{\text{TP} + \text{FN}} \tag{4.7}$$

$$\text{Accuracy} = \frac{\text{TP} + \text{TN}}{\text{TP} + \text{TN} + \text{FN} + \text{FP}} \tag{4.8}$$

4.4.4 Proposed FDMPCA-based feature extraction

Using Eq. (4.1), the acoustics and vibration signals were converted into the frequency domain from the time domain. Subsequently, six channels of acoustics and six channels of vibration signals with unified length of frequency domain dimensions were fused together to construct the FD tensors. Figure 4.10 demonstrates FD tensor that has been constructed from acoustics and vibration time-domain raw signals. The constructed FD tensor's dimension is $8{,}534 \times 12$, and then the MPCA projection matrices were estimated to extract low dimensional features. The resulting feature dimension varies for each iteration (summarized in Table 4.3), with the mean value as 386.3 and the standard deviation value as 9.3. The proposed method reduces the dimension of the FD tensors by 99.62%, and the original data by 99.83%.

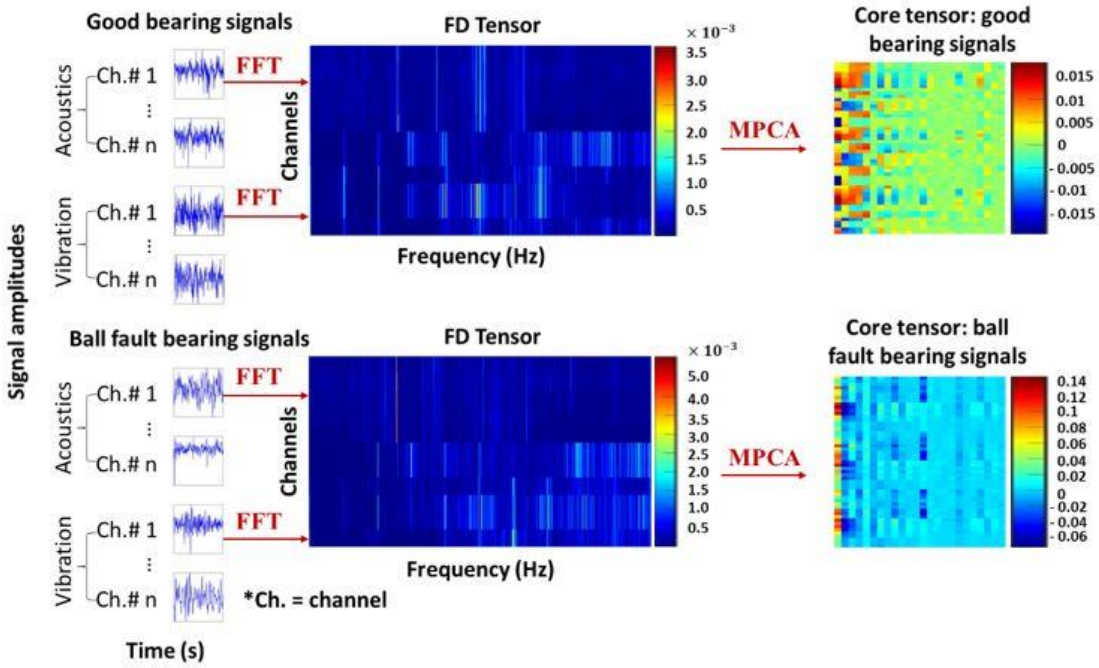

Figure 4.10 Frequency-domain based tensor from original time-domain signals.

Table 4.3 Number of low-dimensional features extracted from 10 iterations.

Run #	Dimension of extracted features
1	385
2	385
3	409
4	389
5	370
6	389
7	381
8	385
9	381
10	389

4.4.5 Neural Network training

When training the NN classifier, the Bayesian optimization technique was adopted for hyperparameter tuning, where the learning rate and the number of nodes per layer were tuned. Basically, the algorithm reaches to the minimum loss function value that yields the best tuned hyper-parameters. During hyperparameter tuning the range for learning rate and number of nodes per layer set as $[0.001, 0.1]$ and $[1, 40]$, respectively. Table 4.4 shows neural network input factors including learning rate, number of nodes per layer, and optimizer used for network training. It is worth noting that 5-fold cross validation was used for parameter tuning and the number of maximum objective evaluation was set as 20 for tuning NN. Finally, the tuned NN model was applied to the independent testing samples for performance evaluation. Table 4.5 shows the Bayesian optimized hyper-parameters for neural networks in all the 10 iterations.

Table 4.4 Neural network input factors.

Neural Network input factors	Parameters
Learning rate	$[0.001 - 0.1]$
Number of nodes per layer	$[1 - 40]$
Optimizer	Gradient Descent Backpropagation

Table 4.5 Bayesian optimized hyper-parameters for NN.

Iteration	Learning rate	No. of nodes per layer
1	0.099992	17
2	0.058304	40
3	0.055059	40
4	0.081894	20
5	0.039273	25
6	0.098252	25
7	0.099589	10
8	0.099996	15
9	0.061274	28
10	0.069321	40

4.5 Results comparison and discussion

Table 4.6 shows the performance metrics of proposed and benchmark methods for each individual category. All the precision and recall metrics were calculated based on the ten iterations. Overall test accuracy for the proposed method and benchmark methods found 99.00% and 97.40%, respectively. Based on the performance metrics comparison, it is observed that the proposed methodology demonstrates universally better performance than the benchmark method for all the different fault scenario diagnosis. In addition, the proposed method demonstrates lower standard deviation values in the performance metrics over the 10 iterations, which shows that its performance is more robust to random data splitting in the evaluation. Moreover, the

computational complexity of the proposed method is significantly lower than the benchmark method. More specifically, the total computation time, including both FDMPCA-based feature extraction time and the NN testing time, is significantly shorter than the testing time of the benchmark method.

Table 4.6 Results summary of the proposed and benchmark methods.

Class label #	**Proposed method**			**Benchmark method**	
	Metric	Avg.	Std.	Avg.	Std.
Good bearing	Precision	0.9909	0.02875	0.9652	0.05979
	Recall	1.0000	0.00000	0.9800	0.06325
Ball fault	Precision	0.9727	0.04391	0.9733	0.05838
	Recall	0.9800	0.04216	0.9500	0.09718
Inner race	Precision	1.0000	0.00000	1.0000	0.00000
	Recall	1.0000	0.00000	1.0000	0.00000
Outer race	Precision	1.0000	0.00000	0.9742	0.05717
	Recall	1.0000	0.00000	0.9700	0.04830
Combined faults	Precision	0.9909	0.02875	0.9742	0.05717
	Recall	0.9700	0.04830	0.9700	0.06749
Total accuracy		**99.00%**		**97.40%**	

As illustrated in Figure 4.11, the computational time of the proposed method is 68.1% lower than the benchmark method. Therefore, the proposed model is more appropriate for real-time detection and fault diagnosis. This is mainly due to FDMPCA's capacity in dimension reduction, where the low-dimensional features lead to simpler Machine Learning models for classification.

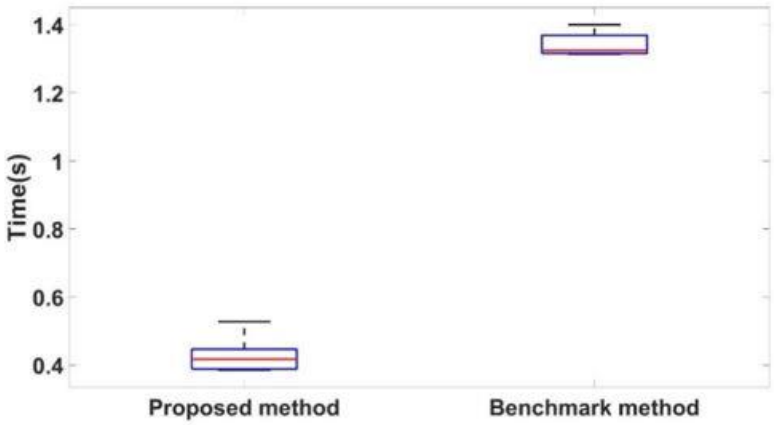

Figure 4.11 Test time comparison between proposed method and benchmark method.

4.6 Conclusion and future work

Real-time fault detection and diagnosis can be challenging for high dimensional data with relatively a small sample size. In contrast, collecting large amounts of data with all the machine faults can be challenging and costly. In this paper, a novel multi-channel sensor fusion methodology is proposed for real-time bearing fault diagnosis to integrate multiple sensing signals with diverse sampling rates for real-time bearing fault detection and diagnosis of a rotary machine with limited training data availability. Specifically, the frequency-domain multilinear principal component analysis (FDMPCA) leverages frequency analysis and tensor decomposition for feature exaction and dimension reduction, which significantly simplifies the Machine Learning models trained for fault diagnosis. In the case study, the machine fault simulator was used to validate the effectiveness of the proposed method for fault detection and diagnosis for RM. The proposed method demonstrated better performance in nearly all the performance metrics for bearing fault diagnosis than the CNN-based benchmark method. Moreover, FDMPCA-based low dimensional feature extraction methodology demonstrated significantly better computational efficiency. Therefore, in cases of real-life engineering applications, the proposed FDMPCA

method can be adopted to achieve satisfactory performance as a multi-sensor fusion method for real time condition monitoring and fault diagnosis of RM with limited training data availability.

This study can be potentially extended in the following directions. Firstly, the extension of this work can be conducted by incorporating scenarios when both bearings have faults in the fault diagnosis. Secondly, in real-world applications, especially in the context of Industry 4.0 perspective, it is not uncommon that some (or even all) sensor signals may be not available from time to time due to the sensor malfunction, or connection issue. This will lead to missing data in the collected multi-channel data. As a result, multi-channel sensor fusion can be challenging for rolling element fault identification and diagnosis when there is significant missing data. Furthermore, in real-world machine fault diagnosis problems, it is not practical to assume all the possible fault scenarios have been included in the historical data. Therefore, how to leverage existing data for new fault identification is another open research question, and some data augmentation methods, such as generative adversarial network (GAN) models can be leveraged for this problem.

CHAPTER V

MISSING SIGNAL IMPUTATION FOR MULTI-CHANNEL SENSING SIGNALS ON ROTARY MACHINERY BY TENSOR FACTORIZATION

5.1 Motivation and challenges

In cyber-physical systems, a manufacturing plant can be operated and monitored simultaneously at the physical plants with the help of remotely controlled sensors that can collect real-time data for process monitoring and decision-making [1], [16], [223]. The emerging trend of multi-channel sensor fusion is ubiquitous. Industry 4.0 perspective, heterogeneous sensor fusion can be integrated real-time for condition monitoring of machinery [224]. Different sensors, including accelerometers, infrared imaging sensors, microphones, power loggers, and thermocouples, are widely used for collecting real-time sensing signals [119], [121]. Among those sensing technologies, microphones and accelerometers are extensively used for acoustic and vibration signals. Numerous studies showed that combining acoustics and vibration signals is more effective than the individual signal analysis approach [215], [225]. Advanced sensing technologies pose some inherent challenges in real-time data-driven decision-making in various advanced manufacturing industries-high dimensional data and a substantial amount of missing signals occurrence [223], which is demonstrated in Figure 5.1. However, signal missing may prevail due to various reasons, including sensor sensitivity malfunction, sensor hardware malfunction, and transmission disruptions[165]. The effect of signal missing data may end up with either continuous or random missing data [165]–[168]. Moreover, in the worst-case scenarios, for example, during

a blackout situation, a substantial portion of continuous missing data may also occur [55], [56], [226], [227]

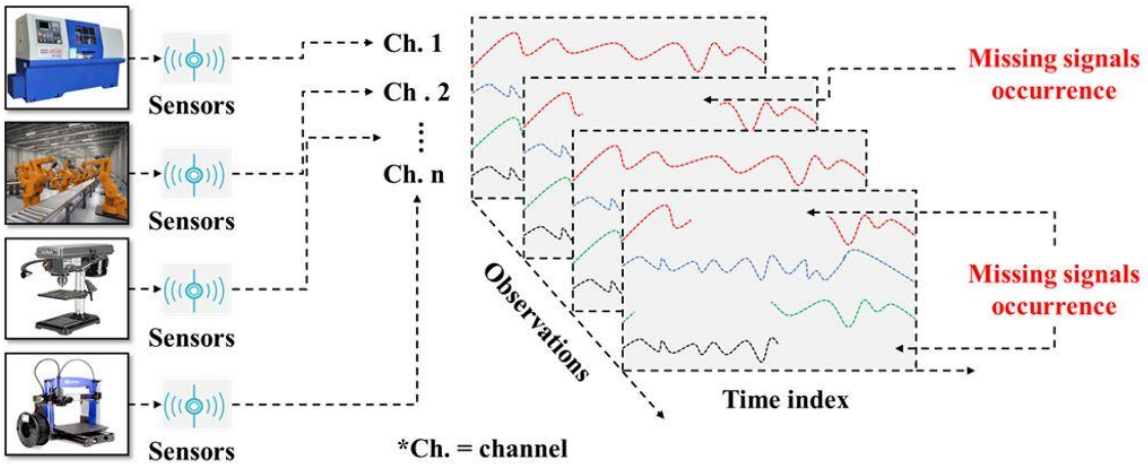

Figure 5.1 Implication of heterogeneous sensor fusion in cybermanufacturing system.

Ultimately, this leads to a substantial volume of missing data occurrence. While imputation of missing entries can also be challenging, and that can also predominantly affect the performance of imputation. However, the multidimensional data structure, which is defined as a tensor, provides an effective way to handle high-volume of data. Tensor completion task with substantially missing data volume effectively imputes missing entries when sensor signal missing occurrence exists. Additionally, tensor factorization enables to capture of multi-linear interaction (channels \times signals) among latent factors of sensor signals and imputes missing entries based on observed signals [20], [227].

Seeking state-of-the-art, a significant number of studies have been involved in imputing missing entries by adopting tensor completion. This study has incorporated the CANDECOMP/PARAFAC (CP) tensor factorizations method that captures multi-linear structures

and incomplete tensor completion tasks. This study adopted a tensorial missing signal imputation by a fully Bayesian CANDECOMP/PARAFAC (FBCP) factorization method with low-rank determination [20]. The FBCP method provides several competitive advantages in dealing with missing signal imputation along with incomplete tensor completion. For instance, a. FBCP method can automatically determine CP rank, b. efficiently avoid overfitting, c. performs well in imputing missing entries with incomplete tensors.

5.2 Technical contribution of this proposed method

This proposed method was conducted on a machinery faults simulator (MFS) based on different bearing fault scenarios by incorporating acoustics and vibration signals. A varying percentage of continuous missing signal scenarios is generated among an equal number of acoustics and vibration channels with a unified length of signals. And then constructed time-domain tensor. Missing signal imputation in the time-domain tensor was adopted by a FBCP factorization method [20]. Figure 5.2 demonstrates continuous missing signals among different channels. It is worth noting that a continuous missing entry is introduced at a random location with varying missing percent based on a given length of signals. The FBCP method enables to capture of multi-linear interaction (channels × signals) among latent factors of sensor signals. The FBCP method performs missing entries imputation along with incomplete tensor completion with low-rank determination. Overall, this proposed method performed well imputing a varying length of continuous missing entries of multi-channel sensor signals from diverse bearing fault conditions.

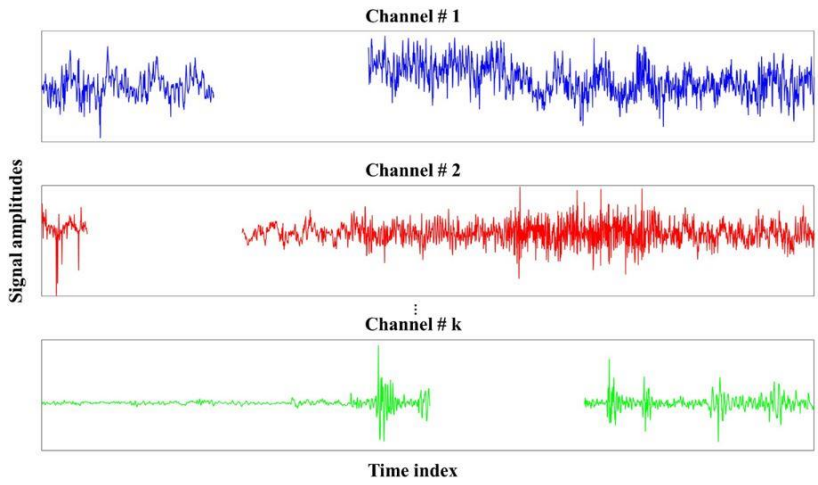

Figure 5.2 Continuous missing signals among different channels.

5.3 Methodology

In this section, the proposed method is presented to impute missing entries in the time-domain signals generated from acoustic and vibration sensors. A varying percentage of continuous missing signal scenarios is generated at a specific channel with a unified length of signals at random location of signals. And then constructed time-domain tensors with all channels at a time, which is defined as incomplete time-domain tensors. Missing signal imputation in incomplete time-domain tensor is adopted by a FBCP factorization method [20] and computed an estimated tensor. Thus, the performance evaluation of FBCP method is calculated based on relative standard error (RSE) of estimated and actual tensors. The overview of the proposed method is depicted in Figure 5.3, that illustrates continuous missing signal scenarios at channel 1 and constructed incomplete time-domain tensors with all channels.

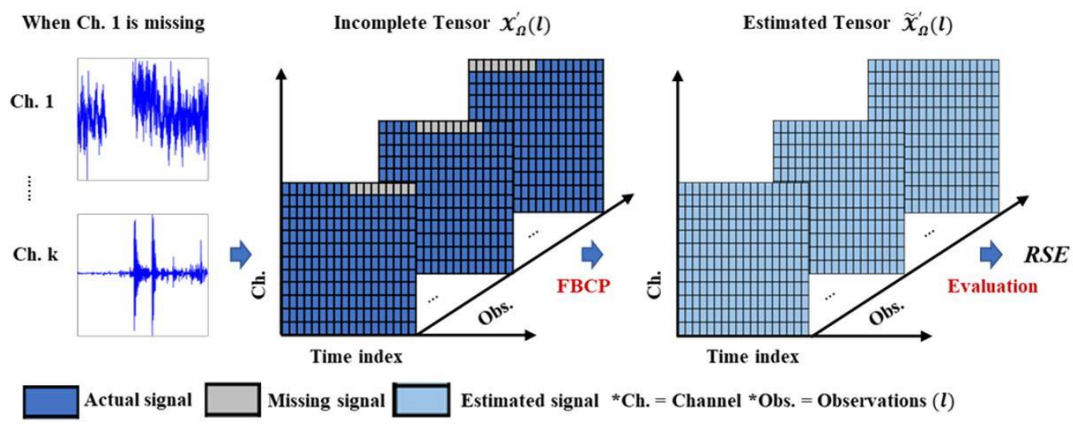

Figure 5.3 The proposed framework for multi-channel missing signal imputation.

5.3.1 Tensor formation of the time-domain signal

Acoustics and vibration time-domain channel-wise signals are combined and expressed as $s_l^1(t), s_l^2(t), s_l^3(t), \dots, s_l^k(t)$, where k represents the total number of channels and l denotes the observation index as $l = 1, 2, 3, \dots, m$. The combined time-domain signals with l observations are constructed as a time-domain tensor with the dimension of $D \times k$. The resulting time-domain tensor contains the actual acoustics and vibration signals, which is denoted as $\mathcal{X}_{\Omega}(l) \in \mathbb{R}^{D \times k}$, where D represents the length of the unified time-domain signals, where channel-wise continuous missing signals can occur at random location. Furthermore, Ω denotes the set of indices in $\mathcal{X}_{\Omega}(l)$, and $(i_1, i_2) \in \Omega$ where $i_n = 1,2,\dots,I_n$, $I_1 = D$ and $I_2 = k$. With continuous missing entries in the signal, the incomplete time-domain tensor can be expressed as $\mathcal{X}'_{\Omega}(l) \in \mathbb{R}^{D \times k}$ (Figure 5.3).

5.3.2 Bayesian-CP based tensor completion

The FBCP algorithm can effectively correlate the latent multi-linear factors based on the observed data with a low-rank determination and estimates the predictive distributions among missing entries. In this section, for simplicity, the sample index l of $\mathcal{X}_{\Omega}(l)$ is omitted, since the tensor completion is implemented on each individual sample separately. Let $\mathcal{X}'_{\Omega} \in \mathbb{R}^{D \times k}$ as a 2nd-

order tensor of dimension $D \times k$ with missing entries. The entries of $\mathcal{X}'_{\Omega} \in \mathbb{R}^{D\times k}$ can be denoted by $\mathcal{X}'_{i_1,i_2}$,. The underlying idea of applying Bayesian-CP decomposition is to approximate the $\mathcal{X}'_l$, by generating the low-rank structure as shown in the Eq. (5.1) [228], $\widetilde{\mathcal{X}}'_{\Omega}$ is the estimated tensor, where the operator o denotes the outer product of vectors, and $[\![...]\!]$ is termed as the Kruskal operator.

$$\widetilde{\mathcal{X}}'_{\Omega} = \sum_{r=1}^{R} \mathbf{x}_r^{(1)} \text{ o } \mathbf{x}_r^{(2)} = [\![\mathbf{X}^{(1)}, \mathbf{X}^{(2)}]\!] \tag{5.1}$$

The CP factorization can be calculated as a sum of R rank-one tensors, where the lowest integer R is determined as the CP rank [229]. $\{\mathbf{X}^{(n)}\}_{n=1}^{2}$ contains the set of n-th decomposed factor matrices, and $\mathbf{X}^{(n)} \in \mathbb{R}^{(D\times k)\times R}$ can be denoted as row-wise or column-wise vectors$\mathbf{X}^{(n)} = [\mathbf{x}_1^{(n)}, \ldots \mathbf{x}_{i_n}^{(n)}, \ldots, \mathbf{x}_{I_n}^{(n)}]^T = [\mathbf{x}_{.1}^{(n)}, \ldots \mathbf{x}_{.r}^{(n)}, \ldots, \mathbf{x}_{.R}^{(n)}]$. The calculation of $\text{Rank}_{CP}(\mathcal{X}'_{\Omega}) = R$ is computationally challenging and costly. The Bayesian inference process can reach automatic low-rank approximation based on tensor factorization to avoid the overfitting problem. The CP generative missing entries assumption is based on observed entries of $\mathcal{X}'_l$ and the factorized tensor elements of $p(\mathcal{X}'_{\Omega}|\mathbf{X}^{(n)})$. Now, in order to enable automated rank determination, a sparsity-inducing prior is provided across the hyperparameters, since the smallest R is more desirable in low rank approximation. Specifically, the prior distribution over the latent factor can be determined by $\boldsymbol{\lambda} = [\lambda_1, \ldots \ldots, \lambda_R]$, where λ_r control r-th components in $\mathbf{X}^{(n)}$ that is expressed in the Eq.(5.2), where $\boldsymbol{\Lambda} = \text{diag}(\boldsymbol{\lambda})$ represents the inverse covariance matrix, also known as the precision matrix, that is shared from the latent factor matrix in all modes.

$$p(\mathbf{X}^{(n)}|\boldsymbol{\lambda}) = \prod_{i_n=1}^{I_n} \mathcal{N}\left(\mathbf{x}_r^{(n)} \middle| 0, \boldsymbol{\Lambda}^{-1}\right), n = 1,2 \tag{5.2}$$

The hyperprior over $p(\boldsymbol{\lambda})$ is a factorized dimension and characterized using a Gamma distribution. The latent variables and hyperparameters are collectively denoted in Eq. (5.3). The Bayesian computation of the full posterior distribution of all variables is demonstrated in the Eq. (5.4). Based on the posterior distribution of all variables in Θ, the predictive distribution of missing entries is estimated by the Eq. (5.5), where $\mathcal{X}'_{\backslash\Omega}$ denotes predictive missing entries.

$$\Theta = \{\mathbf{X}^{(1)}, \mathbf{X}^{(2)}, \boldsymbol{\lambda}\} \tag{5.3}$$

$$p(\Theta|\mathcal{X}'_{\Omega}) = \frac{p(\Theta, \mathcal{X}'_{\Omega})}{\int p(\Theta, \mathcal{X}'_{\Omega}) d\Theta} \tag{5.4}$$

$$p\left(\mathcal{X}'_{\backslash\Omega}|\mathcal{X}'_{\Omega}\right) = \int p(\mathcal{X}'_{\backslash\Omega}|\Theta) p(\Theta, \mathcal{X}'_{\Omega}) d\Theta \tag{5.5}$$

The exact Bayesian inference in Eq. (5.4) and Eq. (5.5) integrate over all latent variables and hyperparameters, which is analytically intractable. Therefore, a deterministic approximate inference under variational Bayesian (VB) framework is developed to learn the probabilistic CP factorization model [20]. Basically, a distribution $q(\Theta)$ based on the Eq. (5.4) and Eq. (5.5), is incorporated to approximate true posterior distribution $p(\Theta|\mathcal{X}'_{l})$ by minimizing Kullback–Leibler (KL) divergence, which is denoted in the Eq. (5.6). The lower bound of Eq. (5.6) is solved by Eq. (5.7) and the maximum lower bound can be determined when KL divergence vanishes assuming $q(\Theta) = p(\Theta|\mathcal{X}'_{\Omega})$.

$$\mathrm{KL}(q(\Theta)||p(\Theta|\mathcal{X}'_{\Omega})) \tag{5.6}$$

$$\mathcal{L}(q) = \int q(\Theta) \ln\left\{\frac{p(\mathcal{X}'_{\Omega}, \Theta)}{q(\Theta)}\right\} d\Theta \tag{5.7}$$

Basically, for model learning via Bayesian inference, Eq. (5.6) is further leveraged to obtain the posterior distribution of the factor matrices, hyperparameters and lower bound of the model evidence. Moreover, during Bayesian inference-based model learning, tensor rank is determined automatically and implicitly updating $\boldsymbol{\lambda}$ in each iteration [20]. Specifically, the **Algorithm 1** adopted from [20], which is leveraged in the Figure 5.4. This algorithm can effectively correlate the latent multi-linear factors leveraging Bayesian inference based on the observed data with a low-rank determination and also estimates the predictive distributions among missing entries. To avoid Bayesian inference to local minima, the initial points of the hyperparameter set are to a fixed value. After completion of the missing entries, the evaluation of missing data imputation can be quantified considering actual time-domain tensor $\mathcal{X}_{\Omega}(l)$ and estimated tensor $\widetilde{\mathcal{X}}'_{\Omega}(l)$, where the evaluation metric can be defined as relative standard error (RSE) in the Eq. (5.8). Based on the **Algorithm 1**, the tensor rank can be determined automatically and in practice R is set manually for computational purpose. In this entire process $\boldsymbol{\lambda}$ updates in each iteration that results in a new prior over $\{\mathbf{X}^{(n)}\}$ and then $\{\mathbf{X}^{(n)}\}$ updates by using the new prior in the subsequent iteration.

$$RSE_l = \frac{\left\|\widetilde{\mathcal{X}}'_{\Omega}(l) - \mathcal{X}_{\Omega}(l)\right\|_F}{\|\mathcal{X}_{\Omega}(l)\|_F} \tag{5.8}$$

Algorithm 1: Fully Bayesian CP Factorization for tensor completion.

Input: A set of acoustics and vibration signals of missing entries with incomplete tensor $\{\mathcal{X}'_{\Omega}(l) \in \mathbb{R}^{D\times k}, l = 1,2,\ldots,m\}$, where m is total number of observations.
Initialization: Initialization of hyperparameters Θ set to fixed.
Output: Estimated tensor $\widetilde{\mathcal{X}}'_{\Omega}(l)$
Algorithm:
  Step 1 (Estimated tensor calculation):
  Repeat
    For $l = 1:m$
      Calculate estimated tensor $\widetilde{\mathcal{X}}'_{\Omega}(l)$ leveraging Eq. (5.1)
    end
    Reduce rank R by eliminating components of $\{\mathbf{X}^{(n)}\}$
    Evaluate the lower bound using the Eq. (5.7)
  until maximum number of iterations

  Step 2 (evaluation of missing data imputation)
Relative standard error calculation from the Eq. (5.8)

Figure 5.4 Fully Bayesian CP factorization algorithm [20].

5.4 Case study

The evaluation study was conducted on a testbed using a machinery faults simulator (MFS) manufactured by Spectra Quest Inc., which is illustrated in Figure 5.5 [24] and equipped with multiple vibrations (accelerometers) and acoustics (microphones) sensors for real-time sensor signal acquisition purpose. Figure 5.6 demonstrates accelerometers and microphone allocation in the MFS [24]. Sensor missing signals are generated as planned continuous missing based on the concept of a blackout situation. Equal channels of acoustics and vibration signals are unified, forming tensorial arrays, and a certain percentage of continuous missing signal scenarios is generated among different channels. It is worth noting that continuous missing entries is introduced at a random location with a varying missing percent based on a given length of signals, such as 1%, 3%, 5%, 10%, and 20% missing. Missing entries are imputed along with incomplete tensor completion by the FBCP method, which is illustrated in section 5.4.1. Finally, the

performance of the estimated tensor $\widetilde{\mathcal{X}}'_{\Omega}(l)$ with missing completion was evaluated comparing with the actual tensor $\mathcal{X}_{\Omega}(l)$.

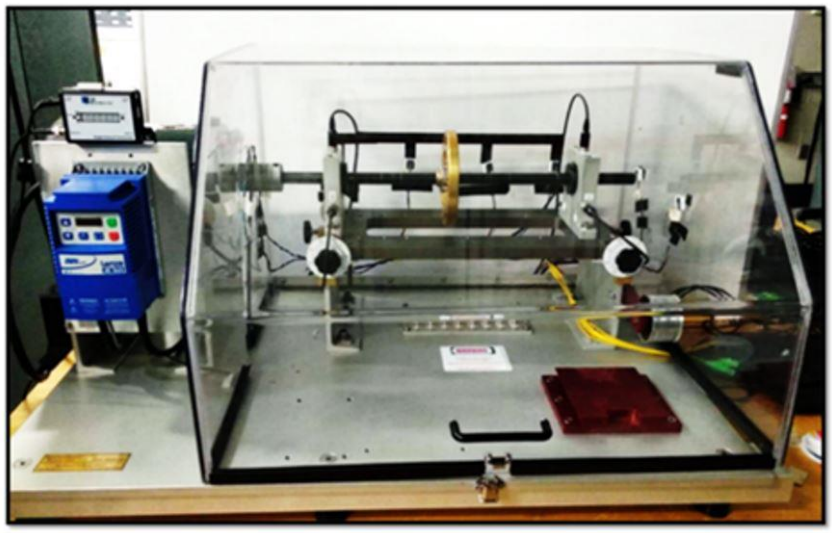

Figure 5.5 The MFS setup for data collection with acoustics and vibration sensors.

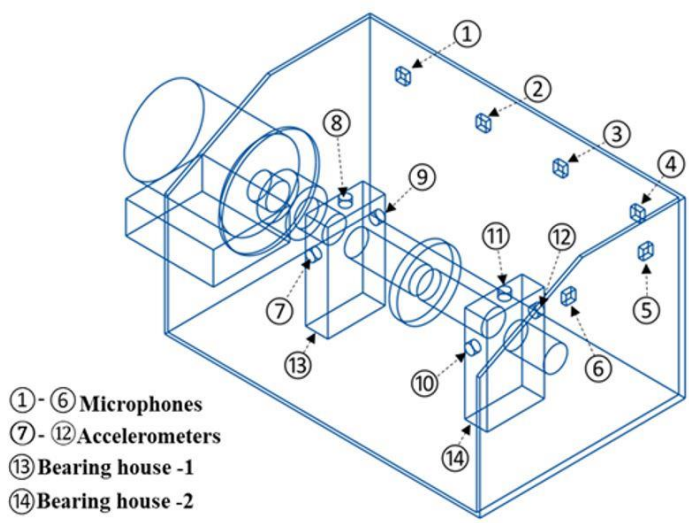

Figure 5.6 Multi-channel sensor allocation in the MFS.

5.4.1 Experimental setup and data collection

In this study, acoustics and vibration signals were compiled by microphones and accelerometers, respectively. Adafruit® silicon MEMS microphones (SPW 2430 model) were incorporated for acoustic signal collection. Single-axis accelerometers (Industrial ICP® 608A11) were used for vibration signal acquisition. Sensitivity performance of accelerometer is 100 mV/g with the frequency ranges of 0.20 to 15 kHz. Six accelerometers were attached on the two bearing housings, where three accelerometers placed on each bearing house, respectively. These six accelerometers were connected to a data acquisition system for data collection with the sampling rate of 10,240 Hz. Also, six microphones were also embedded to the inside wall of the MFS chamber and connected to another data acquisition system to capture real-time acoustic emission signals at the sampling frequency of 8,000 Hz. The working motor speed was 30 Hz. Table 5.1 demonstrates the experimental design for five different bearing fault operating conditions and their corresponding observation numbers. The multi-channel sensor signals were collected after the motor reached the steady state operation conditions.

Table 5.1 Operation conditions performed in data collection.

Bearing house - 1	**Bearing house - 2**	**Class label**	**Number of observations**
Good	Good	1	12
Good	Ball fault	2	6
Ball fault	Good	2	6
Good	Inner race fault	3	6
Inner race fault	Good	3	6
Good	Outer race fault	4	6
Outer race fault	Good	4	6
Good	Combined fault	5	6
Combined fault	Good	5	6
	Total		**60**

5.4.2 Missing data imputation and performance evaluation

In this study, planned missing signal is generated in time-domain tensor with 1%, 3%, 5%, 10%, and 20% percentage of continuous missing among different channels by considering each bearing fault conditions. Missing entries with time-domain tensor size is $12 \times 500 \times 12$, where 12, 500, and 12 represent the total number of channels, signal length, and number of observations for each bearing fault conditions, respectively. Continuous missing is calculated based on the length of signals, where 10% continuous missing equivalent to 50 lengths of continuous missing, which is generated among four different channels at different location randomly. The similar approach is also applicable when 20% missing equivalent to 100 lengths of continuous missing. In the given incomplete tensor size of $12 \times 500 \times 12$ is computed to estimated tensor using each observation starting from 1 to 12. Table 5.2 shows tuning parameters for FBCP-based tensor completion work. While each observation is iterated to 1 to 150 based on performance loss objective value of tolerance limit, which is set as 10^{-12}. In this incomplete-tensor completion, CP rank $R = 250$ is used. The performance evaluation of incomplete-tensor completion (estimated tensor), which is denoted by $\widetilde{\mathcal{X}}'_{\Omega}(l)$ is compared with the actual tensor $\mathcal{X}_{\Omega}(l)$. RSE is computed by the Eq. (5.8). It is worth noting that, tensor completion work is computationally faster when the tensor size is substantially small. To evaluate the effectiveness of the FBCP method, CP weighted optimization (CPWOPT) method is leveraged as benchmark method [198]. In the benchmark method CP rank R and number of iterations set to 15 and 150, respectively, which is similar to the FBCP method.

Table 5.2 Tuning parameter for FBCP-based tensor completion.

Tuning parameter	Value
CP Rank R	250
Tolerance limit	10^{-12}
Initial hyperparameter value	10^{-8}
Number of iterations	150

5.5 Results and discussion

Table 5.3 shows the performance of proposed (FBCP: Pro. (A)) and benchmark (CPWOP: Pro. (B)) methods for the evaluation of estimated tensors based on channel-wise continuous missing percentages with five different bearing fault conditions and their respective RSE values. In different bearing conditions, channel-wise average RSE values are compared with respect to corresponding missing percentages at channel 1, 5, 9 and 11, where channel 1 and 5 corresponds to acoustics signals and channel 9 and 11 contain vibration signals. It is notable to mention that when a varying percentage of continuous missing signal scenarios are introduced at channel 1 then rest of 11 channels remained unchanged. Similar approaches are also applied in channels 5, 9 and 11 respectively. Figure 5.7 demonstrates the performance of estimated signals at the location of missing occurrences (20% missing) and compares with the actual signals among acoustics and vibration channels. In acoustics channel-1, observations 1 and 2 show that estimated signals overlap the actual signals at the location of missing. Their residual plots show the effectiveness of the difference between estimated and actual signals. Similarly, at vibration channel 11, estimated signals overlap the actual at the location of a higher missing percentage (20% missing), and their residual plots show the effectiveness of estimated and actual signals. Figure 5.8 shows an overall trend of RSE value in proposed and benchmark methods with respect to different missing percentages among five different bearing fault conditions. In contrast, it is noticeable that the

proposed method performs better than the benchmark method with higher percentages of missing entries.

Table 5.3 Summary results of proposed (FBCP) and benchmark (CPWOPT) methods.

Bearing conditions	Ch. #	MP: 1 %		MP: 3 %		MP: 5 %		MP: 10 %		MP: 20 %	
		Avg. RSE		Avg. RSE		Avg. RSE		Avg. RSE		Avg. RSE	
		Pro. (A)	Ben. (B)	Pro. (A)	Ben. (B)	Pro. (A)	Ben. (B)	Pro. (A)	Ben. (B)	Pro. (A)	Ben. (B)
Good bearing	Ch. 1	0.0358	0.0443	0.0406	0.0821	0.0453	0.1064	0.0500	0.1601	0.0582	0.2449
	Ch. 5	0.0357	0.0334	0.0392	0.0675	0.0467	0.0830	0.0601	0.1126	0.0825	0.1856
	Ch. 9	0.0339	0.0470	0.0350	0.0879	0.0361	0.1115	**0.0383**	0.1595	**0.0408**	0.2460
	Ch.11	**0.0337**	**0.0331**	**0.0339**	0.0536	**0.0343**	**0.0739**	0.0388	0.1192	0.0423	0.2137
	Avg.	**0.0348**	**0.0395**	**0.0372**	**0.0728**	**0.0406**	**0.0937**	**0.0468**	**0.1379**	**0.0560**	**0.2226**
Ball fault	Ch. 1	0.0347	0.0260	0.0402	0.0450	0.0419	0.0624	0.0511	0.0889	0.0644	0.1415
	Ch. 5	0.0351	0.0215	0.0429	0.0382	0.0469	0.0476	0.0590	0.0720	0.0806	0.1159
	Ch. 9	**0.0280**	0.0216	**0.0280**	0.0441	**0.0286**	0.0583	**0.0293**	0.0860	0.0362	0.1556
	Ch.11	0.0303	**0.0155**	0.0302	**0.0258**	0.0308	**0.0371**	0.0310	**0.0579**	**0.0347**	0.1126
	Avg.	**0.0320**	**0.0212**	**0.0353**	**0.0383**	**0.0370**	**0.0514**	**0.0426**	**0.0762**	**0.0539**	**0.1314**
Inner race fault	Ch. 1	0.0462	0.0175	0.0445	0.0287	0.0437	0.0358	0.0508	0.0539	0.0519	0.0834
	Ch. 5	0.0420	0.0131	0.0434	**0.0220**	0.0463	**0.0284**	0.0470	**0.0443**	0.0560	0.0690
	Ch. 9	0.0468	0.0196	0.0452	0.0372	0.0464	0.0502	0.0473	0.0730	0.0644	0.1407
	Ch.11	**0.0397**	**0.0128**	**0.0400**	0.0262	**0.0425**	0.0350	**0.0439**	0.0520	**0.0500**	0.1114
	Avg.	**0.0437**	**0.0158**	**0.0433**	**0.0285**	**0.0447**	**0.0374**	**0.0472**	**0.0558**	**0.0556**	**0.1011**
Outer race fault	Ch. 1	0.0814	0.0228	0.0828	0.0379	0.0843	0.0491	0.0867	0.0729	0.0916	0.1159
	Ch. 5	0.0811	0.0192	0.0825	0.0305	0.0843	**0.0391**	0.0871	0.0566	0.0924	0.0866
	Ch. 9	0.0819	0.0223	0.0877	0.0430	0.0845	0.0601	0.0896	0.0803	0.0924	0.1234
	Ch.11	**0.0807**	**0.0162**	**0.0814**	**0.0266**	0.0872	0.0399	0.0831	**0.0590**	0.0899	0.1145
	Avg.	**0.0813**	**0.0201**	**0.0836**	**0.0345**	**0.0850**	**0.0471**	**0.0867**	**0.0672**	**0.0916**	**0.1101**
Combined fault	Ch. 1	0.0299	0.0275	0.0343	0.0448	0.0379	0.0579	0.0461	0.0846	0.0597	0.1293
	Ch. 5	0.0322	0.0250	0.0372	0.0406	0.0424	0.0553	0.0528	0.0753	0.0604	0.1117
	Ch. 9	0.0262	0.0192	**0.0265**	0.0393	**0.0272**	0.0536	**0.0288**	0.0769	**0.0313**	0.1328
	Ch.11	**0.0259**	**0.0116**	0.0396	**0.0246**	0.0399	**0.0350**	0.0495	**0.0513**	0.0564	0.1122
	Avg.	**0.0285**	**0.0208**	**0.0344**	**0.0373**	**0.0368**	**0.0505**	**0.0443**	**0.0720**	**0.0519**	**0.1215**

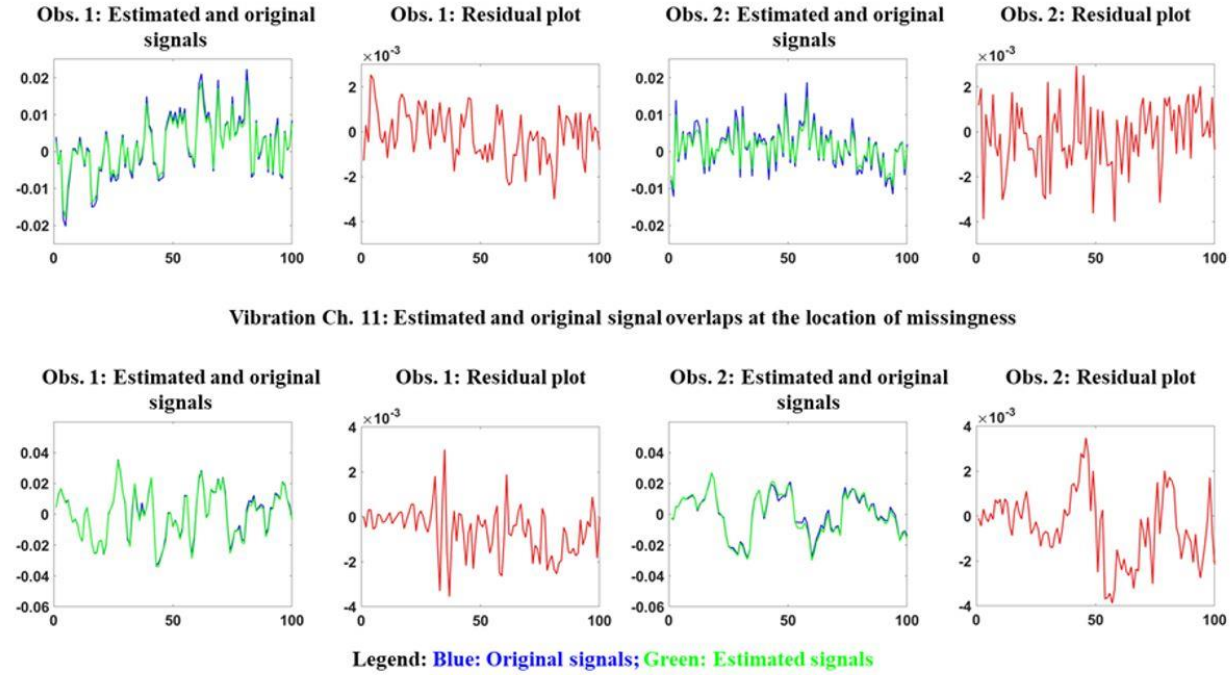

Figure 5.7 Imputation of missing signals at the location of missing occurrences in acoustics and vibration channels (MP: 20%) with FBCP method.

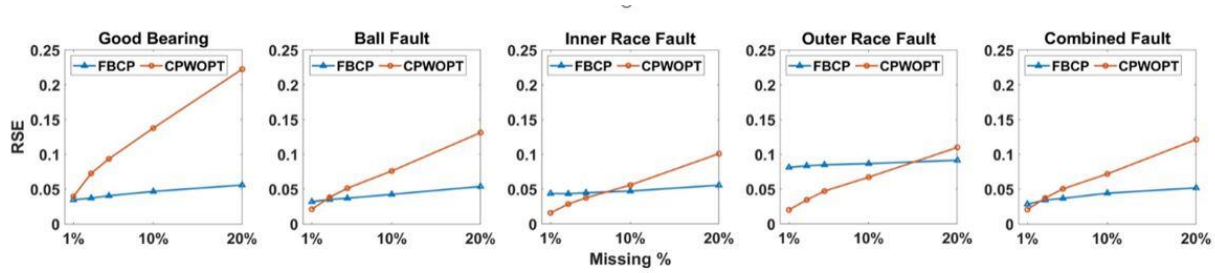

Figure 5.8 Performance evaluation of proposed and benchmark methods with diverse bearing fault conditions.

5.6 Conclusion and future work

The emerging trend of multi-channel sensor fusion is ubiquitous. In the industry 4.0 perspective, heterogeneous sensor fusion can be integrated for real-time machinery fault identification and diagnosis. Multi-channel sensor fusion can be challenging when a substantial amount of missing data occurrence prevails. However, the effectiveness of imputation of missing

sensor signals is also significantly important for monitoring machinery conditions. In quest of the state-of-the-art, this proposed method adopted a fully Bayesian CANDECOMP/PARAFAC factorization (FBCP) method for missing data imputation from diverse bearing fault signals. To validate the effectiveness of this proposed method, a machinery fault simulator is used as a testbed to collect diverse bearing fault signals by integrating an equal number of acoustics (microphones) and vibration (accelerometers) sensors simultaneously. Acoustics and vibration signals are combined by forming time-domain tensors. A varying percentage of continuous missing signal scenarios are generated at random locations among different acoustics and vibration channels, constructing incomplete tensors. Then, the FBCP method is leveraged to complete the incomplete tensors and calculate estimated tensors.

To evaluate the performance of continuous missing data imputation, relative standard errors (RSE) are computed based on the estimated and actual time-domain tensors. The CP weighted optimization (CPWOPT) method is incorporated as a benchmark method to evaluate the effectiveness of the FBCP method. Experimental results show that this proposed method can effectively impute a substantial portion of continuous missing data from diverse bearing fault scenarios. This proposed method can be extended in the following aspects. Firstly, a varying percentage of continuous missing signal scenarios can be introduced among different acoustics and vibration channels at a time. And then evaluate the effectiveness of the FBCP method. Secondly, the extension of this proposed method can be leveraged for bearing faults classification. More specifically, imputed sensor signals can be applied in the Machine Learning tools and evaluated the effectiveness of diverse bearing fault classification with the actual time-domain signals and their respective fault classification results.

CHAPTER VI

DISSERTATION SUMMARY

This chapter concludes the dissertation by outlining the research summary and enumerating future research plans. Given the concurrent challenges of cybermanufacturing systems, three major research objectives are being proposed in this dissertation work. Section 6.1 demonstrates the technical contribution of this dissertation relating cybermanufacturing systems. In section 6.2, future research directions are illustrated based on the current proposed methods.

6.1 Technical contribution of this dissertation by linking cybermanufacturing systems

Cybersecurity frameworks can be leveraged in a wide range of cybermanufacturing operations to make a robust shield against cyberattack space (Table 6.1). Although AI has achieved significant success in modelling and monitoring, manufacturing operations pose inherent challenges, including 1) potential cyber-physical attacks; 2) large volumes of data streams available; 3) ill-structured data, such as missing data. Subsequently, these major challenges hinder effective modeling and monitoring for cybermanufacturing systems' decision-making. Considering the cybersecurity framework, the first research aims to **detect** the *in-situ* additive manufacturing (AM) process authentication problem using high volume video streaming data. By linking the second proposed method, the third research endeavour is aligned to **recovery** systems of multi-channel sensing signals when a substantial amount of missing data exists due to sensor malfunction or transmission issues. Table 6.1 depicts the overall technical contributions of the first and third proposed methods of this dissertation work based on the cybersecurity framework.

Table 6.1 Overall technical contributions in cybermanufacturing systems.

Cybersecurity steps	Proposed research work in cybermanufacturing
Detection	To **detect** layer-wise printing path alteration in AM due to cyberattack space, layer-wise texture analysis based on streamline video analysis is incorporated.
Recovery	To **recover** missing signals from multi-channel sensors in rotary machinery components, tenor factorization method is implemented.

Overview of technical contributions, applications and the broader impact of this dissertation has been presented in Figure 6.1. These proposed methods can be implemented in a wide range of areas, including different AM process, prognostics and health condition monitoring of machineries, and large-scale sensor networks. Overall, broader impact these proposed methods ensure product quality and safety, cybersecurity, reduce manufacturing errors, minimize downtime, and enhance machinery service life.

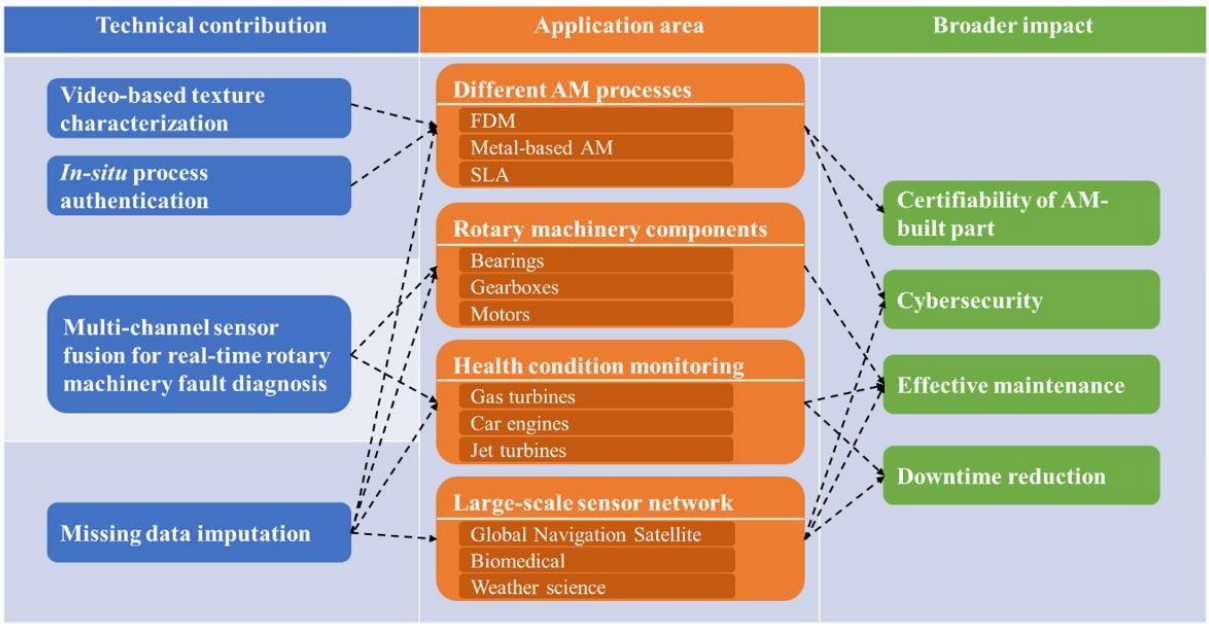

Figure 6.1 Technical contributions, and their applications areas and broader impact.

6.2 Future research directions

The presented dissertation is the beginning of an emerging research trend: data-driven modeling and monitoring of advanced manufacturing systems. The list of future research plans is as follows:

1) Diverse printing path alteration and sensitivity of cyber-physical attack space in AM

A side-channel monitoring approach based on an *in-situ* optical imaging system is established, and a tensor-based layer-wise texture descriptor is constructed to describe the observed printing path. This proposed method can be extended in diverse printing path alteration of AM for sensitivity analysis of cyber-physical attack space. More elaborately speaking, AM parts with diversified geometric features, including different shapes, infill patterns, and infill percentages, will be considered, and their performance will be evaluated.

2) The effectiveness of feature-level sensor fusion with diverse faulty RM components

The second proposed method is aligned with the multi-channel sensor fusion methodology, named frequency-domain multilinear principal component analysis (FDMPCA), by integrating acoustics and vibration signals with different sampling rates for real-time bearing fault diagnosis. This research work can be extended by introducing diverse faulty RM components to bring the robustness of feature-level sensor fusion in predictive maintenance operations.

3) The effectiveness of missing signal imputation

The third proposed method is fully Bayesian CANDECOMP/PARAFAC (FBCP) factorization for missing data imputation of mixed bearing faults signals. The extension of this proposed method can be leveraged for various RM component faults classification. More specifically, imputed sensor signals can be applied in the Machine Learning tools and evaluate the effectiveness of diverse RM component faults classification with the actual time-domain signals and their

respective fault classification results.

BIBLIOGRAPHY

[1] J. Lee, B. Bagheri, and H. A. Kao, "A Cyber-Physical Systems architecture for Industry 4.0-based manufacturing systems," *Manuf. Lett.*, vol. 3, pp. 18–23, 2015, doi: 10.1016/j.mfglet.2014.12.001.

[2] M. Wu *et al.*, "Development of testbed for cyber-manufacturing security issues," *Int. J. Comput. Integr. Manuf.*, vol. 33, no. 3, pp. 302–320, 2020, doi: 10.1080/0951192X.2020.1736711.

[3] V. Gunes, S. Peter, T. Givargis, and F. Vahid, "A survey on concepts, applications, and challenges in cyber-physical systems," *KSII Trans. Internet Inf. Syst.*, vol. 8, no. 12, pp. 4242–4268, 2014, doi: 10.3837/tiis.2014.12.001.

[4] B. B. Cassoli, N. Jourdan, P. H. Nguyen, S. Sen, E. Garcia-Ceja, and J. Metternich, "Frameworks for data-driven quality management in cyber-physical systems for manufacturing: A systematic review," *Procedia CIRP*, vol. 112, pp. 567–572, 2022, doi: 10.1016/j.procir.2022.09.062.

[5] C. Paulsen and P. Toth, "Small Business Information Security: The Fundamentals," Gaithersburg, MD, Oct. 2016. doi: 10.6028/NIST.IR.7621r1.

[6] Z. Song and Y. Moon, "CyberManufacturing system: A solution for sustainable manufacturing," *ASME Int. Mech. Eng. Congr. Expo. Proc.*, vol. 2, no. i, pp. 1–11, 2018, doi: 10.1115/IMECE2018-86092.

[7] M. Moghaddam and A. Deshmukh, "Resilience of cyber-physical manufacturing control systems," *Manuf. Lett.*, vol. 20, pp. 40–44, 2019, doi: 10.1016/j.mfglet.2019.05.002.

[8] M. Powell *et al.*, "Protecting Information and System Integrity in Industrial Control System Environments: Cybersecurity for the Manufacturing Sector," Gaithersburg, MD, Mar. 2022. doi: 10.6028/NIST.SP.1800-10.

[9] M. Fagan, K. N. Megas, K. Scarfone, and M. Smith, "Foundational Cybersecurity Activities for IoT Device Manufacturers," *Nistir 8259*, no. May, p. 27, 2020, [Online]. Available: https://doi.org/10.6028/NIST.IR.8259

[10] S. P. Systems, Z. Guo, Y. Zhang, X. Zhao, and X. Song, "CPS-Based Self-Adaptive Collaborative Control for," *IEEE Trans. Cybern.*, vol. 51, no. 1, pp. 1–11, 2020.

[11] L. Ouyang, J. Chen, Y. Ma, C. Park, and J. Jin, "Bayesian closed-loop robust process design considering model uncertainty and data quality," *IISE Trans.*, vol. 52, no. 3, pp. 288–300, 2020, doi: 10.1080/24725854.2019.1636428.

[12] A. E. Elhabashy, L. J. Wells, J. A. Camelio, and W. H. Woodall, "A cyber-physical attack taxonomy for production systems: a quality control perspective," *J. Intell. Manuf.*, vol. 30, no. 6, pp. 2489–2504, 2019, doi: 10.1007/s10845-018-1408-9.

[13] L. D. Sturm, C. B. Williams, J. A. Camelio, J. White, and R. Parker, "Cyber-physical vulnerabilities in additive manufacturing systems: A case study attack on the.STL file with human subjects," *J. Manuf. Syst.*, vol. 44, pp. 154–164, 2017, doi: 10.1016/j.jmsy.2017.05.007.

[14] M. Wu *et al.*, "Detecting attacks in cybermanufacturing systems: Additive manufacturing example," *MATEC Web Conf.*, vol. 108, pp. 8–11, 2017, doi: 10.1051/matecconf/201710806005.

[15] A. E. Elhabashy, L. J. Wells, and J. A. Camelio, "Cyber-physical attack vulnerabilities in manufacturing quality control tools," *Qual. Eng.*, vol. 32, no. 4, pp. 676–692, 2020, doi: 10.1080/08982112.2020.1737115.

[16] J. Lee, E. Lapira, B. Bagheri, and H. an Kao, "Recent advances and trends in predictive manufacturing systems in big data environment," *Manuf. Lett.*, vol. 1, no. 1, pp. 38–41, 2013, doi: 10.1016/j.mfglet.2013.09.005.

[17] R. Zuech, T. M. Khoshgoftaar, and R. Wald, "Intrusion detection and Big Heterogeneous Data: a Survey," *J. Big Data*, vol. 2, no. 1, 2015, doi: 10.1186/s40537-015-0013-4.

[18] Y. Lu and X. Xu, "Cloud-based manufacturing equipment and big data analytics to enable on-demand manufacturing services," *Robot. Comput. Integr. Manuf.*, vol. 57, no. November 2018, pp. 92–102, 2019, doi: 10.1016/j.rcim.2018.11.006.

[19] Ji Liu, P. Musialski, P. Wonka, and Jieping Ye, "Tensor completion for estimating missing values in visual data," in *2009 IEEE 12th International Conference on Computer Vision*, Sep. 2009, vol. 35, no. 1, pp. 2114–2121. doi: 10.1109/ICCV.2009.5459463.

[20] Q. Zhao, L. Zhang, and A. Cichocki, "Bayesian CP factorization of incomplete tensors with automatic rank determination," *IEEE Trans. Pattern Anal. Mach. Intell.*, vol. 37, no. 9, pp. 1751–1763, 2015, doi: 10.1109/TPAMI.2015.2392756.

[21] D. Kressner, M. Steinlechner, and B. Vandereycken, "Low-rank tensor completion by Riemannian optimization," *BIT Numer. Math.*, vol. 54, no. 2, pp. 447–468, 2014, doi: 10.1007/s10543-013-0455-z.

[22] S. Chen, Y. Meng, H. Tang, Y. Tian, N. He, and C. Shao, “Robust Deep Learning-Based Diagnosis of Mixed Faults in Rotating Machinery,” *IEEE/ASME Trans. Mechatronics*, vol. 25, no. 5, pp. 2167–2176, 2020, doi: 10.1109/TMECH.2020.3007441.

[23] A. Al, C. Liu, C. Kan, and W. Tian, “Securing cyber-physical additive manufacturing systems by in-situ process authentication using streamline video analysis ☆,” *J. Manuf. Syst.*, vol. 62, no. August 2021, pp. 429–440, 2022, doi: 10.1016/j.jmsy.2021.12.007.

[24] A. Al Mamun *et al.*, “Multi-channel sensor fusion for real-time bearing fault diagnosis by frequency-domain multilinear principal component analysis,” *Int. J. Adv. Manuf. Technol.*, vol. 124, no. 3–4, pp. 1321–1334, Jan. 2023, doi: 10.1007/s00170-022-10525-4.

[25] A. Al Mamun, M. Mohammad, L. Bian, T. C. Falls, and W. Tian, “Missing Signal Imputation for Multi-channel Sensing Signals on Rotary Machinery by Tensor Factorization,” *Manuf. Lett.*, vol. 00, no. Accepted, 2023.

[26] M. Aydos, Y. Vural, and A. Tekerek, “Assessing risks and threats with layered approach to Internet of Things security,” *Meas. Control (United Kingdom)*, vol. 52, no. 5–6, pp. 338–353, 2019, doi: 10.1177/0020294019837991.

[27] K. Thakur, M. Qiu, K. Gai, and M. L. Ali, “An Investigation on Cyber Security Threats and Security Models,” *Proc. - 2nd IEEE Int. Conf. Cyber Secur. Cloud Comput. CSCloud 2015 - IEEE Int. Symp. Smart Cloud, IEEE SSC 2015*, pp. 307–311, 2016, doi: 10.1109/CSCloud.2015.71.

[28] J. Jang-Jaccard and S. Nepal, “A survey of emerging threats in cybersecurity,” *J. Comput. Syst. Sci.*, vol. 80, no. 5, pp. 973–993, 2014, doi: 10.1016/j.jcss.2014.02.005.

[29] S. Mittal, P. K. Das, V. Mulwad, A. Joshi, and T. Finin, “CyberTwitter: Using Twitter to generate alerts for cybersecurity threats and vulnerabilities,” *Proc. 2016 IEEE/ACM Int. Conf. Adv. Soc. Networks Anal. Mining, ASONAM 2016*, pp. 860–867, 2016, doi: 10.1109/ASONAM.2016.7752338.

[30] N. Y. Conteh and P. J. Schmick, “Cybersecurity:risks, vulnerabilities and countermeasures to prevent social engineering attacks,” *Int. J. Adv. Comput. Res.*, vol. 6, no. 23, pp. 31–38, 2016, doi: 10.19101/ijacr.2016.623006.

[31] A. Razaque *et al.*, “Survey: Cybersecurity Vulnerabilities, Attacks and Solutions in the Medical Domain,” *IEEE Access*, vol. 7, pp. 168774–168797, 2019, doi: 10.1109/ACCESS.2019.2950849.

[32] K. Ghosh, “Identification and Quantification of Cybersecurity Risk by Likelihood-Severity, Incident-Response and Organizational Asset Valuation Framework,” *SSRN Electron. J.*, 2020, doi: 10.2139/ssrn.3630075.

[33] R. M. Lee, M. J. Assante, and T. Conway, "ICS CP/PE (Cyber-to-Physical or Process Effects) case study paper – German Steel Mill Cyber Attack," *SANS, Ind. Control Syst.*, p. 15, 2014.

[34] T. Alladi, V. Chamola, and S. Zeadally, "Industrial Control Systems: Cyberattack trends and countermeasures," *Comput. Commun.*, vol. 155, no. February, pp. 1–8, 2020, doi: 10.1016/j.comcom.2020.03.007.

[35] M. Bashendy, A. Tantawy, and A. Erradi, "Intrusion response systems for cyber-physical systems: A comprehensive survey," *Comput. Secur.*, vol. 124, p. 102984, 2023, doi: 10.1016/j.cose.2022.102984.

[36] J. Song and Y. Moon, "Security enhancement against insiders in cyber-manufacturing systems," *Procedia Manuf.*, vol. 48, no. 2019, pp. 864–872, 2020, doi: 10.1016/j.promfg.2020.05.124.

[37] M. Caselli, E. Zambon, and F. Kargl, "Sequence-aware intrusion detection in industrial control systems," *CPSS 2015 - Proc. 1st ACM Work. Cyber-Physical Syst. Secur. Part ASIACCS 2015*, pp. 13–24, 2015, doi: 10.1145/2732198.2732200.

[38] T. Cruz *et al.*, "Improving network security monitoring for industrial control systems," *Proc. 2015 IFIP/IEEE Int. Symp. Integr. Netw. Manag. IM 2015*, pp. 878–881, 2015, doi: 10.1109/INM.2015.7140399.

[39] M. Lezzi, M. Lazoi, and A. Corallo, "Cybersecurity for Industry 4.0 in the current literature: A reference framework," *Comput. Ind.*, vol. 103, pp. 97–110, 2018, doi: 10.1016/j.compind.2018.09.004.

[40] K. Stouffer *et al.*, "Cybersecurity Framework Manufacturing Profile Low Security Level Example Implementations Guide : Volume 1 – General Implementation Guidance," *Nistir 8183a*, vol. 1, 2019.

[41] C. Espinoza-Zelaya and Y. B. Moon, "Resilience Enhancing Mechanisms for Cyber-Manufacturing Systems against Cyber-Attacks," *IFAC-PapersOnLine*, vol. 55, no. 10, pp. 2252–2257, 2022, doi: 10.1016/j.ifacol.2022.10.043.

[42] Internet Society, "2018 Cyber Incident & Breach Trends Report | Internet Society," *2018 Cyber Incid. Breach Trends Rep.*, 2018, [Online]. Available: https://www.internetsociety.org/resources/ota/2019/2018-cyber-incident-breach-trends-report/

[43] M. Wu, Z. Song, and Y. B. Moon, "Detecting cyber-physical attacks in CyberManufacturing systems with machine learning methods," *J. Intell. Manuf.*, vol. 30, no. 3, pp. 1111–1123, 2019, doi: 10.1007/s10845-017-1315-5.

[44] M. Shahin, F. F. Chen, A. Hosseinzadeh, H. Bouzary, and R. Rashidifar, “A deep hybrid learning model for detection of cyber attacks in industrial IoT devices,” *Int. J. Adv. Manuf. Technol.*, pp. 1973–1983, 2022, doi: 10.1007/s00170-022-10329-6.

[45] R. Gan, Y. Xiao, J. Shao, and J. Qin, “An Analysis on Optimal Attack Schedule Based on Channel Hopping Scheme in Cyber-Physical Systems,” *IEEE Trans. Cybern.*, vol. 51, no. 2, pp. 994–1003, Feb. 2021, doi: 10.1109/TCYB.2019.2914144.

[46] M. S. Mahmoud, M. M. Hamdan, and U. A. Baroudi, “Secure control of cyber physical systems subject to stochastic distributed DoS and deception attacks,” *Int. J. Syst. Sci.*, vol. 51, no. 9, pp. 1653–1668, 2020, doi: 10.1080/00207721.2020.1772402.

[47] M. M. Hamdan and M. S. Mahmoud, “Secure Filter for Discrete-Time Delayed Systems Subject to Cyber Attacks,” *Cyber-Physical Syst.*, vol. 8, no. 3, pp. 210–232, 2022, doi: 10.1080/23335777.2021.1916230.

[48] L. Zhang, Y. Chen, and M. Li, “Resilient Predictive Control for Cyber–Physical Systems Under Denial-of-Service Attacks,” *IEEE Trans. Circuits Syst. II Express Briefs*, vol. 69, no. 1, pp. 144–148, Jan. 2022, doi: 10.1109/TCSII.2021.3076764.

[49] D. Singh, A. Shukla, and M. Sajwan, “Deep transfer learning framework for the identification of malicious activities to combat cyberattack,” *Futur. Gener. Comput. Syst.*, vol. 125, pp. 687–697, 2021, doi: 10.1016/j.future.2021.07.015.

[50] Q. Abu Al-Haija, “Top-Down Machine Learning-Based Architecture for Cyberattacks Identification and Classification in IoT Communication Networks,” *Front. Big Data*, vol. 4, no. January, pp. 1–18, 2022, doi: 10.3389/fdata.2021.782902.

[51] A. Zedan and N. H. El-Farra, “A machine-learning approach for identification and mitigation of cyberattacks in networked process control systems,” *Chem. Eng. Res. Des.*, vol. 176, pp. 102–115, 2021, doi: 10.1016/j.cherd.2021.09.016.

[52] K. Gai, M. Qiu, and H. Zhao, “Privacy-Preserving Data Encryption Strategy for Big Data in Mobile Cloud Computing,” *IEEE Trans. Big Data*, vol. 7, no. 4, pp. 678–688, 2021, doi: 10.1109/TBDATA.2017.2705807.

[53] X. Shen, L. Zhu, C. Xu, K. Sharif, and R. Lu, “A privacy-preserving data aggregation scheme for dynamic groups in fog computing,” *Inf. Sci. (Ny).*, vol. 514, pp. 118–130, 2020, doi: 10.1016/j.ins.2019.12.007.

[54] X. Dong, J. Yu, Y. Luo, Y. Chen, G. Xue, and M. Li, “Achieving an effective, scalable and privacy-preserving data sharing service in cloud computing,” *Comput. Secur.*, vol. 42, pp. 151–164, 2014, doi: 10.1016/j.cose.2013.12.002.

[55] M. M. Rana, L. Li, and S. W. Su, “Cyber attack protection and control of microgrids,” *IEEE/CAA J. Autom. Sin.*, vol. 5, no. 2, pp. 602–609, 2018, doi: 10.1109/JAS.2017.7510655.

[56] I. Kotenko, I. Saenko, O. Lauta, and M. Karpov, “Methodology for management of the protection system of smart power supply networks in the context of cyberattacks,” *Energies*, vol. 14, no. 18, pp. 1–39, 2021, doi: 10.3390/en14185963.

[57] J. Khazaei and M. H. Amini, “Protection of large-scale smart grids against false data injection cyberattacks leading to blackouts,” *Int. J. Crit. Infrastruct. Prot.*, vol. 35, no. March, p. 100457, 2021, doi: 10.1016/j.ijcip.2021.100457.

[58] M. Wu and Y. B. Moon, “Intrusion detection system for cyber-manufacturing system,” *J. Manuf. Sci. Eng. Trans. ASME*, vol. 141, no. 3, 2019, doi: 10.1115/1.4042053.

[59] Q. Ao, “An Intrusion Detection Method for Industrial Control System against Stealthy Attack,” *Proc. - 2020 7th Int. Conf. Dependable Syst. Their Appl. DSA 2020*, pp. 157–161, 2020, doi: 10.1109/DSA51864.2020.00028.

[60] Y. Gao, J. Chen, H. Miao, B. Song, Y. Lu, and W. Pan, “Self-Learning Spatial Distribution-Based Intrusion Detection for Industrial Cyber-Physical Systems,” *IEEE Trans. Comput. Soc. Syst.*, pp. 1–10, 2022, doi: 10.1109/TCSS.2021.3135586.

[61] A. Rashid, M. J. Siddique, and S. M. Ahmed, “Machine and Deep Learning Based Comparative Analysis Using Hybrid Approaches for Intrusion Detection System,” *3rd Int. Conf. Adv. Comput. Sci. ICACS 2020*, 2020, doi: 10.1109/ICACS47775.2020.9055946.

[62] A. Aribisala, M. S. Khan, and G. Husari, “Feed-Forward Intrusion Detection and Classification on a Smart Grid Network,” *2022 IEEE 12th Annu. Comput. Commun. Work. Conf. CCWC 2022*, pp. 99–105, 2022, doi: 10.1109/CCWC54503.2022.9720898.

[63] H. Xu and B. Lian, “Fault detection for multi-source integrated navigation system using fully convolutional neural network,” *IET Radar, Sonar Navig.*, vol. 12, no. 7, pp. 774–782, 2018, doi: 10.1049/iet-rsn.2017.0424.

[64] X. Xu, Z. Tao, W. Ming, Q. An, and M. Chen, “Intelligent monitoring and diagnostics using a novel integrated model based on deep learning and multi-sensor feature fusion,” *Meas. J. Int. Meas. Confed.*, vol. 165, p. 108086, 2020, doi: 10.1016/j.measurement.2020.108086.

[65] J. Zhang, L. Cai, and S. Zhang, “Malicious cognitive user identification algorithm in centralized spectrum sensing system,” *Futur. Internet*, vol. 9, no. 4, 2017, doi: 10.3390/fi9040079.

[66] X. Wang, S. Ekin, and E. Serpedin, “Joint spectrum sensing and resource allocation in multi-band-multi-user cognitive radio networks,” *IEEE Trans. Commun.*, vol. 66, no. 8, pp. 3281–3293, 2018, doi: 10.1109/TCOMM.2018.2807432.

[67] Y. Li and Q. Peng, “Achieving secure spectrum sensing in presence of malicious attacks utilizing unsupervised machine learning,” *Proc. - IEEE Mil. Commun. Conf. MILCOM*, pp. 174–179, 2016, doi: 10.1109/MILCOM.2016.7795321.

[68] S. Anwar, J. M. Zain, M. F. Zolkipli, Z. Inayat, A. N. Jabir, and J. B. Odili, “Response option for attacks detected by intrusion detection system,” *2015 4th Int. Conf. Softw. Eng. Comput. Syst. ICSECS 2015 Virtuous Softw. Solut. Big Data*, pp. 195–200, 2015, doi: 10.1109/ICSECS.2015.7333109.

[69] Z. Inayat, A. Gani, N. B. Anuar, M. K. Khan, and S. Anwar, “Intrusion response systems: Foundations, design, and challenges,” *J. Netw. Comput. Appl.*, vol. 62, pp. 53–74, 2016, doi: 10.1016/j.jnca.2015.12.006.

[70] A. Shameli-Sendi, J. Desfossez, M. Dagenais, and M. Jabbarifar, “A retroactive-burst framework for automated intrusion response system,” *J. Comput. Networks Commun.*, vol. 2013, 2013, doi: 10.1155/2013/134760.

[71] S. Adepu and A. Mathur, “An Investigation into the Response of a Water Treatment System to Cyber Attacks,” *Proc. IEEE Int. Symp. High Assur. Syst. Eng.*, vol. 2016-March, pp. 141–148, 2016, doi: 10.1109/HASE.2016.14.

[72] O. Boyaci, M. R. Narimani, K. Davis, and E. Serpedin, “Infinite Impulse Response Graph Neural Networks for Cyberattack Localization in Smart Grids,” Jun. 2022, [Online]. Available: http://arxiv.org/abs/2206.12527

[73] J. Wang, N. Varshney, C. Gentile, S. Blandino, J. Chuang, and N. Golmie, “Integrated Sensing and Communication: Enabling Techniques, Applications, Tools and Data Sets, Standardization, and Future Directions,” *IEEE Internet Things J.*, vol. 9, no. 23, pp. 23416–23440, 2022, doi: 10.1109/JIOT.2022.3190845.

[74] D. Shah, A. Hancock, A. Skjellum, J. Wang, and Q. P. He, “Challenges and opportunities for IoT-enabled cybermanufacturing: what we learned from an IoT-enabled manufacturing technology testbed,” *Proc. Found. Comput. Aided Process Oper. / Chem. Process Control*, p. 66, 2017.

[75] A. Rahiminejad *et al.*, “A resilience-based recovery scheme for smart grid restoration following cyberattacks to substations,” *Int. J. Electr. Power Energy Syst.*, vol. 145, no. September 2022, p. 108610, 2023, doi: 10.1016/j.ijepes.2022.108610.

[76] H. Gong, K. Rafi, H. Gu, G. D. Janaki Ram, T. Starr, and B. Stucker, "Influence of defects on mechanical properties of Ti-6Al-4V components produced by selective laser melting and electron beam melting," *Mater. Des.*, vol. 86, pp. 545–554, 2015, doi: 10.1016/j.matdes.2015.07.147.

[77] M. Seifi, A. Salem, J. Beuth, O. L. A. Harrysson, and J. J. Lewandowski, "Overview of Materials Qualification Needs for Metal Additive Manufacturing," vol. 68, no. 3, 2016, doi: 10.1007/s11837-015-1810-0.

[78] M. Seifi *et al.*, "Progress Towards Metal Additive Manufacturing Standardization to Support Qualification and Certification," *Jom*, vol. 69, no. 3, pp. 439–455, 2017, doi: 10.1007/s11837-017-2265-2.

[79] J. M. Waller, B. H. Parker, K. L. Hodges, E. R. Burke, J. L. Walker, and E. R. Generazio, "Nondestructive Evaluation of Additive Manufacturing State-of-the-Discipline Report Prepared for," no. November, 2014.

[80] Q. Y. Lu and C. H. Wong, "Applications of non-destructive testing techniques for post-process control of additively manufactured parts," *Virtual Phys. Prototyp.*, vol. 12, no. 4, pp. 301–321, 2017, doi: 10.1080/17452759.2017.1357319.

[81] F. Caiazzo, F. Cardaropoli, V. Alfieri, V. Sergi, and L. Cuccaro, "Experimental analysis of Selective Laser Melting process for Ti-6Al-4V turbine blade manufacturing," vol. 8677, pp. 1–10, 2013, doi: 10.1117/12.2010577.

[82] S. Everton *et al.*, "Evaluation of laser ultrasonic testing for inspection of metal additive manufacturing," vol. 9353, pp. 1–8, 2015, doi: 10.1117/12.2078768.

[83] A. Toma, R. Condruz, R. Carlanescu, and I. Daniel, "A mini-review on non-destructive techniques for additive manufactured metal parts," *AIP Conf. Proc.*, vol. 2302, no. December, 2020, doi: 10.1063/5.0033732.

[84] X. Zhang *et al.*, "Correlation approach for quality assurance of additive manufactured parts based on optical metrology," *J. Manuf. Process.*, vol. 53, no. May 2019, pp. 310–317, 2020, doi: 10.1016/j.jmapro.2020.02.037.

[85] P. I. Stavroulakis and R. K. Leach, "Invited Review Article: Review of post-process optical form metrology for industrial-grade metal additive manufactured parts," *Rev. Sci. Instrum.*, vol. 87, no. 4, pp. 1–15, 2016, doi: 10.1063/1.4944983.

[86] W. Du, Q. Bai, Y. Wang, and B. Zhang, "Eddy current detection of subsurface defects for additive/subtractive hybrid manufacturing," *Int. J. Adv. Manuf. Technol.*, vol. 95, no. 9–12, pp. 3185–3195, 2018, doi: 10.1007/s00170-017-1354-2.

[87] M. I. Albakri, L. D. Sturm, C. B. Williams, and P. A. Tarazaga, “Impedance-based non-destructive evaluation of additively manufactured parts,” *Rapid Prototyp. J.*, vol. 23, no. 3, pp. 589–601, Jan. 2017, doi: 10.1108/RPJ-03-2016-0046.

[88] G. Park, H. Sohn, C. R. Farrar, and D. J. Inman, “Overview of Piezoelectric Impedance-Based Health Monitoring and Path Forward,” vol. 35, no. 6, pp. 451–463, 2003.

[89] A. Thompson, I. Maskery, and R. K. Leach, “X-ray computed tomography for additive manufacturing: A review,” *Meas. Sci. Technol.*, vol. 27, no. 7, 2016, doi: 10.1088/0957-0233/27/7/072001.

[90] M. Pavan, T. Craeghs, R. Verhelst, O. Ducatteeuw, J. Kruth, and W. Dewulf, “Case Studies in Nondestructive Testing and Evaluation CT-based quality control of Laser Sintering of Polymers,” *Case Stud. Nondestruct. Test. Eval.*, vol. 1, pp. 1–7, 2016, doi: 10.1016/j.csndt.2016.04.004.

[91] L. Koester, H. Taheri, L. J. Bond, D. Barnard, and J. Gray, “Additive manufacturing metrology: State of the art and needs assessment,” *AIP Conf. Proc.*, vol. 1706, 2016, doi: 10.1063/1.4940604.

[92] G. Tapia and A. Elwany, “A Review on Process Monitoring and Control in Metal-Based Additive Manufacturing,” *J. Manuf. Sci. Eng. Trans. ASME*, vol. 136, no. 6, pp. 1–10, 2014, doi: 10.1115/1.4028540.

[93] K. Zeng, D. Pal, and B. Stucker, “A review of thermal analysis methods in Laser Sintering and Selective Laser Melting Kai Zeng, Deepankar Pal, Brent Stucker Department of Industrial Engineering, University of Louisville, Louisville, KY 40292,” pp. 796–814.

[94] E. Rodriguez *et al.*, “Integration of a thermal imaging feedback control system in electron beam melting,” *23rd Annu. Int. Solid Free. Fabr. Symp. - An Addit. Manuf. Conf. SFF 2012*, no. Figure 1, pp. 945–961, 2012.

[95] F. Imani, R. Chen, E. Diewald, E. Reutzel, and H. Yang, “Deep learning of variant geometry in layerwise imaging profiles for additive manufacturing quality control,” *J. Manuf. Sci. Eng. Trans. ASME*, vol. 141, no. 11, 2019, doi: 10.1115/1.4044420.

[96] Q. Tian, S. Guo, E. Melder, L. Bian, and W. Guo, “Deep learning-based data fusion method for in situ porosity detection in laser-based additive manufacturing,” *J. Manuf. Sci. Eng. Trans. ASME*, vol. 143, no. 4, pp. 1–14, 2021, doi: 10.1115/1.4048957.

[97] S. H. Seifi, W. Tian, H. Doude, M. A. Tschopp, and L. Bian, “Layer-Wise Modeling and Anomaly Detection for Laser-Based Additive Manufacturing,” *J. Manuf. Sci. Eng. Trans. ASME*, vol. 141, no. 8, pp. 1–12, 2019, doi: 10.1115/1.4043898.

[98] L. Scime and J. Beuth, “Anomaly detection and classification in a laser powder bed additive manufacturing process using a trained computer vision algorithm,” *Addit. Manuf.*, vol. 19, pp. 114–126, 2018, doi: 10.1016/j.addma.2017.11.009.

[99] C. Liu, A. C. C. Law, D. Roberson, and Z. (James) Kong, “Image analysis-based closed loop quality control for additive manufacturing with fused filament fabrication,” *J. Manuf. Syst.*, vol. 51, no. April, pp. 75–86, 2019, doi: 10.1016/j.jmsy.2019.04.002.

[100] Y. Cheng and M. A. Jafari, “Vision-based online process control in manufacturing applications,” *IEEE Trans. Autom. Sci. Eng.*, vol. 5, no. 1, pp. 140–153, 2008, doi: 10.1109/TASE.2007.912058.

[101] Z. Ye, C. Liu, W. Tian, and C. Kan, “A Deep Learning Approach for the Identification of Small Process Shifts in Additive Manufacturing using 3D Point Clouds,” *Procedia Manuf.*, vol. 48, pp. 770–775, 2020, doi: 10.1016/j.promfg.2020.05.112.

[102] T. Craeghs, S. Clijsters, J. P. Kruth, F. Bechmann, and M. C. Ebert, “Detection of Process Failures in Layerwise Laser Melting with Optical Process Monitoring,” *Phys. Procedia*, vol. 39, pp. 753–759, 2012, doi: 10.1016/j.phpro.2012.10.097.

[103] O. Holzmond and X. Li, “In situ real time defect detection of 3D printed parts,” *Addit. Manuf.*, vol. 17, pp. 135–142, 2017, doi: 10.1016/j.addma.2017.08.003.

[104] M. Yampolskiy *et al.*, “Security of additive manufacturing: Attack taxonomy and survey,” *Addit. Manuf.*, vol. 21, pp. 431–457, 2018, doi: 10.1016/j.addma.2018.03.015.

[105] S. M. Bridges, K. Keiser, N. Sissom, and S. J. Graves, “Cyber security for additive manufacturing,” *ACM Int. Conf. Proceeding Ser.*, vol. 06-08-Apri, pp. 1–3, 2015, doi: 10.1145/2746266.2746280.

[106] C. Liu, C. Kan, and W. Tian, “An Online Side Channel Monitoring Approach for Cyber-physical Attack Detection of Additive Manufacturing,” 2020.

[107] H. Turner, J. White, J. A. Camelio, C. Williams, B. Amos, and R. Parker, “Bad Parts: Are Our Manufacturing Systems at Risk of Silent Cyberattacks?,” *IEEE Secur. Priv.*, vol. 13, no. 3, pp. 40–47, 2015, doi: 10.1109/MSP.2015.60.

[108] S. E. Zeltmann, N. Gupta, N. G. Tsoutsos, M. Maniatakos, J. Rajendran, and R. Karri, “Manufacturing and Security Challenges in 3D Printing,” *Jom*, vol. 68, no. 7, pp. 1872–1881, 2016, doi: 10.1007/s11837-016-1937-7.

[109] J. Brandman, L. Sturm, J. White, and C. Williams, “A physical hash for preventing and detecting cyber-physical attacks in additive manufacturing systems,” *J. Manuf. Syst.*, vol. 56, no. May, pp. 202–212, 2020, doi: 10.1016/j.jmsy.2020.05.014.

[110] S. B. Moore, W. B. Glisson, and M. Yampolskiy, “Implications of malicious 3D printer firmware,” *Proc. Annu. Hawaii Int. Conf. Syst. Sci.*, vol. 2017-Janua, pp. 6089–6098, 2017, doi: 10.24251/hicss.2017.735.

[111] Y. Gao, W. Wang, W. Xu, C. Zhou, Z. Jin, and B. Li, “Watching and Safeguarding Your 3D Printer: Online Process Monitoring Against Cyber-Physical Attacks,” *Proc. ACM Interactive, Mobile, Wearable Ubiquitous Technol.*, vol. 2, no. 3, p. 108, 2018.

[112] D. Genkin, M. Pattani, R. Schuster, and E. Tromer, “Synesthesia: Detecting screen content via remote acoustic side channels,” *Proc. - IEEE Symp. Secur. Priv.*, vol. 2019-May, pp. 853–869, 2019, doi: 10.1109/SP.2019.00074.

[113] S. K. Arul Prakash, T. Mahan, G. Williams, C. McComb, J. Menold, and C. S. Tucker, “Detection of System Compromise in Additive Manufacturing Using Video Motion Magnification,” *J. Mech. Des.*, vol. 142, no. 3, pp. 1–11, 2020, doi: 10.1115/1.4045547.

[114] S. Belikovetsky, Y. Solewicz, M. Yampolskiy, J. Toh, and Y. Elovici, “Digital Audio Signature for 3D Printing Integrity,” *IEEE Trans. Inf. Forensics Secur.*, vol. PP, no. c, p. 1, 2018, doi: 10.1109/TIFS.2018.2851584.

[115] J. Brandman, L. Sturm, J. White, and C. Williams, “A physical hash for preventing and detecting cyber-physical attacks in additive manufacturing systems,” *J. Manuf. Syst.*, vol. 56, no. May, pp. 202–212, 2020, doi: 10.1016/j.jmsy.2020.05.014.

[116] S. Yu and S. Member, “Sabotage Attack Detection for Additive Manufacturing Systems,” vol. 8, 2020.

[117] Z. Duan, T. Wu, S. Guo, T. Shao, R. Malekian, and Z. Li, “Development and trend of condition monitoring and fault diagnosis of multi-sensors information fusion for rolling bearings: a review,” *Int. J. Adv. Manuf. Technol.*, vol. 96, no. 1–4, pp. 803–819, 2018, doi: 10.1007/s00170-017-1474-8.

[118] A. K. S. Jardine, D. Lin, and D. Banjevic, “A review on machinery diagnostics and prognostics implementing condition-based maintenance,” *Mech. Syst. Signal Process.*, vol. 20, no. 7, pp. 1483–1510, 2006, doi: 10.1016/j.ymssp.2005.09.012.

[119] Y. LI, X. DU, F. WAN, X. WANG, and H. YU, “Rotating machinery fault diagnosis based on convolutional neural network and infrared thermal imaging,” *Chinese J. Aeronaut.*, vol. 33, no. 2, pp. 427–438, Feb. 2020, doi: 10.1016/j.cja.2019.08.014.

[120] P. Henriquez, J. B. Alonso, M. A. Ferrer, and C. M. Travieso, “Review of Automatic Fault Diagnosis Systems Using Audio and Vibration Signals,” *IEEE Trans. Syst. Man, Cybern. Syst.*, vol. 44, no. 5, pp. 642–652, May 2014, doi: 10.1109/TSMCC.2013.2257752.

[121] N. Tandon and B. C. Nakra, “Comparison of vibration and acoustic measurement techniques for the condition monitoring of rolling element bearings,” *Tribol. Int.*, vol. 25, no. 3, pp. 205–212, 1992, doi: 10.1016/0301-679X(92)90050-W.

[122] N. Baydar and A. Ball, “Detection of gear failures via vibration and acoustic signals using wavelet transform,” *Mech. Syst. Signal Process.*, vol. 17, no. 4, pp. 787–804, 2003, doi: 10.1006/mssp.2001.1435.

[123] L. J. Currano *et al.*, “Latching ultra-low power MEMS shock sensors for acceleration monitoring,” *Sensors Actuators, A Phys.*, vol. 147, no. 2, pp. 490–497, 2008, doi: 10.1016/j.sna.2008.06.009.

[124] H. Van Tran, T. H. Ngo, N. D. K. Tran, T. N. Dang, T. P. Dao, and D. A. Wang, “A threshold accelerometer based on a tristable mechanism,” *Mechatronics*, vol. 53, no. May, pp. 39–55, 2018, doi: 10.1016/j.mechatronics.2018.05.013.

[125] T. Wang, G. Lu, and P. Yan, “A novel statistical time-frequency analysis for rotating machine condition monitoring,” *IEEE Trans. Ind. Electron.*, vol. 67, no. 1, pp. 531–541, 2020, doi: 10.1109/TIE.2019.2896109.

[126] S. Hao, F. Ge, Y. Li, and J. Jiang, “Multisensor bearing fault diagnosis based on one-dimensional convolutional long short-term memory networks,” *Measurement*, vol. 159, p. 107802, 2020, doi: 10.1016/j.measurement.2020.107802.

[127] R. F. R. Junior, I. A. dos S. Areias, M. M. Campos, C. E. Teixeira, L. E. B. da Silva, and G. F. Gomes, “Fault detection and diagnosis in electric motors using 1d convolutional neural networks with multi-channel vibration signals,” *Measurement*, vol. 190, no. October 2021, p. 110759, Feb. 2022, doi: 10.1016/j.measurement.2022.110759.

[128] P. Stavropoulos, A. Papacharalampopoulos, and T. Souflas, “Indirect online tool wear monitoring and model-based identification of process-related signal,” *Adv. Mech. Eng.*, vol. 12, no. 5, pp. 1–12, 2020, doi: 10.1177/1687814020919209.

[129] Y. Yao *et al.*, “End-To-End Convolutional Neural Network Model for Gear Fault Diagnosis Based on Sound Signals,” *Appl. Sci.*, vol. 8, no. 9, p. 1584, Sep. 2018, doi: 10.3390/app8091584.

[130] J. A. Duro, J. A. Padget, C. R. Bowen, H. A. Kim, and A. Nassehi, “Multi-sensor data fusion framework for CNC machining monitoring,” *Mech. Syst. Signal Process.*, vol. 66–67, pp. 505–520, 2016, doi: 10.1016/j.ymssp.2015.04.019.

[131] F. Ciampa, P. Mahmoodi, F. Pinto, and M. Meo, “Recent Advances in Active Infrared Thermography for Non-Destructive Testing of Aerospace Components,” *Sensors*, vol. 18, no. 2, p. 609, Feb. 2018, doi: 10.3390/s18020609.

[132] A. Laborda, A. Robinson, S. Wang, Y. Zhang, and P. Reed, “Fatigue assessment of multilayer coatings using lock-in thermography,” *Mater. Des.*, vol. 141, pp. 361–373, 2018, doi: 10.1016/j.matdes.2018.01.004.

[133] S. A. Grammatikos, E. Z. Kordatos, T. E. Matikas, and A. S. Paipetis, “On the fatigue response of a bonded repaired aerospace composite using thermography,” *Compos. Struct.*, vol. 188, no. January, pp. 461–469, 2018, doi: 10.1016/j.compstruct.2018.01.035.

[134] O. Janssens *et al.*, “Thermal image based fault diagnosis for rotating machinery,” *Infrared Phys. Technol.*, vol. 73, pp. 78–87, 2015, doi: 10.1016/j.infrared.2015.09.004.

[135] H. Shao *et al.*, “Fault Diagnosis of a Rotor-Bearing System under Variable Rotating Speeds Using Two-Stage Parameter Transfer and Infrared Thermal Images,” *IEEE Trans. Instrum. Meas.*, vol. 70, pp. 1–11, 2021, doi: 10.1109/TIM.2021.3111977.

[136] X. Wang, D. Mao, and X. Li, “Bearing fault diagnosis based on vibro-acoustic data fusion and 1D-CNN network,” *Measurement*, vol. 173, no. June 2020, p. 108518, 2021, doi: 10.1016/j.measurement.2020.108518.

[137] R. S. Gunerkar and A. K. Jalan, “Classification of Ball Bearing Faults Using Vibro-Acoustic Sensor Data Fusion,” *Exp. Tech.*, vol. 43, no. 5, pp. 635–643, 2019, doi: 10.1007/s40799-019-00324-0.

[138] T. Mian, A. Choudhary, and S. Fatima, “A sensor fusion based approach for bearing fault diagnosis of rotating machine,” *Proc. Inst. Mech. Eng. Part O J. Risk Reliab.*, pp. 1–15, 2021, doi: 10.1177/1748006X211044843.

[139] R. C. Luo, C. C. Chang, and C. C. Lai, “Multisensor fusion and integration: Theories, applications, and its perspectives,” *IEEE Sens. J.*, vol. 11, no. 12, pp. 3122–3138, 2011, doi: 10.1109/JSEN.2011.2166383.

[140] R. Gravina, P. Alinia, H. Ghasemzadeh, and G. Fortino, “Multi-sensor fusion in body sensor networks: State-of-the-art and research challenges,” *Inf. Fusion*, vol. 35, pp. 1339–1351, 2017, doi: 10.1016/j.inffus.2016.09.005.

[141] Q. Miao and V. Makis, “Condition monitoring and classification of rotating machinery using wavelets and hidden Markov models,” *Mech. Syst. Signal Process.*, vol. 21, no. 2, pp. 840–855, Feb. 2007, doi: 10.1016/j.ymssp.2006.01.009.

[142] T. Prasad and S. Das, “Multi-sensor data fusion using support vector machine for motor fault detection,” vol. 217, pp. 96–107, 2012, doi: 10.1016/j.ins.2012.06.016.

[143] Q. Liu and H. P. Wang, “A case study on multisensor data fusion for imbalance diagnosis of rotating machinery,” *Artif. Intell. Eng. Des. Anal. Manuf. AIEDAM*, vol. 15, no. 3, pp. 203–210, 2001, doi: 10.1017/S0890060401153011.

[144] P. Stavropoulos, A. Papacharalampopoulos, K. Sabatakakis, and D. Mourtzis, "Quality Monitoring of Manufacturing Processes based on Full Data Utilization," *Procedia CIRP*, vol. 104, no. March, pp. 1656–1661, 2021, doi: 10.1016/j.procir.2021.11.279.

[145] R. Zebari, A. Abdulazeez, D. Zeebaree, D. Zebari, and J. Saeed, "A Comprehensive Review of Dimensionality Reduction Techniques for Feature Selection and Feature Extraction," *J. Appl. Sci. Technol. Trends*, vol. 1, no. 2, pp. 56–70, 2020, doi: 10.38094/jastt1224.

[146] Y. Yuan and C. Chen, "Fault detection of rolling bearing based on principal component analysis and empirical mode decomposition," *AIMS Math.*, vol. 5, no. 6, pp. 5916–5938, 2020, doi: 10.3934/math.2020379.

[147] W. Li, F. Gu, A. D. Ball, A. Y. T. Leung, and C. E. Phipps, "A study of the noise from diesel engines using the independent component analysis," *Mech. Syst. Signal Process.*, vol. 15, no. 6, pp. 1165–1184, 2001, doi: 10.1006/mssp.2000.1366.

[148] F. Wang, J. Sun, D. Yan, S. Zhang, L. Cui, and Y. Xu, "A feature extraction method for fault classification of rolling bearing based on PCA," *J. Phys. Conf. Ser.*, vol. 628, no. 1, 2015, doi: 10.1088/1742-6596/628/1/012079.

[149] K. Zhang, Y. Li, P. Scarf, and A. Ball, "Feature selection for high-dimensional machinery fault diagnosis data using multiple models and Radial Basis Function networks," *Neurocomputing*, vol. 74, no. 17, pp. 2941–2952, 2011, doi: 10.1016/j.neucom.2011.03.043.

[150] C. Hu, S. He, and Y. Wang, "A classification method to detect faults in a rotating machinery based on kernelled support tensor machine and multilinear principal component analysis," *Appl. Intell.*, vol. 51, no. 4, pp. 2609–2621, 2021, doi: 10.1007/s10489-020-02011-9.

[151] X. Li, W. Zhang, Q. Ding, and J.-Q. Sun, "Intelligent rotating machinery fault diagnosis based on deep learning using data augmentation," *J. Intell. Manuf.*, vol. 31, no. 2, pp. 433–452, Feb. 2020, doi: 10.1007/s10845-018-1456-1.

[152] Y. Wu, F. Yang, Y. Liu, X. Zha, and S. Yuan, "A Comparison of 1-D and 2-D Deep Convolutional Neural Networks in ECG Classification," pp. 48–51.

[153] D. T. Hoang and H. J. Kang, "Rolling element bearing fault diagnosis using convolutional neural network and vibration image," *Cogn. Syst. Res.*, vol. 53, pp. 42–50, 2019, doi: 10.1016/j.cogsys.2018.03.002.

[154] H. Shao, H. Jiang, H. Zhao, and F. Wang, "A novel deep autoencoder feature learning method for rotating machinery fault diagnosis," *Mech. Syst. Signal Process.*, vol. 95, pp. 187–204, 2017, doi: 10.1016/j.ymssp.2017.03.034.

[155] B. V. Dasarathy, “Sensor fusion potential exploitation-innovative architectures and illustrative applications,” *Proc. IEEE*, vol. 85, no. 1, pp. 24–38, 1997, doi: 10.1109/5.554206.

[156] B. S. Yang and K. J. Kim, “Application of Dempster-Shafer theory in fault diagnosis of induction motors using vibration and current signals,” *Mech. Syst. Signal Process.*, vol. 20, no. 2, pp. 403–420, 2006, doi: 10.1016/j.ymssp.2004.10.010.

[157] T. Wang, G. Lu, and P. Yan, “Multi-sensors based condition monitoring of rotary machines: An approach of multidimensional time-series analysis,” *Meas. J. Int. Meas. Confed.*, vol. 134, pp. 326–335, 2019, doi: 10.1016/j.measurement.2018.10.089.

[158] Y. Lei, B. Yang, X. Jiang, F. Jia, N. Li, and A. K. Nandi, “Applications of machine learning to machine fault diagnosis: A review and roadmap,” *Mech. Syst. Signal Process.*, vol. 138, p. 106587, 2020, doi: 10.1016/j.ymssp.2019.106587.

[159] S. Planet and I. Iriondo, “Comparison between decision-level and feature-level fusion of acoustic and linguistic features for spontaneous emotion recognition,” *Iber. Conf. Inf. Syst. Technol. Cist.*, 2012.

[160] M. Huang, Z. Liu, and Y. Tao, “Mechanical fault diagnosis and prediction in IoT based on multi-source sensing data fusion,” *Simul. Model. Pract. Theory*, vol. 102, no. July 2019, p. 101981, 2020, doi: 10.1016/j.simpat.2019.101981.

[161] C. K. Enders, “Listwise Deletion,” in *Dictionary of Statistics & Methodology*, 2455 Teller Road, Thousand Oaks California 91320 United States of America: SAGE Publications, Inc., 2005. doi: 10.4135/9781412983907.n1075.

[162] A. M. Sefidian and N. Daneshpour, “Missing value imputation using a novel grey based fuzzy c-means, mutual information based feature selection, and regression model,” *Expert Syst. Appl.*, vol. 115, pp. 68–94, Jan. 2019, doi: 10.1016/j.eswa.2018.07.057.

[163] T. Canchala-Nastar, Y. Carvajal-Escobar, W. Alfonso-Morales, W. Loaiza Cerón, and E. Caicedo, “Estimation of missing data of monthly rainfall in southwestern Colombia using artificial neural networks,” *Data Br.*, vol. 26, p. 104517, Oct. 2019, doi: 10.1016/j.dib.2019.104517.

[164] A. Z. Alruhaymi and C. J. Kim, “Study on the Missing Data Mechanisms and Imputation Methods,” *Open J. Stat.*, vol. 11, no. 04, pp. 477–492, 2021, doi: 10.4236/ojs.2021.114030.

[165] M. Zhao, Y. Li, S. Chen, and B. Li, “Missing value recovery for encoder signals using improved low-rank approximation,” *Mech. Syst. Signal Process.*, vol. 139, p. 106595, May 2020, doi: 10.1016/j.ymssp.2019.106595.

[166] Q. Ma, Y. Gu, W.-C. Lee, and G. Yu, "Order-Sensitive Imputation for Clustered Missing Values (Extended Abstract)," in *2019 IEEE 35th International Conference on Data Engineering (ICDE)*, Apr. 2019, vol. 2019-April, no. 1, pp. 2147–2148. doi: 10.1109/ICDE.2019.00268.

[167] J. Zhu, Z. Ge, Z. Song, and F. Gao, "Review and big data perspectives on robust data mining approaches for industrial process modeling with outliers and missing data," *Annu. Rev. Control*, vol. 46, pp. 107–133, 2018, doi: 10.1016/j.arcontrol.2018.09.003.

[168] Y. Li *et al.*, "A large-scale sensor missing data imputation framework for dams using deep learning and transfer learning strategy," *Measurement*, vol. 178, no. April, p. 109377, Jun. 2021, doi: 10.1016/j.measurement.2021.109377.

[169] D. B. RUBIN, "Inference and missing data," *Biometrika*, vol. 63, no. 3, pp. 581–592, 1976, doi: 10.1093/biomet/63.3.581.

[170] A. N. Baraldi and C. K. Enders, "An introduction to modern missing data analyses," *J. Sch. Psychol.*, vol. 48, no. 1, pp. 5–37, 2010, doi: 10.1016/j.jsp.2009.10.001.

[171] E. Javanmardi, Y. Gu, M. Javanmardi, and S. Kamijo, "Autonomous vehicle self-localization based on abstract map and multi-channel LiDAR in urban area," *IATSS Res.*, vol. 43, no. 1, pp. 1–13, 2019, doi: 10.1016/j.iatssr.2018.05.001.

[172] M. M. Nabi, V. Senyurek, A. C. Gurbuz, and M. Kurum, "Deep Learning-Based Soil Moisture Retrieval in CONUS Using CYGNSS Delay Doppler Maps," *IEEE J. Sel. Top. Appl. Earth Obs. Remote Sens.*, vol. 15, pp. 6867–6881, 2022, doi: 10.1109/JSTARS.2022.3196658.

[173] A. Senanayaka *et al.*, "Similarity-based Multi-source Transfer Learning Approach for Time Series Classification," *Int. J. Progn. Heal. Manag.*, vol. 13, no. 2, pp. 1–25, Oct. 2022, doi: 10.36001/ijphm.2022.v13i2.3267.

[174] C. Sun, Y. Chen, and C. Cheng, "Imputation of missing data from offshore wind farms using spatio-temporal correlation and feature correlation," *Energy*, vol. 229, p. 120777, Aug. 2021, doi: 10.1016/j.energy.2021.120777.

[175] M. Martinez-Luengo, M. Shafiee, and A. Kolios, "Data management for structural integrity assessment of offshore wind turbine support structures: data cleansing and missing data imputation," *Ocean Eng.*, vol. 173, no. November 2018, pp. 867–883, Feb. 2019, doi: 10.1016/j.oceaneng.2019.01.003.

[176] L. Pan and J. Li, "K-Nearest Neighbor Based Missing Data Estimation Algorithm in Wireless Sensor Networks," *Wirel. Sens. Netw.*, vol. 02, no. 02, pp. 115–122, 2010, doi: 10.4236/wsn.2010.22016.

[177] A. L. Hartzell, M. G. da Silva, and H. R. Shea, *MEMS Reliability*. Boston, MA: Springer US, 2011. doi: 10.1007/978-1-4419-6018-4.

[178] S. Razza and S. Burdo, "An underestimated issue: unsuspected decrease of sound processor microphone sensitivity, technical, and clinical evaluation," *Cochlear Implants Int.*, vol. 12, no. 2, pp. 114–123, May 2011, doi: 10.1179/146701010X486499.

[179] R. Vasta, I. Crandell, A. Millican, L. House, and E. Smith, "Outlier detection for sensor systems (ODSS): A MATLAB macro for evaluating microphone sensor data quality," *Sensors (Switzerland)*, vol. 17, no. 10, 2017, doi: 10.3390/s17102329.

[180] E. L. Silva-Ramírez, R. Pino-Mejías, M. López-Coello, and M. D. Cubiles-de-la-Vega, "Missing value imputation on missing completely at random data using multilayer perceptrons," *Neural Networks*, vol. 24, no. 1, pp. 121–129, 2011, doi: 10.1016/j.neunet.2010.09.008.

[181] P. J. García-Laencina, J.-L. Sancho-Gómez, A. R. Figueiras-Vidal, and M. Verleysen, "K nearest neighbours with mutual information for simultaneous classification and missing data imputation," *Neurocomputing*, vol. 72, no. 7–9, pp. 1483–1493, Mar. 2009, doi: 10.1016/j.neucom.2008.11.026.

[182] D. M. P. Murti, U. Pujianto, A. P. Wibawa, and M. I. Akbar, "K-Nearest Neighbor (K-NN) based Missing Data Imputation," in *2019 5th International Conference on Science in Information Technology (ICSITech)*, Oct. 2019, pp. 83–88. doi: 10.1109/ICSITech46713.2019.8987530.

[183] J. Maillo, S. Ramírez, I. Triguero, and F. Herrera, "kNN-IS: An Iterative Spark-based design of the k-Nearest Neighbors classifier for big data," *Knowledge-Based Syst.*, vol. 117, pp. 3–15, Feb. 2017, doi: 10.1016/j.knosys.2016.06.012.

[184] E. Acuña and C. Rodriguez, "The Treatment of Missing Values and its Effect on Classifier Accuracy," in *Classification, Clustering, and Data Mining Applications*, no. 1995, Berlin, Heidelberg: Springer Berlin Heidelberg, 2004, pp. 639–647. doi: 10.1007/978-3-642-17103-1_60.

[185] S. Zhang, J. Zhang, X. Zhu, Y. Qin, and C. Zhang, "Missing Value Imputation Based on Data Clustering," *Trans. Comput. Sci. I*, no. 60625204, pp. 128–138, 2008, doi: 10.1007/978-3-540-79299-4_7.

[186] Z. Che, S. Purushotham, K. Cho, D. Sontag, and Y. Liu, "Recurrent Neural Networks for Multivariate Time Series with Missing Values," *Sci. Rep.*, vol. 8, no. 1, p. 6085, Dec. 2018, doi: 10.1038/s41598-018-24271-9.

[187] J. Yoon, W. R. Zame, and M. van der Schaar, "Estimating Missing Data in Temporal Data Streams Using Multi-directional Recurrent Neural Networks," *IEEE Trans. Biomed. Eng.*, vol. 66, no. 5, pp. 1477–1490, Nov. 2017, doi: 10.1109/TBME.2018.2874712.

[188] Y. Peng, W. Qiao, and L. Qu, "Compressive Sensing-Based Missing-Data-Tolerant Fault Detection for Remote Condition Monitoring of Wind Turbines," *IEEE Trans. Ind. Electron.*, vol. 69, no. 2, pp. 1937–1947, Feb. 2022, doi: 10.1109/TIE.2021.3057039.

[189] D. Craven, B. McGinley, L. Kilmartin, M. Glavin, and E. Jones, "Compressed sensing for bioelectric signals: A review," *IEEE J. Biomed. Heal. Informatics*, vol. 19, no. 2, pp. 529–540, 2015, doi: 10.1109/JBHI.2014.2327194.

[190] Y. Nan, Z. Yi, and C. Bingxia, "Review of compressed sensing for biomedical imaging," *Proc. - 2015 7th Int. Conf. Inf. Technol. Med. Educ. ITME 2015*, pp. 225–228, 2016, doi: 10.1109/ITME.2015.119.

[191] T. G. Kolda and B. W. Bader, "Tensor decompositions and applications," *SIAM Rev.*, vol. 51, no. 3, pp. 455–500, 2009, doi: 10.1137/07070111X.

[192] E. E. Papalexakis, C. Faloutsos, and N. D. Sidiropoulos, "Tensors for data mining and data fusion: Models, applications, and scalable algorithms," *ACM Trans. Intell. Syst. Technol.*, vol. 8, no. 2, 2016, doi: 10.1145/2915921.

[193] F. L. Hitchcock, "The Expression of a Tensor or a Polyadic as a Sum of Products," *J. Math. Phys.*, vol. 6, no. 1–4, pp. 164–189, Apr. 1927, doi: 10.1002/sapm192761164.

[194] J. D. Carroll and J.-J. Chang, "Analysis of individual differences in multidimensional scaling via an n-way generalization of 'Eckart-Young' decomposition," *Psychometrika*, vol. 35, no. 3, pp. 283–319, Sep. 1970, doi: 10.1007/BF02310791.

[195] R. a Harshman, "Foundations of the PARAFAC procedure: Models and conditions for an 'explanatory' multimodal factor analysis," *UCLA Work. Pap. Phonetics*, vol. 16, no. 10, pp. 1–84, 1970, [Online]. Available: http://www.psychology.uwo.ca/faculty/harshman/wpppfac0.pdf

[196] Q. Song, H. Ge, J. Caverlee, and X. Hu, "Tensor Completion Algorithms in Big Data Analytics," *ACM Trans. Knowl. Discov. Data*, vol. 13, no. 1, pp. 1–48, Jan. 2019, doi: 10.1145/3278607.

[197] H. Lu, K. N. Plataniotis, and A. N. Venetsanopoulos, "MPCA: Multilinear principal component analysis of tensor objects," *IEEE Trans. Neural Networks*, 2008, doi: 10.1109/TNN.2007.901277.

[198] E. Acar, D. M. Dunlavy, T. G. Kolda, and M. Mørup, "Scalable tensor factorizations for incomplete data," *Chemom. Intell. Lab. Syst.*, vol. 106, no. 1, pp. 41–56, Mar. 2011, doi: 10.1016/j.chemolab.2010.08.004.

[199] L. Sorber, M. Van Barel, and L. De Lathauwer, "Optimization-based algorithms for tensor decompositions: Canonical polyadic decomposition, decomposition in rank-(Lr, Lr, 1) terms, and a new generalization," *SIAM J. Optim.*, vol. 23, no. 2, pp. 695–720, Jan. 2013, doi: 10.1137/120868323.

[200] L. Xiong, X. Chen, T.-K. Huang, J. Schneider, and J. G. Carbonell, "Temporal Collaborative Filtering with Bayesian Probabilistic Tensor Factorization," in *Proceedings of the 2010 SIAM International Conference on Data Mining*, Apr. 2010, pp. 211–222. doi: 10.1137/1.9781611972801.19.

[201] J. Håstad, "Tensor rank is NP-complete," in *Lecture Notes in Computer Science (including subseries Lecture Notes in Artificial Intelligence and Lecture Notes in Bioinformatics)*, vol. 372 LNCS, 1989, pp. 451–460. doi: 10.1007/BFb0035776.

[202] O. Tabaste, F. Lacan, C. Liu, and K. Carolin, "Digital Twin-enabled Collaborative Data Management for Metal Additive Manufacturing Systems," no. April, 2020, doi: 10.1016/j.jmsy.2020.05.010.

[203] S. R. Chhetri, A. Canedo, and M. A. Al Faruque, "Confidentiality breach through acoustic side-channel in cyber-physical additive manufacturing systems," *ACM Trans. Cyber-Physical Syst.*, vol. 2, no. 1, pp. 1–25, 2018, doi: 10.1145/3078622.

[204] S. Rokka Chhetri and M. A. Al Faruque, "Side Channels of Cyber-Physical Systems: Case Study in Additive Manufacturing," *IEEE Des. Test*, vol. 34, no. 4, pp. 18–25, 2017, doi: 10.1109/MDAT.2017.2682225.

[205] H. Vincent, L. Wells, P. Tarazaga, and J. Camelio, "Trojan Detection and Side-channel Analyses for Cyber-security in Cyber-physical Manufacturing Systems," *Procedia Manuf.*, vol. 1, pp. 77–85, 2015, doi: 10.1016/j.promfg.2015.09.065.

[206] C. J. Bayens, "Physical signal-based intrusion detection for cyber physical systems." Georgia Institute of Technology, 2017.

[207] Z. Shi, C. Kan, W. Tian, and C. Liu, "A Blockchain-based G-code Protection Approach for Cyber-Physical Security in Additive Manufacturing," *J. Comput. Inf. Sci. Eng.*, pp. 1–29, 2020.

[208] D. Bradley and G. Roth, "Adaptive thresholding using the integral image," *J. Graph. tools*, vol. 12, no. 2, pp. 13–21, 2007.

[209] C. A. Lowry and D. C. Montgomery, "A review of multivariate control charts," *IIE Trans.*, vol. 27, no. 6, pp. 800–810, 1995.

[210] B. A. Olshausen and D. J. Field, “Sparse coding with an overcomplete basis set: A strategy employed by V1?,” *Vision Res.*, vol. 37, no. 23, pp. 3311–3325, 1997.

[211] A. T. Bui and D. W. Apley, “Monitoring for changes in the nature of stochastic textured surfaces,” *J. Qual. Technol.*, vol. 50, no. 4, pp. 363–378, 2018.

[212] Z. Wang, C. Lu, and B. Zhou, “Fault diagnosis for rotary machinery with selective ensemble neural networks,” *Mech. Syst. Signal Process.*, vol. 113, pp. 112–130, 2018, doi: 10.1016/j.ymssp.2017.03.051.

[213] O. Alshorman *et al.*, “A Review of Artificial Intelligence Methods for Condition Monitoring and Fault Diagnosis of Rolling Element Bearings for Induction Motor,” *Shock Vib.*, vol. 2020, no. Cm, 2020, doi: 10.1155/2020/8843759.

[214] C. Lu, Y. Wang, M. Ragulskis, and Y. Cheng, “Fault diagnosis for rotating machinery: A method based on image processing,” *PLoS One*, vol. 11, no. 10, pp. 1–22, 2016, doi: 10.1371/journal.pone.0164111.

[215] P. Henriquez, J. B. Alonso, M. A. Ferrer, and C. M. Travieso, “Review of automatic fault diagnosis systems using audio and vibration signals,” *IEEE Trans. Syst. Man, Cybern. Syst.*, vol. 44, no. 5, pp. 642–652, 2014, doi: 10.1109/TSMCC.2013.2257752.

[216] N. Sikder, K. Bhakta, A. Al Nahid, and M. M. M. Islam, “Fault diagnosis of motor bearing using ensemble learning algorithm with FFT-based preprocessing,” *1st Int. Conf. Robot. Electr. Signal Process. Tech. ICREST 2019*, pp. 564–569, 2019, doi: 10.1109/ICREST.2019.8644089.

[217] V. Vakharia, V. K. Gupta, and P. K. Kankar, “Ball Bearing Fault Diagnosis Using Supervised and Unsupervised Machine Learning Methods,” vol. 20, no. 4, 2015.

[218] T. P. Banerjee and S. Das, “Multi-sensor data fusion using support vector machine for motor fault detection,” *Inf. Sci. (Ny).*, vol. 217, pp. 96–107, 2012, doi: 10.1016/j.ins.2012.06.016.

[219] D. Kolar, D. Lisjak, M. Pająk, and M. Gudlin, “Intelligent Fault Diagnosis of Rotary Machinery by Convolutional Neural Network with Automatic Hyper-Parameters Tuning Using Bayesian Optimization,” *Sensors*, vol. 21, no. 7, p. 2411, Mar. 2021, doi: 10.3390/s21072411.

[220] Q. Hang, J. Yang, and L. Xing, “Diagnosis of Rolling Bearing Based on Classification for High Dimensional Unbalanced Data,” *IEEE Access*, vol. 7, pp. 79159–79172, 2019, doi: 10.1109/ACCESS.2019.2919406.

[221] R. S. Gunerkar, A. K. Jalan, and S. U. Belgamwar, “Fault diagnosis of rolling element bearing based on artificial neural network,” *J. Mech. Sci. Technol.*, vol. 33, no. 2, pp. 505–511, 2019, doi: 10.1007/s12206-019-0103-x.

[222] J. Wu, X. Y. Chen, H. Zhang, L. D. Xiong, H. Lei, and S. H. Deng, “Hyperparameter optimization for machine learning models based on Bayesian optimization,” *J. Electron. Sci. Technol.*, vol. 17, no. 1, pp. 26–40, 2019, doi: 10.11989/JEST.1674-862X.80904120.

[223] M. M. Herterich, F. Uebernickel, and W. Brenner, “The impact of cyber-physical systems on industrial services in manufacturing,” *Procedia CIRP*, vol. 30, pp. 323–328, 2015, doi: 10.1016/j.procir.2015.02.110.

[224] A. Diez-Olivan, J. Del Ser, D. Galar, and B. Sierra, “Data fusion and machine learning for industrial prognosis: Trends and perspectives towards Industry 4.0,” *Inf. Fusion*, vol. 50, no. October 2018, pp. 92–111, Oct. 2019, doi: 10.1016/j.inffus.2018.10.005.

[225] N. BAYDAR and A. BALL, “DETECTION OF GEAR FAILURES VIA VIBRATION AND ACOUSTIC SIGNALS USING WAVELET TRANSFORM,” *Mech. Syst. Signal Process.*, vol. 17, no. 4, pp. 787–804, Jul. 2003, doi: 10.1006/mssp.2001.1435.

[226] P. Bansal, P. Deshpande, and S. Sarawagi, “Missing value imputation on multidimensional time series,” *Proc. VLDB Endow.*, vol. 14, no. 11, pp. 2533–2545, Jul. 2021, doi: 10.14778/3476249.3476300.

[227] X. Chen, M. Lei, N. Saunier, and L. Sun, “Low-Rank Autoregressive Tensor Completion for Spatiotemporal Traffic Data Imputation,” *IEEE Trans. Intell. Transp. Syst.*, vol. 23, no. 8, pp. 12301–12310, 2022, doi: 10.1109/TITS.2021.3113608.

[228] X. Chen, Z. He, and L. Sun, “A Bayesian tensor decomposition approach for spatiotemporal traffic data imputation,” *Transp. Res. Part C Emerg. Technol.*, vol. 98, no. June 2018, pp. 73–84, 2019, doi: 10.1016/j.trc.2018.11.003.

[229] T. G. Kolda and B. W. Bader, “Tensor Decompositions and Applications,” *SIAM Rev.*, vol. 51, no. 3, pp. 455–500, Aug. 2009, doi: 10.1137/07070111X.